Directive dielectric designs for high efficiency photovoltaics

van der Burgt, J.S.

Publication date
2022
Document Version
Final published version

Citation for published version (APA):
van der Burgt, J. S. (2022). *Directive dielectric designs for high efficiency photovoltaics*.

Directive Dielectric Designs

for high efficiency photovoltaics

Julia S. van der Burgt

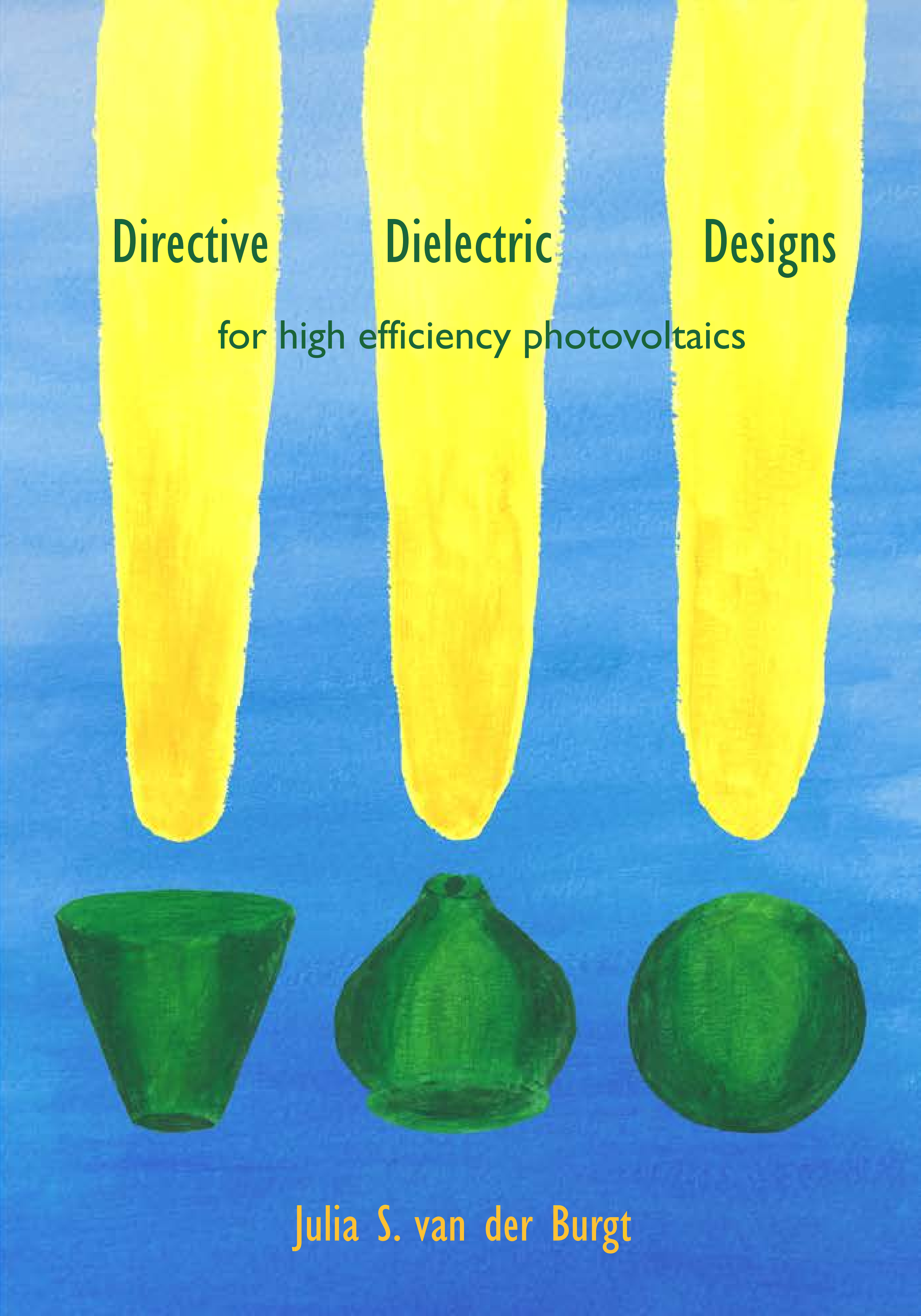

Directive Dielectric Designs for high efficiency photovoltaics

Julia S. van der Burgt

2022

Directive dielectric designs for high efficiency photovoltaics

Directive Dielectric Designs for high efficiency photovoltaics
Ph.D. Thesis, University of Amsterdam, June 2022
Julia van der Burgt

ISBN:978-94-92323-64-4

Cover design: *artist's impression of directional emission from the three nanophotonic designs that are described in this thesis, painted by Julia van der Burgt.*

The work described in this thesis was performed between December 2017 and April 2022 at NWO-Intitute AMOLF, Science Park 104, 1098 XG Amsterdam, The Netherlands.

This work is part of the Dutch Research Council (NWO).

A digital version of this thesis is available at:
https://www.lmpv.nl/Theses/.

Printed by Optima Grafische Communicatie

DIRECTIVE DIELECTRIC DESIGNS FOR HIGH EFFICIENCY PHOTOVOLTAICS

ACADEMISCH PROEFSCHRIFT

ter verkrijging van de graad van doctor
aan de Universiteit van Amsterdam,
op gezag van de Rector Magnificus
prof. dr. ir. K.I.J. Maex,
ten overstaan van een door het College voor Promoties ingestelde commissie,
in het openbaar te verdedigen in de Agnietenkapel
op donderdag 7 juli 2022, te 10.00 uur

door Julia Sofieke van der Burgt
geboren te Wageningen

Promotiecomissie

Promotor:	prof. dr. E.C. Garnett	Universiteit van Amsterdam
Copromotor:	prof. dr. A. Polman	Universiteit van Amsterdam
Overige leden:	prof. dr. A.F. Koenderink	Universiteit van Amsterdam
	prof. dr. N.F. Shahidzadeh	Universiteit van Amsterdam
	dr. J. van de Groep	Universiteit van Amsterdam
	prof. dr. T. Kirchartz	Universität Duisburg Essen
	prof. dr. I. Staude	Friedrich-Schiller-Universität Jena

Faculteit der Natuurwetenschappen, Wiskunde en Informatica

"The best that most of us can hope to achieve in physics is simply to misunderstand at a deeper level."

–**Wolfgang Pauli**

Contents

1

INTRODUCTION

1.1 LIGHT

Light is all around us. It provides us with energy and information. From light bulbs or screens in our daily life to the complete history of planet earth that is powered by sunlight, we cannot think of a life without light. Our most dominant sense is our vision,[1] with which we obtain information about the world around us via light hitting our eyes. Information on the internet is swiftly spread around the world in the form of light signals in glass fibers. The sunlight hitting the earth in a single day contains twenty times more energy than what humankind consumes in a year.[2] This light keeps us warm, makes plants grow, and just a tiny fraction of all that light is used to generate electricity with solar cells.

Having control over light - being able to detect, collect, generate and guide light - is extremely important for all kinds of technologies. From large-scale solar cells to bright and efficient light-emitting diodes (LEDs), from glass fiber cables across the ocean to tiny on-chip circuits that communicate with light, all require control over generating, absorbing, or sensing light in/from a specific direction, at a specific wavelength. With solar cells we usually want to absorb as much light as possible, to convert it to electricity. Although not always: sometimes, for aesthetic reasons or double functionality we might want to absorb only specific colors, or only part of the light. For lighting and screens, we want efficient light emission of a specific (mix of) color(s). The light only has to go into a specific direction: towards the viewer. In information technology, light signals can be used to process information. On-chip light circuits require microscopic light emitters and detectors, and light signals that travel in a specific direction with accurate emission and detection

1.2 NANOPHOTONICS

For achieving such control over light emission and absorption, we can find a wide range of tools for light manipulation in the field of nanophotonics, where one studies the interaction of light with nanometer-sized objects. Since these objects are on the order of, or smaller than the wavelength of light, they ‘see’ the light differently than macroscopic objects. While large objects experience light as a continuum, nano-scale structures can interact with individual photons and feel the fluctuating electric and magnetic fields of light. Next to the material properties, the size and shape of a nano-scale object become very important for how it interacts with light. This allows, for example, to have very strong interaction for only a specific color, when the corresponding wavelength exactly matches the size of the structure. This is called a resonance. For light-emitting materials, the color, rate, and efficiency at which they emit light can be influenced by the shape and size, as well as the direction of light emission.

Nanophotonics can be split up into two categories: plasmonics and dielectrics. In plasmonics, metals are used. The free electrons in a metal, which are also responsible for the electrical conductivity, react to the electric field of light. When light shines on a metal nanoparticle, the electrons can start to collectively move with the electric field, called a plasmon resonance. This gives a very strong interaction between the light and the particle, resulting in strong light scattering for particles much smaller than the wavelength of light. However, some energy is always dissipated as heat in the metal. This parasitic absorption makes plasmonics inherently lossy. On the other hand, there are dielectric materials, i.e. insulators. Here the electrons are not free to move, but in an electric field they can still get displaced a bit from the nuclei. The material becomes polarized, and the polarizability is an important parameter for the optical response. When the material is transparent, i.e. non-absorbing, at the wavelength of interest, dielectric nanostructures can be (almost) free from parasitic absorption. Dielectric structures need to be larger than plasmonics, on the order of the wavelength or larger. Light can be trapped inside a transparent dielectric and bounce back and forth in a cavity, or travel along the length in a waveguide. When the light goes from one material to another, with a different refractive index, it changes direction, an effect used on the used on macroscopic scale in lenses and prisms. When periodic structures or small holes are used, interference of light from different locations on the structure can give diffraction patterns. By combining resonances, wave guiding, diffractive and refractive effects, dielectrics provide a large range of tools to manipulate light absorption, emission, and scattering. In this thesis, we study nanophotonics of dielectrics, because the parasitic absorption in plasmonics is detrimental to the envisioned applications in solar cells.

1.3 NEED FOR IMPROVEMENT

With the tremendous challenges of the energy transition, existing technologies need to be further optimized and new technologies must be developed. To supply the world with renewable energy, solar, together with wind, is expected to be the major player. To reach the target of less than 1.5° global warming, electricity generation from solar energy has to increase by a factor of 50 in 2050, as shown in figure 1.1.[3] To realize this, solar energy technologies need to be developed further in many aspects.[4] Efficiency improvements are needed to meet the demand and reduce costs, material consumption, and land area use. New photovoltaic (PV) materials must come to market, and semi-transparent and flexible devices must be developed for the increasing range of specific applications. Also on the energy-saving side, large improvements are needed. LEDs must become more efficient to satisfy the growing demand for lighting and displays. Traditional electronics or mechanics might get replaced by more energy-efficient systems from the emerging field of smart materials. For example, by mimicking the human brain with artificial synapses based on optical networks,[5] energy-efficient hardware can be developed for already widely used artificial intelligence algorithms.[6]

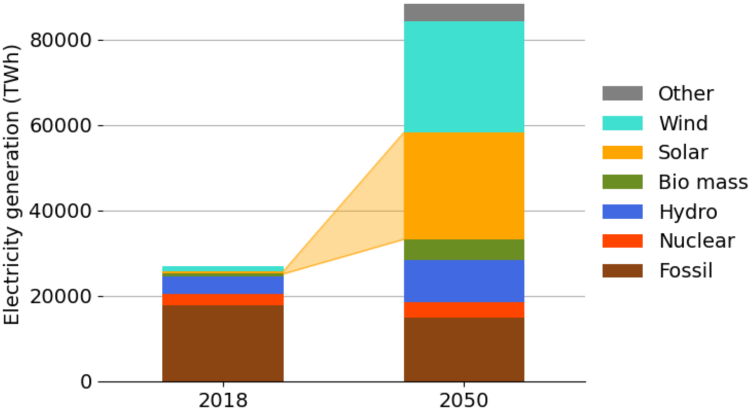

Figure 1.1: Electricity generation in 2018 and needed electricity generation in 2050 by source to reach the 1.5° global warming scenario. Electricity generation from solar power has to increase by a factor of forty from about 600 TWh in 2018 to 25000 TWh in 2050.[3]

1.4 Solar cells

Currently, over 90% of all solar energy generation relies on silicon PV cells.[7] Although tremendous improvements have been made over the past decades in terms of efficiency and costs, silicon solar cells are reaching their limits. Given the intrinsic material properties of silicon, efficiencies above 29% simply cannot be achieved. To keep up with the decrease in price per kWh installed capacity necessary for further growth of the PV market, new techniques must be developed. Nanophotonics provides many tools for further optimization.[8] It has been widely studied for improving solar cell performance, where traditionally the focus has been on improving light absorption, important for maximizing the current generated by the solar cell.[9] The voltage of a cell was more considered a material property, determined by the bandgap and the quality of the material. This has led to record solar cells having their short circuit current (J_{sc}) close to the theoretical limit, while the open-circuit voltage (V_{oc}) was lagging behind.[10] However, by accurately managing the light going into and out of the solar cell with nanophotonic engineering, V_{oc} can also be increased. The mechanisms behind this will be discussed in detail in chapter 2. Also, new solar cell materials must come to market, to fill niche applications where silicon is not applicable, like flexible solar cells, or to join forces with silicon solar cells in tandem configurations. In a tandem solar cell, two materials are combined, that absorb different parts of the solar spectrum: one for the high energy blue and green light and one for the lower energy orange and red light. For both tandem and flexible solar cells, halide perovskite materials are promising candidates, which will be discussed in the next section.

1.4.1 LUMINESCENT SOLAR CONCENTRATORS

Luminescent solar concentrators (LSCs) are an interesting alternative to planar PV panels. LSCs rely on a transparent slab of material impregnated with fluorescent particles. These particles, called luminophores, absorb incident sunlight and re-emit it as fluorescence. Due to total internal reflection on the surfaces of the slab, light is guided towards the edges. Here it is collected with PV cells that are much smaller than the total collection area. This technique has several advantages. First of all the large collection area can be made of an inexpensive polymer or glass, and much less PV cell material is needed. Highly efficient but expensive PV materials like gallium-arsenide become affordable for the small PV cells on the edges. Furthermore, it allows for semi-transparent and colored devices, which suit building-integrated PV. So far efficiency of LSCs has been low, due to the additional loss pathways in the process towards generating electricity. First of all, efficient luminophores are needed, that re-emit close to 100% of the light that they absorb. Subsequently, the light has to travel through the waveguide towards the PV cells. Photons that are emitted towards the waveguide surface at angles smaller than the angle of total internal reflection will escape from the waveguide. Photons that are guided by the waveguide, can be scattered or re-absorbed by the luminophores, which again gives a chance of escaping from the waveguide or decaying non-radiatively in the luminophore. Nanophotonic structures can play an important role in overcoming these limitations and optimizing the waveguide efficiency of LSCs. Since they can be used to accurately control absorption and emission properties as a funtion of wavelength and angle, emission into the waveguide can be improved and re-absorption can be reduced, while maintaining high sunlight absorption. Together with recent improvements in luminophore efficiency, nanophotonic techniques for directional light emission open new possibilities for high-efficiency LSCs.

1.5 PEROVSKITES

Perovskites can be easily called the new wonder material of the twenty-first century. Although this material family was discovered already in 1839 and studied extensively for its superconducting properties, it has experienced an incredible revival since the discovery of a 2% efficient perovskite solar cell in 2006.[11] Initially, the name perovskite referred to a calcium titanium oxide mineral with the chemical formula $CaTiO_3$, but nowadays the name is used to describe the family of materials that consist of corner-sharing octahedra, usually with the generic chemical formula ABX_3. This structure is shown in figure 1.2a. Corner-sharing BX_6 octahedra form the core of the structure and largely determine the optical and electronic properties. The A-site cations in between balance the charge and proivde the necessary crystal stability. Perovskites with many different cations and anions have been made, resulting in a wide range of material properties. In addition, different cations and anions can be mixed within a perovskite crystal, allowing for fine-tuning the properties. A well-known example is the possibility of bandgap tuning through mixing of different halide anions. By gradually moving from pure chloride, via mixed states with bromide, to pure iodide, emission from cesium lead halide perovskite quantum dots can cover the full visible spectrum, shown in figure 1.2b.[12] Perovskites can be easily processed, for example from solution, which gives it the prospect for mass production at low costs.[13] Since the first perovskite solar cell in 2006, a tremendous increase in efficiency has been achieved, to 25.5% in 2020, with which it can now compete with silicon. Also other applications have been successfully demonstrated, ranging from sensors to batteries and from LEDs to memory devices.

The main limiting factors that are still hampering large-scale application of perovskite devices are stability and toxicity. A perovskite is basically a salt, which easily dissolves in water. For solar cell devices, the high sensitivity to water, and even to humidity in the air, is detrimental. The best performing perovskite solar cells contain lead atoms, which makes dissolving in water and leaking into the environment a serious health threat. In addition, perovskites are known to show a lot of imperfections in the crystal lattice, of missing atoms or atoms at the wrong position. One of the special properties of perovskties is that optical and electronic properties do not suffer a lot from such defects. This is contrary to many other materials, like silicon, where an almost perfect crystal is needed for optimal functioning. On the other hand, these defects make the perovskite properties subject to change. Under influence of light, pressure or electric fields, ions can move around, called ion migration, which changes the optoelectrical properties. While this kind of behavior in some cases can be used, for example in sensors, where sensitivity to external stimuli is desirable, it often limits stable functioning devices. While a lot of research has been dedicated to making perovskites more stable, we show in this thesis how the dynamic nature can be used to our advantage.

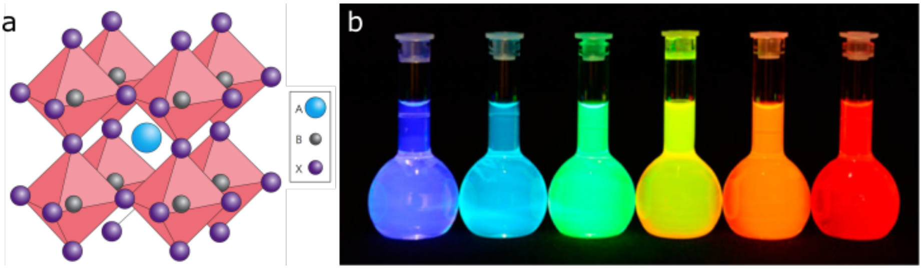

Figure 1.2: a) The atomic structure of perovskite crystal. It consists of two cations (A and B) in the center and on the corners of the cube, respectively, and anions C on the faces of the cube. Each cation and anion can also be a mixture of different elements or molecules, which provides an incredible range of properties that can be accurately tuned by the chemical composition of the perovskite.Figure taken from;[14] b) Cesium Lead halide ($CsPbX_3$, X= Cl, Br, I) nanocrystals can emit light at all visible wavelengths by varying the halide composition. Figure taken from[12]

1.6 MOTIVATION AND OUTLINE

In this thesis we investigate how dielectric nanophotonic structures can be used to create directional light emission. Through a combination of theoretical analysis and experimental verification we investigate several directional emitting dielectric systems. Simulations show the potential impact of such emitters on device performance: the effect of directional nanophotonic structures on performance in realistic operating conditions for planar and tandem solar cells, the effect of controlled halide segregation on perovskite solar cell performance and the effect of directional emitters on LSC efficiency. A newly built experimental setup is used to measure directivity with higher accuracy than before, in which a record directivity from all-dielectric nanostructures is measured and the dynamics of a self-optimizing system are tracked.

In **Chapter 2** we give a general introduction of how nanophotonic engineering can be used to reach high efficiency solar cells. The detailed balance method is introduced, which gives an upper limit to solar cell efficiency, which can be used to benchmark solar cell performance. We explain the importance of controlling the light emission for reaching high open circuit voltages, and analyze the potential effect of two nanophotonic applications on solar cell performance in real world operating conditions.

In **Chapter 3** we give experimental evidence of a new record in directional emission from an all-dielectric nanostructured microlens. This record value was achieved by making three improvements compared to previous work. First, a well-localized emitter at the center of the lens was fabricated with direct electron beam patterning of quantum dot emitters. Second, the fabricated lens structure was optimized to accurately match the designed shape. Finally, with a dedicated measurement setup the full directivity into all angles could be measured, by combining a Fourier microscope with an integrating sphere. In conventional measurement schemes only the partial directivity within the numerical aperture of the objective can be determined.

In **Chapter 4** we show how this same microlens can be used for a self-optimizing system, where we use the dynamic nature of mixed halide perovskite films to make a responsive and adaptive system. It shows some of the basic requirements for material learning and memory and can be seen as a case study for a wide range of potential applications where the dynamic and adaptive nature of perovskites is used as a feature. Here we use ligh-induced phase segregation of halide ions in a mixed halide perovskite film to form an emitter in the hotspot of the microlens. The concept of reciprocity states that an emitter in the hotspot of an incoming plane wave, will give directional emission into the direction of the incoming light. This makes the system self-aligned and robust against small distortions in the lens, resulting in higher directivity compared to that of the same lens in Chapter 3.

In **Chapter 5** we investigate how the self-aligned photo-induced phase segregation concept can be applied to perovskite solar cells to make a self-tracking solar concentrator system with absorption of diffuse sunlight. While phase segregation of halide ions in mixed halide perovskites in many cases reduces performance, we show that it can lead to effective concentration and thereby higher efficiency when it happens in a controlled manner. Instead of the nanophotonic microlenses, we use simple glass microspheres, that focus the incoming sunlight, induce local phase segregation and redirect the emission. Simulations predict large potential increases in solar cell performance. Simple large scale monolayer self-assemby of spheres, resulting in increased absorption and directional emission was shown experimentally. The simple fabrication of sphere monolayers gives the prospect for large scale application.

Chapter 6 discusses the potential of directional light emission for Luminescent Solar Concentrators. Thorough Monte Carlo ray-tracing simulations reveal the importance of directivity and the potential for high efficiency LSCs. While intensive research on luminophores with high photoluminescent quantum yield has led to almost perfect emitters, there has been less attention for directional emitters, while both factors are equally important for final performance.

In the final chapter, **Chapter 7**, a more detailed analysis of the concept of forward emitting structures, as introduced in chapter 6, is performed. The Monte Carlo ray-tracing model is expanded to also include the effects of anisotropic absorption, and the additional benefits of forward emitting structures are revealed.

2

Nanophotonic Emission Control for Improved Photovoltaic Efficiency

With the necessary transition to renewable energy at hand, there is a renewed research focus on increasing solar cell efficiency, in order to reduce the cost of electricity. Nanomaterials are promising candidates to contribute to a new generation of low cost and highly efficient solar cells. Due to their wavelength-scale dimensions, nanomaterials display exceptionally strong light-matter interactions that lead to large perturbations in absorption and emission compared to their bulk counterparts. Although most work on nanostructured solar cells has focused on increasing the absorption, emission control may have even greater potential for improving efficiency of state-of-the-art solar cells. In this chapter, we describe how nanostructures can be applied to improve solar cell efficiency, focusing on emission control. First, we analyze the requirements for making the most efficient solar cell, by looking at the thermodynamics of energy conversion. We show that an ideal solar cell at open circuit displays emission that is identical to its absorption. Comparing this to the emission of a typical silicon solar cell shows that there are three differences: the intensity, the angles in which light is emitted, and the spectrum. These differences lead to a reduction in efficiency, mainly due to a drop in open circuit voltage. For each loss mechanism, we discuss how nanomaterials can manipulate the emission and thereby reduce the voltage loss. Finally, we analyze the performance of two conceptual designs for solar cells based on nanomaterials. These give a large improvement in efficiency compared to conventional designs, showing the great potential of nanomaterials in solar cells.

2.1 INTRODUCTION

Over the past decades, the price of electricity generated by solar panels dropped drastically.[15] However, to become fully competitive with fossil fuels, including the cost of energy storage, electricity from solar panels has to become even cheaper. The materials, manufacturing and installation costs are already pushed to their lower limit, but by increasing the electricity output per panel, the price of energy can be reduced further.[16,17] This requires an increase in solar cell efficiency.

Nanomaterials display exceptionally strong light-matter interactions and are therefore promising candidates to consider for the next generation of high efficiency solar cells.[10,18,19] The close matching between the wavelength of light and the size of nanomaterials can lead to a variety of resonant effects.[18] By controlling their shape and size, nanomaterials offer greatly enhanced flexibility in tuning the angle, wavelength and rate of both absorbed and emitted photons compared to their bulk counterparts.[20,21] This so-called nanophotonic engineering allows for optimizing the optical properties for application in solar cells.

Initially most research in the field of nanophotonics for solar cells was focused on maximizing light absorption. Nanomaterials can act as optical antennas, concentrating light from an area much larger than their physical size, leading to greatly enhanced absorption. The electrical current generated by a solar cell scales with the number of absorbed photons, and the optimization of light absorption has led to short circuit currents (J_{sc}) close to the theoretical maximum.[10] The open circuit voltage (V_{oc}) of solar cells, however, was mostly seen as a consequence of material properties, design architecture and fabrication, and was less considered as an optical problem.

It can be shown however, that nanophotonic engineering can also improve the open circuit voltage, by optimizing light emission of the solar cell. The connection between optimizing light absorption and increasing current is very clear, but optimization of light management for high V_{oc} is less intuitive. Although the importance of emission control was already recognized by Shockley and Queisser in their seminal paper on solar cell efficiency[22] and later discussed in more detail several decades ago,[23] practical implementation has been limited. Improvements have been made, but the achieved open circuit voltages are still further away from the theoretical limit[10] than the achieved J_{sc}. The only exception is Gallium-Arsenide (GaAs) solar cells, which have been studied for their outstanding optical properties for a long time.

Most early work on emission control was based on angle restriction filters, that block emission into certain angles. Only recently nanophotonic strategies started to be implemented that allow for a fundamentally different approach, with the key difference being the stage at which the emission is controlled. Angle restriction filters, even if they are based on nanoscale structures like Bragg stacks or photonic crystals,[24,25,26] interact with the light after it has been emitted. Nanophotonic engineering changes the photonic environment of the emitter, and thereby the emission process itself. This is particularly relevant for non-ideal materials, where non-radiative recombination is dominant. With angle restrictors the light emitted at oblique angles is reflected back, which leads to an increase of photon recycling, i.e. reabsorption of emitted photons. This reabsorption enhances the non-radiative recombination. In any practical application, this increase in non-radiative recombination nullifies any increase in efficiency coming from angle restriction.[27] This led to the general idea that emission control only helps for materials close to the radiative limit. However, nanophotonic structures enable emission control while simultaneously reducing non-radiative recombination.[21, 28, 29, 30, 20] In this perspective paper we will give an overview of how nanophotonic engineering can be used to increase solar cell efficiency, with a focus on increasing the open circuit voltage, by exploring the opportunities arising from light-matter interactions at the nanoscale that are fundamentally different from any bulk phenomena.

This perspective article is structured as follows. We start with deriving the theoretical maximum efficiency for converting solar energy to electrical power. This derivation gives insight in why light emission is an important performance parameter for solar cells and shows us how an ideal solar cell should perform. From this theoretical maximally efficient solar cell we can find three aspects in which any real solar cell differs from the ideal one. These lead to three loss mechanisms that limit the efficiency of solar cells. For each of these, we will discuss nanophotonics strategies that can be applied to minimize the losses. Finally, we will present two designs for high efficiency solar cells, based on the proposed techniques, and we analyze the performance modeled under realistic operation conditions. We discuss the (optical) properties required for such cells and highlight some of the most important research questions that still need to be addressed.

2.2 Fundamentals of photovoltaics

The upper limit on the conversion efficiency of solar to electrical energy is set by the first and second law of thermodynamics. These laws have played a major role in the development of any energy technology we have today. Applying them to solar energy conversion, will give insight in how we can approach the upper limit of efficiency. In the thermodynamic model, the photovoltaic (PV) system acts as a heat engine, with the sun as the hot source, the ambient as the cold source and the light as heat exchange medium. Optimizing a heat engine requires optimizing the heat exchange. In the case of PV this means optimizing the light management is a way to improve efficiency. Understanding how a PV system should operate from a thermodynamics point of view, gives insight in how we should manage the light with nanophotonics.

When a heat engine extracts heat from a hot source at T_H, not all energy can be converted into useful work. Since work is free of entropy, the entropy from the hot source has to go somewhere else, which requires some heat to be lost towards a cold sink at T_C. The maximum efficiency of this heat engine is given by the Carnot limit:

$$\eta_{carnot} = 1 - \frac{T_C}{T_H}. \tag{2.1}$$

With the sun at T_H=6000K and the ambient at T_C=300K, the maximum efficiency is 95%.

This limit can be reached in theory with the following requirements: the PV system consists of an infinite stack of solar cells with smoothly varying bandgap from 0 to ∞ with full absorption and without the presence of any non-radiative recombination and etendue expansion.[31] The performance of such a system can be derived, based on the fact that any material at non-zero temperature must exchange thermal radiation with the environment to be in thermal equilibrium. According to Kirchhoff's reciprocity law, absorption and emission at a given wavelength, into a given angle are always coupled.[32] The emission (and thus absorption) spectrum of an ideal black body is described by Planck's law and is a function of temperature. The incident flux of photons with energy E on a solar cell coming from the sun at temperature T_S is:

$$f_i = \frac{1}{exp\left(\frac{E}{k_B T_S}\right) - 1} \frac{2\pi E^2}{h^3 c^2}, \tag{2.2}$$

with h being Planck's constant, q the elemental charge, k_B Boltzmann's constant and c the speed of light. Note that this equation assumes illumination from the full hemisphere or full concentration, corresponding to no etendue expansion between emission and absorption. When a voltage builds up in a material, the emission intensity is increased. The flux of photons f_0 emitted by a solar cell at energy E depends on the temperature T_C and the voltage V over the cell according to:

$$f_0 = \frac{1}{exp\left(\frac{E-qV}{k_B T_C}\right) - 1} \frac{2\pi E^2}{h^3 c^2}. \tag{2.3}$$

This equation gives the photon flux emitted by each cell with a bandgap at E in the infinite stack of cells.[31] In open circuit, when no electrical current is extracted from the cell, the emitted and absorbed photon flux must balance to reach thermal equilibrium. The emission spectrum of the infinite stack of solar cells then equals the emission spectrum of the sun, meaning that $f_0 = f_i$ at every E, which requires:

$$\frac{E - qV_{oc}}{k_B T_C} = \frac{E}{k_B T_S} \tag{2.4}$$

Where V_{oc} is the open circuit voltage in each cell. This can be rewritten to:

$$\frac{qV_{oc}}{E} = 1 - \frac{T_C}{T_S} = \eta_{carnot}, \tag{2.5}$$

which gives a direct relation between the theoretical maximum V_{oc} in each cell and the Carnot limit. It shows that the energy of the photons (E) is converted to energy of electrons (qV_{oc}) with the Carnot efficiency.

From this derivation, we can conclude that to optimize solar cell performance, the emission spectrum at V_{oc} must approach that of the sun. In a practical solar cell, three effects cause the emission spectrum to differ from the solar spectrum and thereby reduce efficiency. First of all, a practical solar cell consists of a limited number of materials, often only one. A single bandgap material has a narrow emission spectrum, that peaks close to the bandgap and exponentially decreases towards higher energy. The second effect is the difference between absorption and emission angles. In the derivation above, emission and absorption happen in the same solid angle. In practice, a cell receives collimated sunlight over a narrow angle, while it emits in all directions. This increase in etendue can be seen as a heat loss towards the environment or as an increase in photon entropy. Finally, any real material provides non-radiative pathways, via which absorbed photons are lost as heat towards the environment. This reduces the emission intensity compared to the incoming sunlight.

To extract power, current must be drawn. This moves the system away from the reversible Carnot limit and reduces the maximum efficiency. Excited states now do work instead of emitting light, which reduces the emission intensity. The resulting maximum power conversion efficiency is 87%.[31] It is important to make the distinction between this useful reduction in voltage and the three mechanisms mentioned above, which decrease the voltage without increasing the current.

The well known Shockley-Queisser limit[22] is also based on thermodynamics, but for a less idealized system. It includes two of the three loss mechanisms: it assumes a single stepwise bandgap and takes into account the difference in solid angle between emission and absorption, but it does not include non-radiative recombination. The system is characterized by the short circuit current density J_{sc}, which is the same as the photo-generated current density, and the dark current density J_0, which is the recombination current density in the dark. These two determine the open circuit voltage V_{oc} according to[33]

$$V_{oc} = \frac{k_B T}{q} ln\left(\frac{J_{sc}}{J_0}\right). \tag{2.6}$$

With these assumptions, the efficiency as a function of bandgap can be calculated, shown as the red line in figure 2.1. This calculation uses the AM1.5G spectrum with 1 sun illumination. It has a maximum efficiency of 34%, which is far below the limit of 87% due to the emission being narrowband and isotropic.

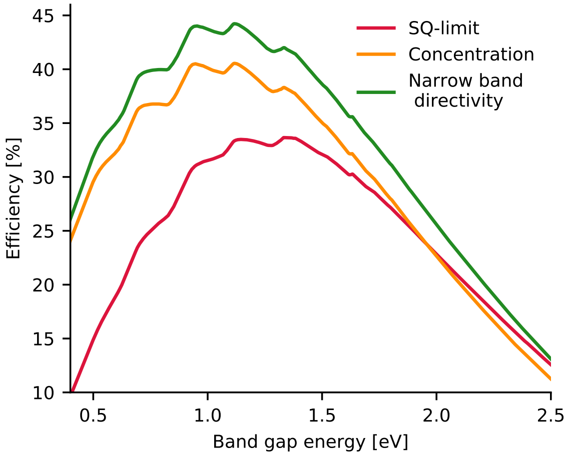

Figure 2.1: Maximum achievable efficiency as a function of bandgap energy based on the AM1.5 spectrum for three models: the SQ limit (blue), maximum concentration of 46200 (orange) and maximum directivity of 46200 over a narrow band width optimized at each bandgap (green). The latter one also captures the diffuse part of the light efficiently.

Any real single junction solar cell under one sun illumination performs below the SQ limit, due to non-radiative recombination of excited electrons. By analyzing the performance of a record efficiency silicon solar cell, we can quantify how much each of the three loss mechanisms contributes to a reduction in current and/or voltage. For this analysis we assume the solar cell has a stepwise bandgap of 1.1 eV. The amount of non-radiative recombination is given by the photoluminescence quantum yield (PLQY), which is the ratio of radiative recombination to the total (radiative plus non-radiative) recombination. We use a PLQY of 1%, which is the typical value for state-of-the-art silicon solar cells.[34,35] With these assumptions, the modeled cell has an efficiency of 28% under the AM1.5G spectrum. The actual record lies at 26.7%,[36] meaning that other non-idealities that are not considered in this model account for only 1.3%. These are, for example, no ideal stepwise absorption onset and imperfections at the contacts. The remaining difference between the record efficiency and the maximum achievable efficiency of 87%, can be split up in different contributions, as shown in figure 2.2. The fraction of photons that is not absorbed, contains only 19% of the incoming energy. Considering that the conversion efficiency at maximum power generation is 87%, the energy loss due to non-absorbed photons, and thus loss in current, is 16%. The remaining 43% of efficiency loss compared to the maximum power conversion efficiency is due to reductions in voltage, originating from increases in J_0: 5% efficiency loss due to the non-radiative recombination, 12% loss due to isotropic emission and 26% due to thermalization of high energy electrons. In the following sections we will discuss each of the loss mechanisms in more detail, and provide nanophotonic concepts that can help to overcome these losses.

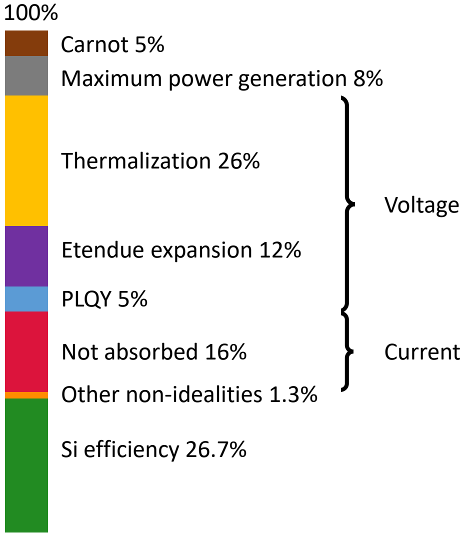

Figure 2.2: Contribution of different loss mechanisms to the total reduction in power conversion efficiency compared to the thermodynamic limit. Most losses (43%) are caused by a reduction in voltage.

2.3 Improving light emission

The reduction in emission intensity due to non-radiative recombination is the first loss mechanism that we will discuss. Any non-radiative recombination increases the saturation current density J_0 and thereby reduces the voltage compared to the radiative limit $V_{oc,rad}$ according to:[33]

$$V_{oc} = V_{oc,rad} + \frac{k_B T}{q} ln\left(PLQY\right), \tag{2.7}$$

The radiative limit is very similar to the SQ limit, but takes into account the realistic, non-stepwise, absorption spectrum. A high performance solar cell should have good absorption anywhere above the bandgap and all of the discussion below assumes that good absorption is achieved. The radiative limit is not approached by reducing J_0 when J_{sc} is not maintained, because efficiency changes only logarithmically with J_0(equation (2.6)), while it changes linearly with J_{sc}.

In approaching the radiative limit, PLQY is the key performance parameter. It is the rate of externally emitted photons divided by the total recombination rate and is determined by two parameters. One is the internal luminescence efficiency Q_i^{lum}, which depends on the radiative and non-radiative rates inside the material. The second is the escape probability p_e: the probability that an internally generated photon makes it to the far field, outside the material. Otherwise it is reabsorbed with probability p_r or parasitically absorbed with probability p_a, such that $p_e + p_a + p_r = 1$. The PLQY expressed in these terms is given by:[33]

$$PLQY = \frac{Q_i^{lum} p_e}{1 - Q_i^{lum} p_r}, \tag{2.8}$$

To approach the radiative limit, we have to maximize Q_i^{lum} and p_e. The internal luminescence efficiency Q_i^{lum} is increased by decreasing the non-radiative recombination rate or by increasing the radiative rate. The probability p_e is increased by improving light outcoupling. Reabsorption in the active material is preferable over parasitic absorption in other materials, so increasing p_r can increase solar cell performance. Once p_a is minimized, p_e should be increased in order to approach the radiative limit.

The non-radiative recombination rate constant is set by the material quality and scales with the density of defects. Nanomaterials can show higher material quality, because they are more easily grown as single crystals. Also lattice mismatch with the substrate is more easily accommodated, allowing for a wider range of materials to be combined. The large surface-to-volume ratio was for a long time considered to be the main drawback of nanomaterials, because many trap states are formed at the surface.[37] However, great progress in surface passivation techniques has led to nanostructures with low non-radiative recombination rates. For example, silicon nanostructures (black silicon) passivated by Al_2O_3[38] or SiO_2,[39] InP nanowires passivated by PO_x[40] and halide perovskite nanowires passivated by porous aluminum oxide templates[41] have all enabled PLQY values comparable to state-of-the-art bulk systems.

Both the radiative recombination rate and light outcoupling can be tuned with nanophotonic engineering. When comparing a planar device to a nanostructured device, many parameters are changed at the same time and it is difficult, if not impossible, to fully separate the different contributions to the final performance. A detailed (mathematical) analysis is beyond the scope of this paper. We will point out some of the effects that play a role.

The key parameter to which many of the optical properties of nanostructures relate, is the enhancement in light absorption. Initially this was mainly considered as a way to increase J_{sc}. However, it can also improve V_{oc} by increasing PLQY as given in equation (2.7). Absorption enhancement per unit volume leads to a higher density of excited charge carriers inside the material, i.e. higher injection level. The radiative recombination rate scales with the carrier concentration squared, while the trap state assisted non-radiative recombination rate scales only linearly with carrier concentration.[42] The non-radiative Auger recombination scales with carrier concentration cubed and starts to dominate at high injection levels.[42] Therefore Q_i^{lum} usually has a peak at finite carrier concentration; with higher carrier concentration leading to a loss in Q_i^{lum} because of Auger recombination and lower carrier densities leading to a loss because of enhanced trap state assisted non-radiative recombination.[42] Intelligent choice of doping concentrations and absorber layer properties may allow the device to be designed such that the optimum injection level is close to one sun conditions. The effect of enhanced Q_i^{lum} at higher injection levels can also be understood from reciprocity: a higher absorption rate means also a higher emission rate; for the same non-radiative rate this gives an increase in Q_i^{lum}.

Changes in light absorption, and thus light incoupling, will also influence the light outcoupling, and thereby p_e. Intuitively one can understand that when less absorbing material is needed, p_e will be larger in a nanostructured device: emitted light has to travel a shorter distance through the material before it reaches an interface where it can escape. Or again the reciprocity argument can be used: stronger coupling to incoming light, means stronger coupling to outgoing modes, which increases p_e.

The changes in Q_i^{lum} (via enhanced internal radiative rate) and p_e (via enhanced external radiative rate) are related to the same optical effects. Nanostructures can enhance the local density of optical states (LDOS) and they can enhance coupling to specific modes, which is equivalent to locally enhancing the field of incoming waves. Since these effects are coupled and influence both Q_i^{lum} and p_e, these parameters can not be tuned independently. In addition to that, the absorption and emission spectra will be altered by changes in LDOS and electric field strength. Often the consequential changes in V_{oc} are attributed to different parameters in an additive manner, but it has already been shown that in this additive form the different components are not independent.[43] By combining the additive terms in one equation (eq. 27 in[43]) this expression is claimed to contain only independent parameters. However, when considering nanostructures, several terms in this expression are still coupled via the LDOS and field enhancement. A general statement on how these effects change V_{oc} can therefore not be made. However, attempts to attribute changes in V_{oc} to specific parameters has led to some confusion, some of which we will try to resolve here.

In the first place, there is experimental proof of strongly increased V_{oc} and PLQY in nanostructured materials. By comparing a planar InP device to one with nanowires of the same material, an increase in V_{oc} of 70 mV was found due to a combination of enhanced absorption, increased Q_i^{lum} and increased p_e.[28] Light outcoupling enhancement via nanotexturing has also been used to improve methylammonium lead halide perovskite thin film solar cells. For the iodide perovskite, the PLQY was increased by more than a factor 5, by going from thin film deposition on a smooth glass substrate to a nanotextured substrate.[44] Also without fully quantifying and separating the contributions of the physical processes underlying these effects, it should be clear that nanostructures can improve the optical properties of a material.

One source of confusion is the fact that changing the optical properties of a material can also change the emission and absorption spectrum. This might lead to an effective increase or decrease in bandgap, resulting in a change in $V_{oc,rad}$. When only looking at the resulting voltage, one can come to the conclusion that p_e should be minimized, because this can lead to an effective increase in bandgap and therefore in V_{oc}.[45] However, this is only moving along the bandgap axis in figure 2.1, without actually getting closer to the radiative or SQ limit, as shown by the red arrow in figure 2.3. In the presence of non-radiative recombination, increasing p_e will lead to an increase in PLQY (green arrow in figure 2.3). Even though the absolute V_{oc} may decrease due to a lower effective bandgap, the radiative limit will be more closely approached. Intuitively this can be well-understood from the fact that any reabsorption of a photon (due to a low p_e) provides another chance for non-radiative recombination, which reduces the PLQY. Therefore p_e should always be maximized for approaching the radiative limit as long as absorption is not compromised.

Another source of confusion arises when looking at individual nanoparticles. Instead of an absorption spectrum, they are typically characterized by their absorption cross section σ_{abs} as a function of wavelength, defined as the effective area over which the particle absorbs light. The absorption cross section can be substantially larger than the geometrical size of the particle, which makes the standard definitions for solar cell performance not applicable.[46] In individual nanoparticles, $V_{oc,rad}$ and the radiative recombination rate can be changed over a very large range, which complicates fair comparisons between different systems. In figure 2.3, we show schematically the different situations that can be encountered. When σ_{abs} is increased equally for all wavelengths above the bandgap, the radiative rate is increased. This brings the system closer to the radiative limit, as indicated by the green arrow. As long as σ_{abs} is isotropic, the efficiency can not increase above the radiative limit, because $J_{0,rad}$ (the radiative saturation current density) and J_{sc} are increased by the same amount. To surpass the radiative limit, the expansion of etendue has to be reduced, which is the topic of the next section. This requires an angle dependent σ_{abs}[46] and as a consequence the whole radiative limit moves to higher efficiency for all bandgaps (dotted line). If σ_{abs} is increased more for some wavelengths than for others, the effective optical bandgap of the material is changed and one moves along the bandgap axis, indicated by the red arrow. Depending on whether the starting point is below or above the optimum bandgap, this increases or decreases efficiency. When an individual nanoparticle has a strong resonance at the bandgap, $V_{oc,rad}$ can actually be decreased significantly. The resonance strongly enhances emission and absorption at the bandgap only, by which J_0 is increased much more than J_{sc},[46,47] following the orange arrow. In a full scale solar cell, this would be equivalent to a device with full absorption at the bandgap, but much lower absorption at higher energy. Since a good performing solar cell should have full absorption anywhere above the bandgap, larger absorption rates at the bandgap than at higher energy are not desirable. By designing a structure with a both angular and wavelength-dependent absorption cross section, potentially very high efficiencies can be achieved, as shown by the green curve in figure 2.1. This will be discussed in more detail in the next section.

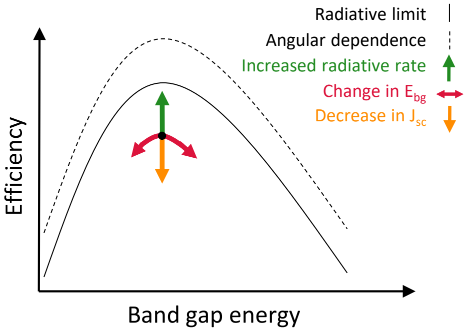

Figure 2.3: Nanostructures can affect the efficiency and V_{oc} in several ways, which occasionally leads to some confusion. Four effects can be distinguished: by enhancing the radiative rate, the PLQY can be increased, approaching the radiative limit (green arrow); the effective bandgap can be changed (red arrow); a resonance at the bandgap effectively decreases J_{sc} and $V_{oc,rad}$ (orange arrow); or the whole radiative limit can be increased by restricting the cone of emission (dotted line).

Throughout this section we have used the PLQY as a measure of solar cell voltage, relying on the reciprocity relation between light absorption and light emission. The critical reader might have noticed that this is technically incorrect, because the reciprocity relation links PLQY to the quasi-Fermi level splitting, while solar cell voltage is connected to the electroluminescence (LED) quantum efficiency. The PLQY and LED quantum efficiency are equivalent when assuming perfect contacts and infinite carrier mobility, but can be different for real materials.[48] However, in mature semiconductor systems, carrier extraction is close to perfect and for most materials, except for organics, the mobility is sufficiently high at one sun fluxes. In this case transport losses do not play a significant role, and the optically and electrically measured quantum efficiency are almost the same.[48,49,50] PLQY is the upper bound and is the one we influence with nanophotonics. We do not focus on carrier transport or carrier injection in this article and therefore use PLQY as a characteristic parameter. Experimentally, PLQY is also often more useful since it can be measured at every step of the solar cell fabrication, while the electroluminescence requires a complete device.

2.4 MATCHING THE ANGLES

The second loss mechanism that we discuss, is the mismatch between absorption and emission angles. This leads to an increase in photon entropy between the incoming and emitted light. Since the conventional SQ limit assumes isotropic emission, this limit can be exceeded by reducing the cone of emission. This leads to a decrease in the radiative recombination $J_{0,rad}$, by which $V_{oc,rad}$, and thus the efficiency, are increased. Emission and absorption are coupled via Kirchhoff's law, so emission into the cone of the sun can not be reduced without sacrificing J_{sc}. The sunlight comes from a cone with a 0.5 degree half angle, which allows for a maximal reduction of J_0 by a factor 46200, compared to emission into the full hemisphere. This corresponds to a maximum increase in voltage of 278 mV.

The most conventional way to reduce the loss due to etendue expansion is by using a concentrating lens. The light that comes directly from the sun is focused onto the cell, while the thermal radiation that comes from all angles is not focused on the cell. Or equivalently, the lens focuses the emission from the cell towards the sun. The resulting efficiency of the SQ limit with 46200 times concentrated AM1.5 spectrum is shown in figure 2.1, orange line. The maximum achievable efficiency is over 40%. However, in a typical terrestrial situation, part of the sunlight is scattered by clouds and surroundings. This light is not focused on the cell and as a consequence the absorption of this diffuse light decreases by the concentration factor. In many terrestrial applications, this decreases J_{sc} more than it increases V_{oc} and the efficiency decreases.

To see the consequences of this effect, we analyzed the impact of diffuse sunlight on conventional concentrating systems. We derived an expression for the relation between efficiency, concentration factor and fraction of direct sunlight. For a concentration factor X, both J_0 and the absorption of diffuse sunlight are reduced by a factor X. Plugging this into the equations for J_{sc} and V_{oc}, and simplifying the expression by neglecting small terms, it can be shown that efficiency approximately scales with concentration factor and fraction of direct sunlight as:

$$\eta \propto J_{sc} f_{dir} \left[ln\left(\frac{J_{sc}}{J_0}\right) + ln\left(f_{dir} X\right) + \frac{1}{X}\frac{1-f_{dir}}{f_{dir}} ln\left(\frac{J_{sc}}{J_0}\right) \right] \tag{2.9}$$

with J_{sc} and J_0 the short circuit and dark current for the cell without concentrating lens, respectively, and f_{dir} the fraction of direct sunlight. The derivation can be found in section 2.8.1. This equation shows that the concentration factor has both a positive ($ln(X)$ term), and a negative ($1/X$ term) effect on efficiency, which originate from the increase in V_{oc} and the decrease in J_{sc}, respectively.

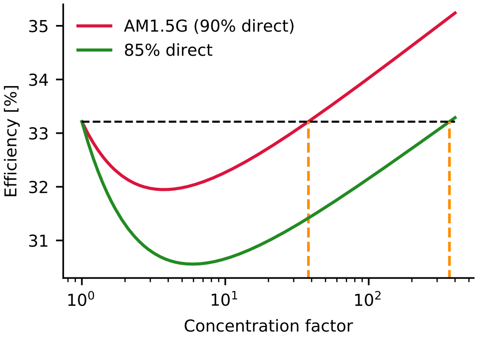

Figure 2.4: Efficiency as a function of concentration factor at a bandgap of 1.11 for different fractions of direct sunlight, calculated with equation (2.9). The black line indicates the efficiency at 1 sun and the orange lines indicate the break even points, above which the efficiency is increased due to the concentration.

We used this expression to calculate the efficiency as a function of concentration factor for a silicon solar cell, ignoring Auger effects. We used a bandgap of 1.1 eV and the AM1.5

spectrum, which contains 90% direct sunlight, and a modified version of this spectrum with 85% direct sunlight. Figure 2.4 shows how at low concentration the reduction in $J_{\rm sc}$ is dominant and the efficiency is decreased. Only above a certain threshold value for X_{thr}, concentration is beneficial. The lower the fraction of direct sunlight, the higher X_{thr} becomes. X_{thr} rapidly increases: by going from 90% to 85% direct sunlight, it increases from 40 to almost 400. Vice versa, the lower the concentration factor, the more direct sunlight is needed. The minimum required fraction of direct sunlight for a given X can be derived from equation (2.9) and reads:

$$f_{dir} = \left[1 + \frac{1}{ln(J_{sc}/J_0)} \frac{X ln(X)}{X-1}\right]^{-1}. \tag{2.10}$$

For the AM1.5 global spectrum, a bandgap of 1.1 eV and maximum concentration (46200x), at least 76% of the sunlight must be direct. For a more practically achievable concentration of 400x, the break-even point lies just below 85% direct sunlight. In many places on earth this value is not reached most of the time. In that case adding a concentrator will make the system perform worse. To get a feeling for the numbers: in the Netherlands the fraction of energy from direct sunlight is on average 36%, in Denver (Colorado, US) this is 76% and in the Sahara this is 80%.[51] The AM1.5G spectrum assumes a clear sky, but still contains 10% diffuse sunlight due to the presence of the atmosphere.

Instead of expanding the angular range of incident sunlight to match the angle of emitted light (as with concentrating lenses described above), it is also possible to reduce the emission angle of the solar cell towards that of the sun. This is done with angle restrictive filters, that block emission and absorption into oblique angles. This concept was described more than two decades ago,[23] and has been studied in order to find upper thermodynamic limits for PV systems since then.[43,52] When acting over the full solar spectrum, angle restrictive mirrors are mathematically equivalent to concentrating lenses and they can be described with an effective concentration factor. However, since emission occurs over a narrow bandwidth, the angle restrictive mirrors can be made wavelength selective. This way, the problem with diffuse sunlight can be circumvented: if the mirrors only block light at the emission wavelength, while they are transparent at higher energy, J_0 is decreased while maintaining high $J_{\rm sc}$. In practice however, PV systems with angle selective mirrors suffer from the decreased escape probability, which reduces the PLQY as discussed in the previous section(equation (2.8)) as a consequence of photon recycling. The resulting increase in $V_{\rm oc}$ for an effective concentration factor X and initial value of PLQY is given by $(k_B T/q) ln\{X/[X-(X-1)PLQY]\}$, which approaches zero as the initial PLQY goes to zero.[34] This approach was tried experimentally, using a high quality GaAs solar cell. Despite the high PLQY in GaAs the increase in $V_{\rm oc}$ was only a few mV due to the decrease in escape probability.[53]

As mentioned above, concentration and angle restriction are mathematically the same in the radiative limit and without considering diffuse sunlight. When you look at the combined system of solar cell plus concentrating lens or angle restrictor from the outside, both look the same: only incoming light at normal incidence is absorbed and only collimated light comes out. Both techniques have their limitations, and by combining the two losses can be minimized.[24,54] Concentrating lenses always act over the full spectrum, which leads to significant losses in any realistic operating conditions with diffuse sunlight. However, they do have the advantage of having good light outcoupling, which makes them also applicable to materials with a low PLQY like silicon. Angle restrictors allow for wavelength selectivity, but they work based on reduced light outcoupling. In some cases this can be beneficial, because this light trapping increases the absorption close to the bandgap, increasing Jsc for a given thickness.[55] However, this comes at the cost of increased non-radiative recombination, meaning that the efficiency will always be below the radiative limit for non-ideal materials. Since most work on controlling the emission angles has been focused on angle restricting filters on top of the solar cell, which enhance photon recycling and reduce escape probability, this has led to the misconception that any type of angle restriction only works for solar cells close the radiative limit. With nanophotonic structures this does not have to be the case: they change the emission event itself, instead of interacting with the light after it is emitted. Just like the efficiency of silicon cells can be increased with concentrating lenses, which effectively also change the angular profile of the emission, nanophotonic structures have the potential to improve efficiency also for materials with low radiative efficiency.[21]

Nanophotonic structures can combine the best of both worlds: maintaining high light-outcoupling as with concentrating lenses, while providing wavelength selectivity comparable to angle restriction filters. This requires directive nanoparticles: particles that emit and absorb more in one direction than in all others. This is described by the so called directivity, as used in antenna theory. It is defined as the maximum power absorbed or emitted into a certain direction divided by the average power in all directions. The particles must be directive over a narrow band width around the emission wavelength, and absorb high energy light from all directions. This gives both directive light emission (i.e. reduced emission loss) and good absorption of diffuse sunlight, while maintaining or potentially increasing the escape probability. The resulting efficiency of such system, with the band width of directivity optimized at each bandgap, is shown in figure 2.1, green line.

To achieve these efficiencies, one must have accurate control over the light emission. In the field of nanophotonic engineering several methods have been developed for controlling the emission at the nanoscale. Especially in the field of single photon emitters there is a large demand for increasing the brightness, enhancing the Purcell factor and controlling the directivity.[20] A frequently studied system is the Yagi-Uda antenna. On macroscopic scale this is a well-known antenna design used for radio frequencies. By scaling it down to the nm size, light emission of a single quantum dot can be controlled. Using five gold elements a forward-to-backward ratio of the emission of 4.7 dB has been experimentally achieved.[56] Another well-known geometry is the Bull's eye antenna, which consists of concentric rings or grooves around the emitter(s). With shallow grooves in a gold film a directivity of 7.5 dB was measured from an ensemble of particles.[57] Coupling emitters to plasmonic resonances in an array of aluminum nanoantennas, gave a more than 60-fold directional enhancement for the purpose of efficient light-emitting diodes.[58] By introducing spatial variations in an array of nanoantennas, wavefront shaping with sub-wavelength resolution can be achieved, which is being used for the development of flat optics or metalenses.[59]

All of the above mentioned systems rely on plasmonic nanostructures. The main disadvantage of plasmonic structures is the parasitic absorption in the metals. This realization has led to a shift away from lossy metallic (plasmonic) resonators towards dielectric systems. Here many of the nanophotonic advantages are still present, but without the parasitic absorption.[60] For example, a hybrid system of a titania Bull's eye structure on a silver film was realized, which gave emission into two lobes with full-width-half-max of 3 degrees.[61] An all-dielectric Yagi-Uda nanoantenna was fabricated from silicon spheres, reaching a maximum directivity above 7 in the microwave range.[62] Also in the field of metalenses the low efficiency associated to the dissipative losses in metals has led to the development of all-dielectric metasurfaces, which show good potential for replacing their plasmonic counterparts.[63]

For the performance of solar cells, parasitic absorption is detrimental for both current and voltage. Initially, work has been done on plasmonic structures for solar cells, mostly to enhance absorption in the solar cell material.[64] Since it became clear that the parasitic absorption in the metals will limit the achievable efficiencies, the attention has now shifted to dielectric nanostructures.[18]

Of course the dielectric materials have their own possibilities and challenges. An advantage is, that dielectric nanoparticles can support both electric and magnetic resonances simultaneously, which can be controlled independently.[60] On the other hand, these resonances are usually less localized than in metals, leading to more broadband response and lower directivity. Fabrication imperfections are challenging in any nanoscale structure and cause sub-optimal geometries and rough surfaces. Insufficient surface passivation has further decreased the performance of dielectric nanophotonic structures so far. Both theoretical and experimental work is to be done on improving light management with dielectric nanostructures and developing pathways to large-scale applications.

A specific example of the kind of design requirements is the angular and wavelength dependent absorption and emission profile needed for the reduction in etendue. For a material with a bandgap at 860 nm (e.g. GaAs), the ideal absorption cross section as a function of angle and wavelength is shown schematically in figure 2.5. The structure must have high absorption at normal incidence, to collect the direct sunlight efficiently, and high absorption from all directions at high energy, to maximize absorption of diffuse sunlight. Close to the bandgap, away from normal incidence the absorption should be low, which makes the emission directional towards the sun. Radiative recombination should be enhanced, while parasitic absorption must be avoided.

To realize such particles, morphologies have to be found and fabricated that lead to anisotropic absorption cross sections. Finding the optimal shape for highly directive particles is a non-trivial nanophotonics problem. Either the absorber material itself can be made into a directive structure, or nanoantennas of dielectric material can be placed around or on top of the semiconductor. The directivity of GaAs nanowires has been increased from 2 to 20 by placing a 'nanolens' on top of the wire. The nanophotonic structure of the lens was designed through an evolutionary algorithm and fabricated using two-photon lithography.[65] For future large-scale application, faster fabrication methods are needed, based on chemical growth or self assembly. A good candidate might be the shape-preserving transformation of carbonate minerals into semiconductors. Carbonate minerals can mineralize into three dimensional shapes in a well controlled manner. Subsequently the structure can be transformed into, for example, methylamonium lead halide perovskite, which is a good solar cell material.[66]

Potentially, high directivities can be reached by combining different effects. For example, it may be possible to place the directive nanolenses in an array that provides additional

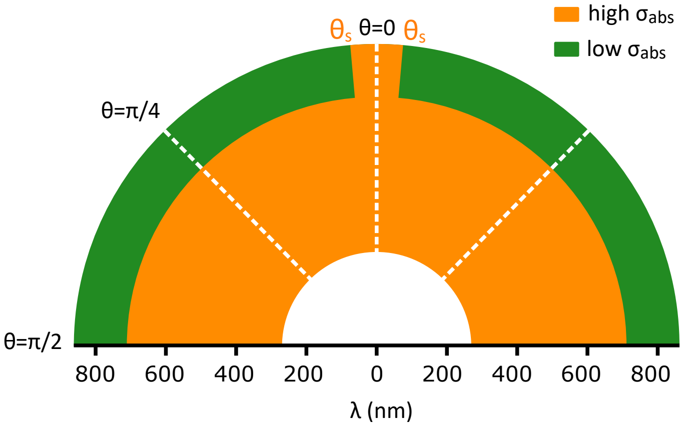

Figure 2.5: Schematic illustration of how the absorption cross section (σ_{abs}) of a nanostructure should vary with wavelength and angle of the incoming light in order to achieve the narrow band directivity. Around the bandgap the nanoparticle should be directive, such that it emits light in the direction of the sun. This requires higher absorption for normal incidence than for oblique angles. At energies further above the bandgap it should absorb light from all directions, to also capture diffuse sunlight.

directivity. Another option is to choose specific emitter materials with intrinsic directional emission, due to preferred dipole orientation[67,68] and combining this with nanolenses or array effects, or both. To achieve the wavelength selective directivity different materials or molecules with specific dipole orientation must be combined and coupled.

2.5 MATCHING THE SPECTRUM

The biggest loss mechanism that applies to all single junction solar cells, is the mismatch in absorption and emission spectrum. For the typical silicon solar cell, as analyzed in figure 2.2, this contributes to an absolute loss of 42% in efficiency. All photons below the bandgap are not absorbed, which accounts for 16% of the loss, and all excess energy of above-bandgap photons is dissipated as heat, thereby losing the remaining 26% of efficiency. There are several techniques available to reduce these losses. In this section we will discus the ones that can benefit from nanophotonics.

A luminescent solar concentrator (LSC) consists of a plate or sheet of transparent material with embedded luminescent particles. These particles absorb the sunlight and subsequently emit light, which is then waveguided through the plate. Small solar cells connected to the waveguide absorb the light and convert it to electricity. Although this system has the name concentrator, it can not increase the efficiency above the SQ limit like the concentrating systems discussed previously. This can be understood from the fact that the thermal emission to the environment is not directed towards the sun, and thus the entropy loss remains. However, LSCs have several advantages, both economical and physical, and nanophotonics can help to improve their performance.

The economical benefit of using an LSC is that the transparent plate with luminescent particles can be cheap and easy to fabricate: existing cover glasses or polymer coatings used in the solar cell industry can already fulfill the role of a waveguide. The actual solar cells to which the light is guided are very small compared to the collection area. This small size makes expensive, high efficiency solar cells affordable. LSCs can potentially create high efficiency devices, because they can be used in tandem configurations for better capturing of the full solar spectrum. Conventional multi-junction solar cells are complex and expensive to fabricate, because many additional layers are required to accommodate the lattice mismatch, charge transport and surface passivation. The cells are usually connected in series, which limits the current to the lowest current in one of the cells. Stacking LSCs with different bandgaps is less complex, and the cells do not need to be current matched. This makes the tandem less sensitive to temperature and spectral fluctuations and easier to fabricate. Promising results have been found in both theoretical[69] and experimental[70] work on the performance of LSC-tandem configurations.

Nanophotonics engineering is already being used for optimizing the absorption and emission spectra of the luminescent particles in LSCs. With Stokes shift engineering, i.e. the shift between absorption and emission spectrum, reabsorption in the waveguide can be reduced. By properly matching the emission to the absorption of the solar cells, efficiency can be increased. In a tandem configuration the bandgaps of the different layers can be accurately tuned for optimal performance, by using quantum confinement or resonances to change the effective bandgap of the material. However, the main challenge for making high efficiency LSCs is to achieve efficient guiding of the emitted light towards the solar cells. Many photons are often lost along the way, due to non-radiative recombination in the particles, or because they are emitted into the escape cone of the waveguide. The light that is coupled to the waveguide, is often reabsorbed many times along its way. Each reabsorption event leads to another chance of non-radiative recombination or emission into the escape cone.

With nanophotonic engineering, particles can be designed that minimize the losses in the waveguide. By creating directive emission into the plane of the waveguide, the fraction of light emitted into the escape cone can be reduced significantly. It has been proposed to use for example photonic structures to enhance in-plane emission and reduce escape cone losses.[71] By creating aligned directive emission into only one direction, also the chance of reabsorption can be reduced: the structures emit light mostly in one direction (say towards the right), but due to reciprocity they mostly absorb light traveling to the left. This leads to a structure in which light can travel only in one direction. The structure requires a lower directivity than the nanolenses in the previous section: as long as the light is emitted into the cone of total internal reflection of the waveguide, the photons do not escape. The required absorption cross section as a function of angle and wavelength is schematically shown in figure 2.6. Again, at short wavelengths (high energy) the absorption should be high from all directions, to maximize absorption of sunlight, and the particles should be only directive over their emission spectrum.

Another system that reduces the spectral mismatch and that can benefit from nanophotonic engineering, is a photon multiplier. In this concept, high energy photons are converted to two low energy photons. This process takes place in the so-called down converter layer on top of a solar cell, from which the photons have to be emitted towards the solar cell. This down conversion can be realized with singlet fission[72] or multiple exciton generation.[73,74,75] The efficiency of this type of devices can be increased by coupling the down

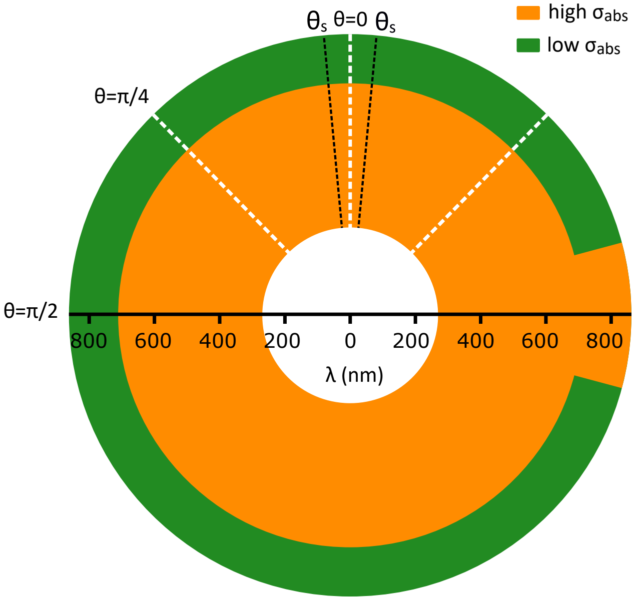

Figure 2.6: Schematic illustration of how the absorption cross section (σ_{abs}) of a nanostructure should vary with wavelength and angle of the incoming light for the emitters in the LSC waveguide. The emission around the bandgap should occur primarily within the cone of total internal reflection, which requires low σ_{abs} in all other directions. At energies higher above the bandgap σ_{abs} should be large to absorb the incoming sunlight from all directions.

converter to directive emitters. This will ensure that the down converted light is emitted towards the solar cell.

Finally, nanostructures can form an alternative configuration for tandem or multi-junction solar cells. Instead of placing layers that absorb different parts of the solar spectrum on top of each other, spectral splitting can be achieved by placing nanostructures next to each other. Thanks to the enhanced absorption cross section of nanowires, adjacent wires with different bandgap can collect light from an overlapping area. Spectral splitting can be achieved by making high bandgap nanowires taller, such that the high energy photons are absorbed before they reach the lower bandgap material wires,[76] or by making use of structures with different resonance frequencies, which cause an enhancement in absorption cross-section at specific frequencies.[77]

2.6 Future solar cells

In this section we propose two concepts for high efficiency solar cell designs, based on the approaches discussed in the previous sections. In the first design, a high efficiency is reached by reducing the cone of emission while maintaining high J_{sc} and p_e by using narrow-band directive nanostructures. The second design combines existing bifacial silicon solar cells with a luminescent solar concentrator, which leads to a low cost, high efficiency tandem device. The performance of each design is evaluated in realistic operating conditions using measured solar spectra, and compared to a more conventional design without nanophotonics.

2.6.1 Narrow band directivity nanolenses

The first concept aims at a reduction in emission cone, high light outcoupling and good absorption of diffuse sunlight. This is achieved with nanostructures that emit the light into one specific direction, rather than using structures that redirect the light after emission, such that directivity does not come at the cost of light outcoupling. The constituent nanostructures should have an absorption cross section varying with incidence angle and wavelength as shown in figure 2.5. The optimal bandgap for this concept is 1.1eV, as can be seen in figure 2.1. We assume a high quality solar cell material in combination with good light outcoupling to give a PLQY of 85%. This could be achieved with, for example, an alloy of III-V or halide perovskite materials, which provide tunable bandgap and high PLQY. For comparison with state of the art concentrators, we propose a directivity of 400, similar to existing record concentrating solar cells. The optimum band width of the directivity was found to be 0.22 eV, based on simulations with the measured solar spectra. This design is compared with solar cells of the same material (bandgap of 1.1eV and 85% PLQY), without concentration and with macroscopic concentration over the full band width.

With these parameters the performance of the cells can be calculated for any given solar spectrum. The spectra were taken from publicly available measurements from NREL in Denver,[78] measured every 5 minutes throughout the year 2018. Measurements of the direct solar spectra are readily available (SRRL PGS-100 Direct Normal). The diffuse solar spectra could be calculated using the direct spectra, the global horizontal measurements (SRRL WISER Global or Direct) and the azimuth angle of the sun. The temperature of the cell, used in the calculation of J_0, was approximated by the locally measured temperature (Dry Bulb Temperature (deck)). For each spectrum and cell temperature, a detailed balance model is used to determine J_{sc} and J_0, and from these the maximum efficiency is calculated. The results are presented in figure 2.7, showing the increase in efficiency compared to the cell without concentration or directivity, plotted versus fraction of direct sunlight. For low fractions of direct sunlight, macroscopic concentration performs very poorly, as expected from equation (2.10). The efficiency based on annual energy yield is 31.8%, which is a relative decrease of 5% compared to the standard cell (33.6%). This difference is smaller than it might seem from figure 2.7. This is because in general low fractions of direct sunlight correspond to low total incoming power, so the absolute loss in generated power is limited. The narrow band directivity concept outperforms the standard cell over the whole range and the annual energy conversion efficiency is 38.7%, a relative increase of 15% compared to the standard cell. This concept does not suffer from high fractions of diffuse sunlight, which shows the importance of having high directivity only over a narrow band width.

There are still several challenges that need to be solved to realize this concept. As suggested in the section on matching the angles, directive nanostructures can be made in different ways, both from the semiconductor itself or from a dielectric nanolenses on top of the semiconductor. A cheap and fast fabrication technique for directive structures has to be found. A question is whether it is possible to obtain the desired directivity with a texture on a planar film, or by using diffractive effects. Another question is what happens when directive structures are placed in an array and the enhanced absorption cross sections

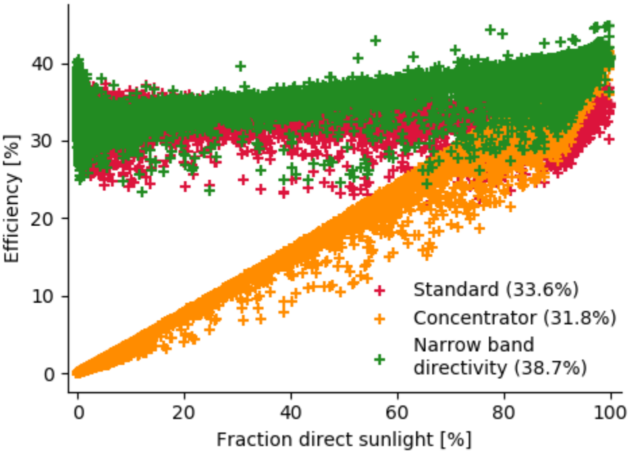

Figure 2.7: Performance of a conventional concentrator system and narrow band directivity system compared to a cell without concentration. The efficiency is plotted as function of the fraction of direct sunlight and the simulations are based on measured solar spectra.[78] The values in brackets indicate the average efficiency over the year. The concentrator reduces the efficiency by 2.7%, while the narrow band directive structures increase efficiency by absolute 7.7%

start to overlap at certain wavelengths or angles. Also fundamental questions need to be solved, to show if there is a limit on directivity in nanostructures or if there is a trade off between directivity, LDOS and light outcoupling. It has to be shown, both theoretically and experimentally, whether the required emission patterns can be achieved. High directivity into a narrow cone requires accurate 2-axis solar tracking: one 'fast' moving rotation to follow the arc of the sun throughout the day and one slow rotation to adjust the axis throughout the year. If a directive structure can be made that emits into a band matching the arc of the sun, tracking throughout the day could be eliminated, allowing for the widely available and inexpensive single axis tracking to be used. These questions and more require further research to nanoscale directivity.

2.6.2 Bifacial LSC-Si tandem device

The second concept aims at combining cheap and well established silicon solar cells with new techniques. We propose a bifacial tandem configuration, where a high bandgap LSC is placed on both sides of a bifacial silicon panel. This concept combines the existing design of silicon cells with a yet to be developed LSC and solves several problems at the same time.

Currently the industry of silicon cells is moving towards bifacial cells, which can also absorb sunlight from the back side. This can give a significant increase in energy output per panel, especially in regions with large fractions of diffuse sunlight. To increase energy output even further, the efficiency has to be increased. As discussed in relation to figure 2.2, silicon solar cells perform close to their limit, and improving efficiency requires new measures. The biggest gain can be found in going to a tandem configuration, with a high bandgap material on top of the silicon. As mentioned before, conventional tandem cells are expensive to fabricate and suffer from current matching. Using an LSC can potentially be a very cheap solution. Standard silicon solar cells already have a encapsulation layer, that could serve a dual purpose as an LSC, without adding a fabrication step to the module assembly. Currently existing LSCs suffer from low efficiency and this is the main challenge that might be solved with directional emission from nanostructures in the LSC.

A typical solar cell module consists of an array of silicon wafers. For monocrystalline silicon, these wafers are cut from a cylindrical ingot. The packing efficiency in a panel is increased by cutting the circular wafers into squares. To limit the waste of material, the squares are cut slightly too big, which leads to 'missing' corners that are typically visible on the modules. We propose to place the high bandgap cells of the LSC in these empty squares of the module. For standard silicon cells used in industry (commonly called 6-inch wafers) the missing corners form a fraction of 0.6% of the total area. This gives a concentration factor of 170 for the LSC. In figure 2.8 the layout is shown schematically. For the small, high bandgap cells, high efficiency III-V materials can be used. These are expensive, but the concentration of the LSC reduces the price by factor 170. By placing them in between the c-Si cells, there is no need for lattice matching or wafer bonding.

Aligned directive nanostructures, with an absorption cross section as depicted in figure 2.6, are used to optimize emission into the waveguide and to minimize reabsorption. The exact requirements on the absorption cross section depend on several parameters, like the refractive index of the waveguide (and thus the escape cone), the PLQY of the emitters, the Stokes shift and the scattering cross section. Fully modeling this is beyond the scope of this paper. A simple parameter that captures several effects is the internal efficiency Q_{int} that gives the ratio of the number of photons that reach the LSC solar cells compared to the number of photons absorbed in the LSC (sometimes also called the optical quantum efficiency in the LSC community). This parameter accounts for the major loss mechanisms in an LSC: photons escaping the waveguide and photons lost due to non-radiative recombination, including the effects of reabsorption along the way. We use this parameter to take into account the directive emission in the modeling of the performance of the LSC-tandem concept: a high Q_{int} corresponds to high directivity, because this reduces reabsorption and escaping of photons.

To simulate the performance of this concept, several parameters have to be quantified. For the bifacial silicon cell a PLQY of 1% and a step wise bandgap of 1.1eV are assumed. The optimum bandgap of the LSC was found to be 1.75 eV through optimization with measured solar spectra. The high bandgap cells are modeled to have an PLQY of 85%. Different values of Q_{int} have been evaluated. If less than three quarters of the photons absorbed in the LSC are collected, it performs worse than the current matched tandem. If less than half of the photons are collected, the performance is worse than only the bifacial silicon cell. Here we model the performance of a system with $Q_{int} = 90\%$. We assume that the back side of the bifacial cell receives 75% of the diffuse sunlight. For a bifacial silicon panel without LSC this gives a yearly increase in energy output of 15%, compared to a monofacial cell. Some long running field tests with bifacial cells have shown an increase between 10% and 20%, so the increase of 15% is a realistic approximation.[79] The performance of the LSC-Si tandem is compared with a current matched tandem, with the same bifacial silicon bottom cell, but no tandem on the back. The top cell has again a bandgap of 1.75eV and an PLQY of 85%.

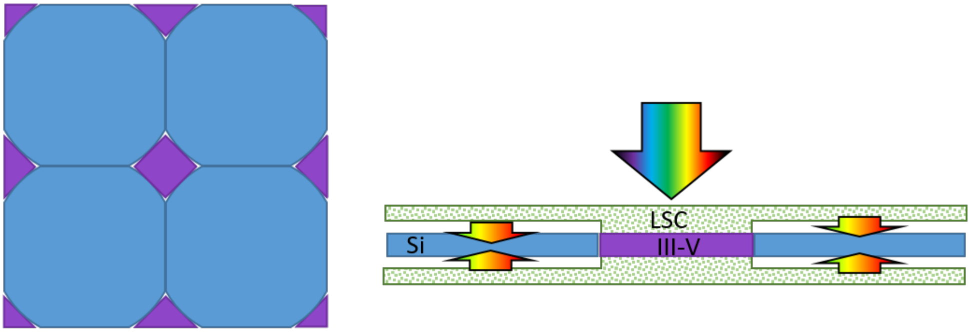

Figure 2.8: Schematic layout of the LSC-Si tandem configuration, where the high bandgap cells sit in the gaps between the silicon wafers. The connection between the LSC and the small solar cells must be index matched, such that the waveguided light leaks out and couples into the cell.

With these assumptions the performance is again calculated based on the measured solar spectra[78] by simulating the tandem devices in a detailed balance model. The results of the simulation are shown in figure 2.9, where the performance is plotted relative to a single junction bifacial cell. In this case the efficiency is plotted versus the mean wavelength of the spectrum. Spectral shifts reduce the performance of current matched tandem, because the current is determined by the minimum current in either of the two cells. If the spectrum is red-shifted, the current in the high bandgap cell decreases. The blue shifted spectra correspond to high fractions of diffuse sunlight. In this case the reduced current in the Si bottom cell due to the blue-shift, is compensated with the contribution of diffuse sunlight on the back side and the efficiency remains high. The yearly energy output compared to standard bifacial panel is increased by an absolute 9.2%, which is a 28% relative increase.

The bifacial LSC-tandem configuration exceeds the performance of the two others at almost every spectrum. The yearly energy output is increased by 13.3% compared to the single junction bifacial cell and 4.1% compared to the current matched tandem, relative increases of 41% and 10% respectively. It benefits from the increased efficiency of a tandem device, without current losses and with less complex manufacturing. This shows the great potential of optimized LSC-tandem configurations.

The performance of the systems is given as a relative efficiency compared to a reference bifacial cell. We want to mention that the efficiency of a bifacial device is ill-defined without specifying the environment around the cell, PV packing density, and other geometric factors. The great benefit of bifacial configurations is the fact that they can harvest diffuse sunlight that is scattered from elsewhere. When the efficiency is calculated based on the incident sunlight per unit area, this can lead to apparently very high efficiencies at high fractions of diffuse sunlight, because light is effectively harvested from a larger area. This leads to seemingly unrealistic results when reporting absolute efficiencies, and therefore it is more insightful to look at the relative performance of the three systems.

For this concept the same questions apply regarding directive nanostructures as for the first design. A detailed modeling of the aligned nanolenses in a waveguide must be done to show whether asymmetric transmission can be achieved. One possible problem could

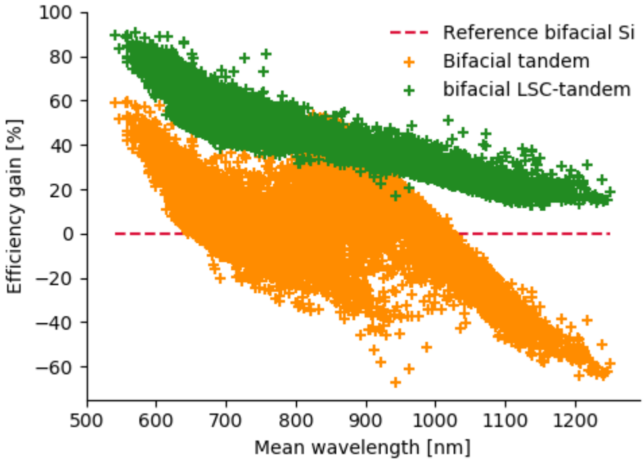

Figure 2.9: Relative performance of a bifacial current matched tandem and a bifacial LSC-tandem configuration compared to a bifacial silicon solar cell. The relative performance is plotted as function of the mean wavelength in the spectrum and the simulations are based on measured solar spectra.[78] The current matched tandem and the LSC tandem show an absolute increase of 9.2% and 13.3% in power generation compared to the bifacial silicon cell, respectively.

be the scattering of light in undesired directions, but some preliminary modeling showed that the transmission of directive nanolenses is high and that less than 10% of the light incident on the back (low absorption) side is scattered backwards. Furthermore techniques need to be developed to make waveguides with aligned nanostructures and couple them to solar cells.

2.7 Conclusion

In this Perspective article we gave an overview of how nanomaterials can increase solar cell efficiency. Nanomaterials have a great potential due to their strong and tunable interaction with light, originating from their size being comparable to the wavelength of light. This allows for controlling the emission event itself, instead of manipulating the light after it has been emitted, which is a key difference compared to macroscopic approaches. In this article we covered the different aspects in which nanomaterials can play a role in increasing solar cell efficiency. To do so we took a step back and looked at the fundamental properties needed to make a good solar cell. From thermodynamics we learned that an ideal solar cell in open circuit should emit all light back to the sun. This shows the importance of good light management, not only to optimizing absorption, but also making good, defect-free materials and applying nanophotonic engineering to accurately control the emission. By comparing a typical silicon solar cell to the idealized thermodynamic model we identified three differences in the emitted light: the spectral band width, the intensity and the angular emission profile. Each of these cause a reduction in V_{oc}, while J_{sc} is only mildly affected. This is also seen in record solar cells: while J_{sc} approaches the theoretical limit, V_{oc} is typically lagging behind. This perspective focuses on ways to increase V_{oc} with nanomaterials, because this field has only recently emerged and is rapidly developing.

For each of the three loss mechanisms we gave an overview how nanomaterials can help in reducing the losses. We have pointed out what has been achieved so far and what the remaining challenges are. Finally we applied this knowledge in two conceptual solar cell designs. We showed that with nanostructures that reduce the cone of emission while maintaining sensitive to diffuse light, the performance in terrestrial application can be increased by 15%. A conventional, macroscopic solution will actually decrease performance by 8% due to its low performance in the presence of diffuse sun light. A bifacial LSC-tandem configuration based on nanophotonic structures can increase performance compared to a bifacial silicon cell by 41%, while a more conventional current matched tandem gives an increase of 28%. Further development in designing and fabricating nanostructures for accurately optimized light management has the potential for contributing to high efficiency solar cells at low cost.

2.8 SUPPORTING INFORMATION

2.8.1 DERIVATION OF EFFECT OF CONCENTRATION

The maximum efficiency of a solar cell is given by the power output devided by the incident solar power. The power output is given by the product of the V_{oc}, J_{sc} and the fill factor. In this approximation we will only consider the effect of concentration on V_{oc} and J_{sc}, so we can write:

$$\eta \propto V_{oc} \cdot J_{sc} \tag{2.11}$$

The open circuit voltage scales with the logarithm of J_{sc} over J_0:

$$V_{oc} \propto ln(\frac{J_{sc}}{J_0}), \tag{2.12}$$

and J_{sc} and J_0 are finally the ones that depend on the concentration factor X:

$$J_{sc} = J_{dir} + \frac{J_{dif}}{X}, \tag{2.13}$$

where J_{dir} is the photon current corresponding to the photon flux of direct sunlight, and J_{dif} the photon current corresponding to the photon flux of diffuse sunlight. A concentrating lens or angle restriction filter blocks part of the diffuse sunlight, decreasing it with a factor X. The dark current J_0 is as a whole reduced by factor X:

$$J_0 = \frac{J_{0,0}}{X} \tag{2.14}$$

Filling in equations (2.12) to (2.14) into equation (2.11) gives:

$$\eta \propto ln\left(\frac{J_{dir} + \frac{J_{dif}}{X}}{\frac{J_{0,0}}{X}}\right) \cdot \left(J_{dir} + \frac{J_{dif}}{X}\right) \tag{2.15}$$

We assume that the fraction of current due to direct sunlight is proportional to the fraction of direct sunlight, such that the fraction of direct sunlight f_{dir} can be calculated as:

$$f_{dir} = \frac{J_{dir}}{J_{sc,0}}, \tag{2.16}$$

J_{dif} and J_{dir} always add up to $J_{sc,0}$, the total current without concentration, such that $J_{dif} = (1-f_{dir})J_{sc,0}$. This allows us to write equation (2.15) as

$$\eta \propto ln\left(\frac{f_{dir}J_{sc} + \frac{(1-f_{dir})J_{sc}}{X}}{J_0/X}\right)\left(f_{dir}J_{sc} + \frac{(1-f_{dir})J_{sc}}{X}\right) \tag{2.17}$$

Reorganizing the terms gives:

$$\eta \propto f_{dir}J_{sc,0}\left[ln\frac{J_{sc}}{J_0} + ln(f_{dir}X + 1 - f_{dir})\right]\left(1 + \frac{(1-f_{dir})}{f_{dir}}\frac{1}{X}\right) \tag{2.18}$$

The value of f_{dir} is smaller than 1, while X is always equal to or larger than one. In most cases $X \gg r$, so for typical values of $J_{sc,0}/J0,0$, we can simplify equation (2.18) by assuming $ln(f_{dir}X + 1 - f_{dir}) \approx ln(X)$ to get:

$$\eta = f_{dir}J_{sc,0}\left[ln\left(\frac{J_{sc,0}}{J_{0,0}}\right) + ln\left(f_{dir}X\right)\right]\left[1 + \frac{1-f_{dir}}{f_{dir}}\frac{1}{X}\right] \tag{2.19}$$

Working out the brackets and noting that $\frac{1}{X}ln(X)$ is much smaller than the other terms we get

$$\eta \propto J_{sc}f_{dir}\left[ln\left(\frac{J_{sc}}{J_0}\right) + ln\left(X\right) + \frac{1}{X}\frac{1-f_{dir}}{f_{dir}}ln\left(\frac{J_{sc}}{J_0}\right)\right] \tag{2.20}$$

The validity of the simplifications was checked by comparing the outcome of this expression with a numerical simulation. The resulting efficiency with increasing the concentration factor was calculated for a bandgap of 1.1 eV with the AM1.5 spectrum, which contains ca. 90% direct sunlight. The result is shown in figure 2.10, with in blue the efficiency as calculated numerically with a Shockley-Queisser type of calculation, and in orange the outcome of the analytical expression of equation (2.20). The two calculations show good agreement, so equation (2.20) can be used to draw conclusions about the performance of concentrating systems in terrestrial applications.

2.8.2 Modeling of solar cells under realistic operating conditions

Data preparation

From the NREL website the following data sets were downloaded:

- Direct solar spectra: SRRL PGS-100 Direct Normal
- Global horizontal spectra: SRRL WISER Global or Direct
- Temperature: Dry Bulb Temperature (deck)
- Zenith angle of the sun using the free calculation tool

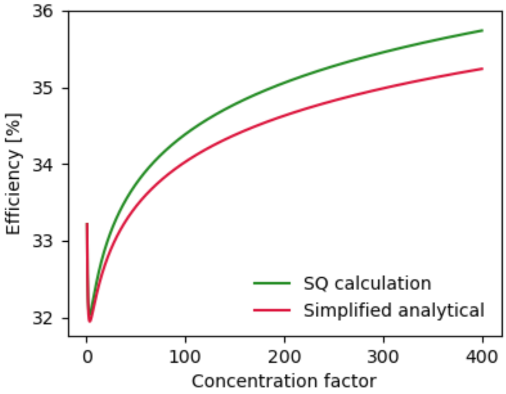

Figure 2.10: Efficiency as a function of concentration factor at a bandgap of 1.11 for the AM1.5 spectrum, blue line corresponds to the numerical SQ-calculation, orange is the results of equation (2.20)

The solar spectra are taken every 5 minutes, while the temperature data set contains measurements every minute. Also some data points are missing in the solar spectra data sets. A script was written that matches the four data sets and keeps only those data poins that are present in all four data sets.

The direct solar spectra run from 334 nm to 1075.4 nm. The global horizontal spectra run from 290nm to 1650nm. To obtain realistic values for the calculated efficiency, the spectra should contain higher wavelengths, like the AM1.5 spectrum that runs to 4000nm. Therefore the long wavelength tail of the AM1.5 spectrum is appended to the measured spectra, weighted by the average power in the last 100 data points of the measured spectra (i.e. 1000 to 1075 nm for the direct spectra and 1550 to 1650 nm for the global spectra). After appending this long wavelength tail, all spectra are interpolated over the wavelength range from 334 to 4000 nm at 1 nm step size.

EFFICIENCY MODELING

The efficiency is calculated based on the Shockley-Queisser model. Using the equation:

$$J = J_0(e^{\frac{qV}{k_BT}} - 1) - J_{sc} \tag{2.21}$$

The J-V curve is constructed for a given J_{sc} and J_0. The efficiency is calculated from the maximum power point and the given input power. J_0 is calculated by integrating the photon flux of the black body emission spectrum above the bandgap, assuming a step wise bandgap. J_{sc} is calculated as the integral over the solar spectrum at all energies above the bandgap in terms of photon flux.

The standard cell J_{sc} is calculated from the sum of the direct and the diffuse spectrum. For the conventional concentrator, the contribution of diffuse sunlight is reduced by the concentration factor X, and J_0 is reduced by factor X. For the narrow band directivity model, only J_0 is reduced by factor X.

For the bifacial silicon cell, J_{sc} is calculated using a total incoming flux of the direct sunlight plus 175% of diffuse sunlight, corresponding to 75% diffuse sunlight on the back side.

For the current matched bifacial tandem, the top cell receives just the sum of the direct and diffuse spectra. The silicon bottom cell receives all that is not absorbed by the top cell, plus 75% of the diffuse spectra from the back. In the LSC model the high bandgap cell is on both sides and receives the direct plus 175% diffuse light and the silicon cell receives everything that is not absorbed in the top cells.

The fraction of diffuse sunlight is calculated from the incoming power in the spectra, weighted by the total incoming power. The mean wavelength is calculated with:

$$\lambda_{mean} = \frac{\int P(\lambda)\lambda \, d\lambda}{\int P(\lambda) d\lambda} \tag{2.22}$$

where $P(\lambda)$ is the spectrum in watts per square meter per wavelength.

3

INTEGRATING SPHERE FOURIER MICROSCOPY OF HIGHLY DIRECTIONAL EMISSION

Accurately controlling light emission using nano- and microstructured lenses and antennas is an active field of research. Dielectrics are especially attractive lens materials due to their low optical losses over a broad bandwidth. In this chapter we measure highly directional light emission from patterned quantum dots (QDs) aligned underneath all-dielectric nanostructured microlenses. The lenses are designed with an evolutionary algorithm and have a theoretical directivity of 160. The fabricated structures demonstrate an experimental full directivity of 61±3, three times higher than what has been estimated before, with a beaming half-angle of 2.6°. This high value compared to previous works is achieved via three mechanisms. First, direct electron beam patterning of QD emitters and alignment markers allowed for more localized emission and better emitter-lens alignment. Second, the lens fabrication was refined to minimize distortions between the designed shape and the final structure. Finally, a new measurement technique was developed that combines integrating sphere microscopy with Fourier microscopy. This enables complete directivity measurements, contrary to other reported values, which are typically only partial directivities or estimates of the full directivity that rely partly on simulations. The experimentally measured values of the complete directivity were higher than predicted by combining simulations with partial directivity measurements. High directivity was obtained from three different materials (cadmium-selenide based QDs and two lead halide perovskite materials), emitting at 520nm, 620nm and 700nm, by scaling the lens size according to the emission wavelength.

3.1 INTRODUCTION

Controlling the direction of light propagation is an important element in modern technologies. It is used in energy, lighting and information technologies to increase device efficiency. An important metric for defining how well the light is focused in a specific direction, is the directivity, borrowed from classical antenna theory. It is defined as the maximum intensity into the beaming direction, divided by the average intensity[80] (equation (3.1), as we will discuss in more detail there). On the macroscopic scale, light is typically directed with curved lenses and mirrors, which make use of refraction and reflection. Nanoscale structures, with sizes similar to the wavelength of light, work in a fundamentally different manner, by relying additionally on diffraction and interference effects to control the light. These effects also naturally result in wavelength selectivity and by combining the traditional refraction/reflection effects with diffraction/interference effects the bandwidth can be adjusted. This is an important aspect in nanophotonic design. Directional light emission has been shown to increase the efficiency of LEDs,[58, 81, 82, 83] single photon emitters,[20, 84] photonic circuits[85, 86] and solar cells.[87]

Different methods have been developed to control the direction of light with nanostructures.[88] Especially structures made of dielectric material are of interest, because they do not suffer from the parasitic absorption that is inherent to plasmonics.[60, 89] Zone plates, which consist of concentric rings with spacings similar to the wavelength, focus light based on diffraction rather than refraction used in conventional curved lenses.[90, 91] Metasurfaces, with nanoscale patterns far below the wavelength of light that modify the optical phase, have been designed to make flat lenses, enhance light emission and control its direction.[92, 93, 94] Relatively simple shapes like micro or nanospheres can also give rise to directional emission: an emitter embedded asymmetrically in a lossless sphere can give a directivity of 7.5.[46] By placing silicon dioxide nanoparticles on a mirror, surface enhanced Raman scattering showed an increase in enhancement factor of 250 through the combination of plasmonic and refractive effects on both excitation and emission efficiency.[95] Numerical simulations have shown directivity up to 11 from nitrogen vacancy centers in diamond with all-dielectric spherical nanoantennas on top.[96]

To achieve higher directivity, shapes more complex than simple spheres have to be used. Ideas of more versatile nanoantenna designs used with plasmonic structures have been applied to dielectric materials as well. For a hybrid system that combines a single emitter coupled to a gold nanorod with a silicon nanodisk for redirecting the light, simulations predict a directivity of 8.5.[97] Even higher directivity of 40 (16 dB) was simulated using a photonic nanojet with a hybrid antenna consisting of a dielectric sphere and a plasmonic antenna.[98] Quantum dots (QDs) in the feed gap of a hafnium oxide nanoantenna showed partial directivity of 18 (12.5 dB).[99] In a hybrid system inspired by the Yagi-Uda antenna design, consisting of a gold bow-tie nanoantenna and three silicon nanorods, a directivity up to 49.2 was estimated based on a combination of experiments and simulations.[100] In previous work we have reported on a method to create directional emission from gallium arsenide (GaAs) nanowires with dielectric nanostructured microlenses designed with an evolutionary algorithm (EA).[65] This led to a record directivity from all-dielectric nanostructured microlenses of 22. The given examples of theoretical and experimental work on directivity above are summarized in Table 1. Many different metrics are used to assess directivity, caused by limited experimental access to the full directivity, which complicates comparison among different works. For example, many works use beaming half angle instead of directivity, which then ignores all power outside of the primary emission peak. Nevertheless, we have selected several relevant examples in Table 1, including metasurfaces used to direct light from LEDs[93] as well as parabolic light directors[101] and elliptical microlenses.[102] Directivity is typically measured with Fourier microscopy, which provides the angular emission pattern only within the numerical aperture (NA) of the objective. Either the relative enhancement or partial directivity within the collection cone of the objective is reported, which strongly depends on the NA. Alternatively, the total directivity is obtained from combining measurements and simulations.

	Full directivity	Partial directiviy (NA)	Beaming half-angle	FWHM	Lens (largest dimension)
Dielectric sphere (sim only)[46]	7.5				907 nm
Hybrid gold nanorod/ silicon nanodisk (sim only)[97]	8.5				620 nm
Sphere in nitrogen vacancy centers (sim only)[96]	11				380 nm
Photonic nanojet with hybrid antenna (sim only)[98]	40				20 μm
Hafnium oxide nanoantenna[99]		18 (1.49)		9°	3 μm
Hybrid Yagi-Uda nanoantenna[100]	49.2	44.3 (1.4)	4.6° / 27.3°		728 nm
InGaN/GaN quantum -well metasurfaces[93]			7°		3 μm
Parabolic light directors[101]			5.6°		22 μm
Elliptical microlenses[102]			1°		16.3 μm
Nanolens from EA (our previous work)[65]	22	18.9 (0.9)	3.5°		6 μm
Nanolens from EA (current work)	61	12.9 (0.42)	2.6°	5.6°	7 μm

Table 3.1: Overview of theoretical and experimental work on directional emission from (partly) dielectric nanostructures

The directivity obtained in our previous work was also limited by experimental constraints, causing the obtained directivity to be five times lower than the value predicted by finite difference time domain (FDTD) simulations. Limited by the NA of our objective, the directivity was determined by extrapolating outside the cone of the objective, and by relying on simulation results for the emission into the substrate. The randomly dropcast nanowires limited the lens alignment precision and provided extended emitters, both reducing performance compared to an ideal point source at the lens center.

Here we show a new approach for the fabrication and characterization that has led to a three-fold improvement in directivity. The enhancement relies on direct electron beam patterning of quantum dot emitter arrays, which both simplifies lens alignment and provides more localized sources. The more reproducible alignment also allowed for nanoscale lens corrections in both shape and size to play a role in improved directivity, partially overcoming previous limitations. Additionally, we have developed a new technique for measuring the complete directivity, which combines a Fourier microscope with an integrating sphere. figure 3.1 schematically shows the three parts of this work, which will be discussed in more detail in the following sections: the theoretical lens design with the EA, the fabrication process and the optical directivity measurements.

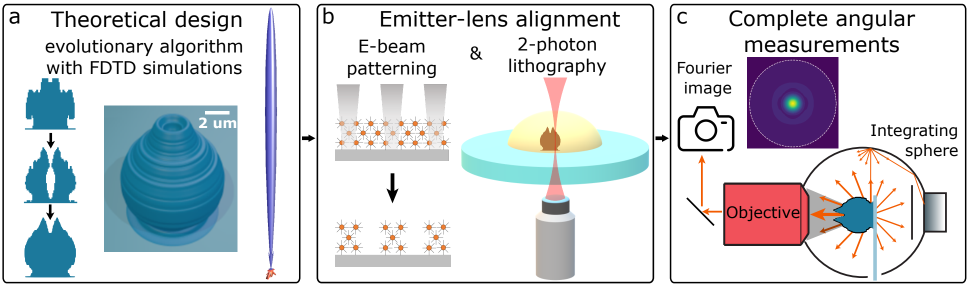

Figure 3.1: Schematic representation of the process towards highly directional emission. The first step (a) is the design of a 3D structure that gives directional emission from an emitter at the center. With an evolutionary algorithm, a 2D matrix that describes the presence of material is optimized (left). By rotating around the central axis a circularly symmetric 3D structure is obtained (center) for which the emission pattern is calculated (right). Fabrication of lenses on top of emitters consists of first patterning the emitters with direct electron-beam lithography (b, left). Upon exposure to an electron beam, the ligands in a film of CdSe-based QDs cross-link. Subsequently, unexposed parts are washed off and localized clusters remain. Next, 3D structures are fabricated from a transparent photoresist with 2-photon lithography (b, right). Finally, the complete angular directivity is measured by combining Fourier microscopy with an integrating sphere (c).

3.2 RESULTS AND DISCUSSION

3.2.1 EVOLUTIONARY ALGORITHM

Although the design of nanophotonic components in some cases can be guided by analogues developed for longer wavelengths, the high material dispersion of emitter materials in the visible, combined with the interplay between interference, refraction and diffraction effects can complicate their efficient design. Inverse design avoids this issue, allowing simulations of a component response to directly inform the creation of new designs. Broadly, two categories of such design processes exist: gradient-based techniques, and gradient-free techniques.[103, 104, 105] While gradient-based approaches generally offer more computationally efficient solutions, they are inherently local optimization processes, and can suffer in performance when many local optima are present.[106] Evolutionary algorithms offer a conceptually simple approach to gradient-free optimization, relying on the combination of features from previous well-performing structures to iteratively improve performance. The design here utilizes the same evolutionary process as described previously[65] to create a new directive nanolens optimized for our specific source geometry and emission frequency. In this case, we optimized for broadband and unpolarized absorption in a 100x100x50nm volume, in the wavelength range of 470 to 570 nm. This leads to relatively broadband directivity compared to resonant optics (figure 3.6), which tend to work only over a very narrow bandwidth. At the same time, the EA still allows for optimization over a specific wavelength range, contrary to conventional macroscopic lenses, which typically act similarly over the full optical spectrum.

The as-optimized lens shows a peak in directivity at 570 nm emission. For optimal performance, the maximum directivity can be shifted to the emission wavelength of the emitter of choice by scaling the lens size according to the wavelength. This can be done over a range of tens to hundreds of nanometers, as long as the dispersion of the material does not change significantly in this range. By increasing the size by 8%, the optimum was shifted to the emission wavelength in our experiments of 620 nm, resulting in a theoretical directivity of 160. The final lens geometry and 3D emission profile calculated for an orientation averaged dipole are shown in figure 3.1a and the corresponding theoretical Fourier image is shown in figure 3.1c. To prove the wavelength scalability, also lenses scaled for 520 nm and 700 nm emission were investigated, giving a directivity of 152 and 146 respectively. The small variations in directivity for the different wavelengths are within the accuracy of the simulations caused by finite meshing.

3.2.2 FABRICATION AND MEASUREMENT TECHNIQUES

An important aspect for optimizing the performance is the position and spatial extent of the emitters with respect to the lens. The lens performs best for a point source at the center of the lens, thus emitters should be fabricated that most closely resemble this. In earlier work, misalignment and large emitter size were the major causes for a reduction in performance.[65] For this work, we decided to use cadmium selenide/cadmium sulfide/zinc sulfide (CdSe/CdS/ZnS) QDs, since they are efficient and stable emitters. With a recently developed method, these QDs can be patterned in any design of choice with direct electron-beam (e-beam) lithography,[107] shown schematically on the left of figure 3.1b and experimentally in figure 3.2a. A spin coated film of QDs is locally exposed to an electron beam, which causes cross linking of the oleate ligands and makes the QDs insoluble. Subsequently the sample is developed by redispersing the unexposed QDs in tetrahydrofuran, such that only the exposed QDs remain on the indium-tin-oxide (ITO) coated substrate. This allowed us to make a square array of CdSe-based QD clusters of 200nm in diameter and 50 nm in height(figure 3.8), spaced 20 μm apart, and we included alignment markers for placing the lenses, as shown in figure 3.2a.

The nanolens is fabricated from transparent photoresist, through 2-photon lithography.[108] In the fabrication process the sample is exposed to high intensity infrared laser illumination and different chemicals. To shield the QDs from these harsh conditions, two protection layers are applied. First, 15 nm of alumina is evaporated on the sample to protect the QDs from chemicals and to bind the clusters more strongly on the substrate. Subsequently, a 120 nm film of transparent SU-8 photoresist is spin coated on the sample.

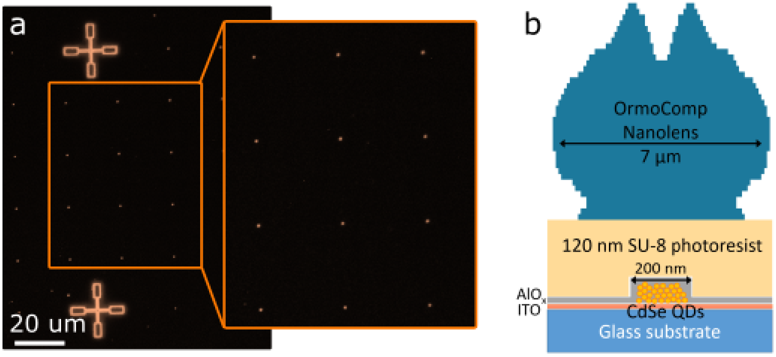

Figure 3.2: (a) Dark field optical microscope image of the patterned CdSe-based QDs. The crosses act as alignment markers for accurately writing the lenses on top of the small clusters. (b) Schematic of the full sample configuration. The Indium Tin Oxide (ITO) layer provides conductivity required for e-beam patterning. The alumina (AlO$_x$) and SU-8 photoresist act as protection layers against the harsh conditions of the 2-photon lithography process for making the nanolens. Dimensions and thicknesses are not to scale.

This layer acts as a spacer layer, such that the QDs are not directly in the focus of the laser during the lithography process.[65] The complete configuration of the sample, with all layers and materials present, is shown in figure 3.2b.

Directivity is defined as the maximum intensity (p_{max}) divided by the average intensity in all directions (p_{avg}), i.e. the total emission (P_{tot}) into the 4π solid angle of a sphere divided by 4π:[80]

$$D = \frac{p_{max}}{p_{avg}} = \frac{4\pi p_{max}}{P_{tot}}, \tag{3.1}$$

The conventional way to measure directivity is with a Fourier microscope. In these measurements, only light emitted into the cone of the objective is detected, from which the partial directivity within the numerical aperture (NA) of the objective can be determined. For air objectives (oil immersion would alter the performance of the lens), which have a maximum NA of ~ 0.95, a maximum 69% of the forward hemisphere is collected, and none of the light emitted in the backward direction. Even with two perfect objectives (one on each side of the substrate), the substantial fraction of light that is waveguided in the substrate and either scattered out or emitted at the edges will be lost. Previous works on directivity only report the partial directivity[99] or rely partly on simulations for determining the full directivity.[100] An alternative to Fourier imaging for wide angle measurements is to place a detector on a rotation stage and scan in a circle at a fixed angle.[109] However, using such an approach for complete directivity would be very time consuming and complex as it would require very accurate scanning over the full three-dimensional sphere. For individual nano and microstructured lenses the signal is too low for such an approach to be feasible. Due to the difficulties above, experimental measurements of the full directivity are absent from the literature.

We built a setup with which we can obtain the full directivity of an individual nanostructured microlens coupled to a 200 nm emitter patch in a single measurement. To achieve this, we combined a Fourier microscope with an integrating sphere (IS), shown schematically in figure 3.3a. The integrating sphere gives the missing piece of information in the Fourier measurement, by collecting all the light that was emitted outside the cone of the objective. This light is scattered around in the IS and measured with a photodetector on the back, while at the same time an image is taken with a CCD camera in the Fourier plane of the microscope. The Fourier image provides p_{max} and by combining the Fourier and IS signals P_{tot} can be determined. Combining these two signals demands careful calibration of the collection efficiencies; a detailed description of the required reference measurements and the full calculation can be found in the Supporting Information. With proper calibration, our integrating sphere Fourier microscopy method can therefore provide an accurate full directivity value for any structure with an emission peak that falls within the NA of the objective lens.

The sample is mounted on a piezo stage, that allows us to scan the focused excitation spot through the structure in three dimensions and find the position of highest directivity. Here we benefit from the fact that the directivity can be determined in a single measurement, allowing us to take detailed maps over the lenses. After finding the optimal position, repeated measurements were taken on this fixed location, to determine the noise on the signals and get accurate directivity values. With an additional lens in front of the objective, we can create full field laser illumination to excite multiple lenses. We can find the structures in a real space image (figure 3.3b) and by inserting the Fourier lens, Fourier images can be taken for either full field illumination (figure 3.3c) or focused excitation (during the measurements). Note that for combining the Fourier microscope with an integrating sphere, an objective with a long working distance of 17 mm has to be used, which leads to a relatively low NA of 0.42. As a consequence, our measured partial directivities might appear relatively low. As long as the peak of maximum intensity lies within the cone of the objective, this low NA is not a problem for the determination of full directivity.

With nanoscale corrections we optimized the fabrication of the nanolenses, to make them closely resemble the designed structure. We optimized two aspects separately: the size and the shape. Due to slight shrinking of the photoresist in the development process, structures made with 2-photon lithography typically have to be written with slightly larger coordinates in order to end up with the correct size. The amount of shrinking depends on the laser power used for writing (see figure 3.9), and the density of points with which the structure is written. Lenses with different size scaling were fabricated and measured with a scanning electron microscope (SEM). The diameter of the lens is easily measured from the top view. The height of the lens was checked by cutting a cross section through a lens with focused ion beam (FIB) milling. To be less sensitive to the exact location of the FIB cutting plane, we fabricated elongated lenses with a fixed cross section over several micrometers, which is why the lenses shown in figure 3.4 are not circularly symmetric.

Higher laser power typically gives sharper features, but when the intensity is too high, this results in small explosions in the photoresist (figure 3.10).[110,111] Therefore we fine-tuned the exact shape by comparing the FIB cross sections with the desired design. figure 3.4a shows the first step, in which the lens was written based on the original binary matrix from the EA together with the desired cross section in orange. Subsequently, pixels corresponding to regions with too much material (marked red and orange in figure 3.4b) are removed from the writing coordinates. This first optimization resulted in a close

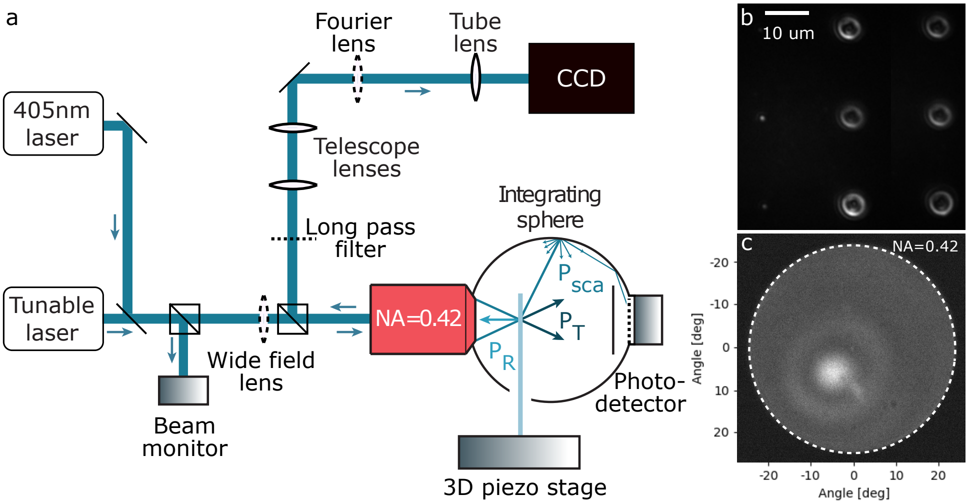

Figure 3.3: (a)Schematic representation of the combined integrating sphere and Fourier microscope for complete angular measurement of directivity. By moving out the Fourier lens, the sample is seen in real space to find the structures. Measurements are taken in the Fourier configuration with 450 nm long pass filters to remove the 405 nm laser excitation, where the CCD gives the angular emission pattern in the cone of the objective, while the integrating sphere photodetector collects light emitted in all other directions. The tunable laser is used to determine the collection efficiencies at the emission wavelength and the beam monitor tracks fluctuations in excitation intensity. With the sample mounted on a piezo stage the exact position of maximum directivity can be found. (b) Real space image of bare clusters (left column) and lenses (right two columns) in wide field laser illumination; (c) Fourier image of lenses in wide field laser illumination.

resemblance between the observed cross section and the desired shape(figure 3.4c). In the second optimization the two red pixels in the top are added again to better match the shape of the top of the lens.

3.2.3 COMPLETE ANGULAR DIRECTIVITY MEASUREMENTS

With the techniques and optimizations described above, we were able to accurately fabricate nanolenses on top of arrays of CdSe-based QD clusters, as shown in figure 3.5a. The first directivity measurements were performed on lenses from the original design, like the one in figure 3.4a. The writing coordinates were scaled by 102%, 106% and 110% to find the optimum size. These lenses all performed rather poorly, with a partial directivity, i.e. only in the NA of the objective (D_{NA}), between 3 and 4 and a total directivity ($D_{4\pi}$) between 8 and 26 (figure 3.5d left and table 3.2). The first optimization again consisted of lenses in the three different sizes. The adjustment in shape turned out to be an essential step: a partial directivity as high as D_{NA}=10.9 was observed, corresponding to a total directivity of $D_{4\pi}$=41. All five lenses of scale 102% performed similar, see figure 3.5d middle and table 3.3 for all results. The last optimization consisted of a detailed size tuning and three small variations in the design. The sizes were varied between 98% and 106% in steps of 2%. The three designs were the design of optimization 1 (thus red and orange pixels in figure 3.4b removed), the design of optimization 2, i.e. only the orange pixels removed, and this same

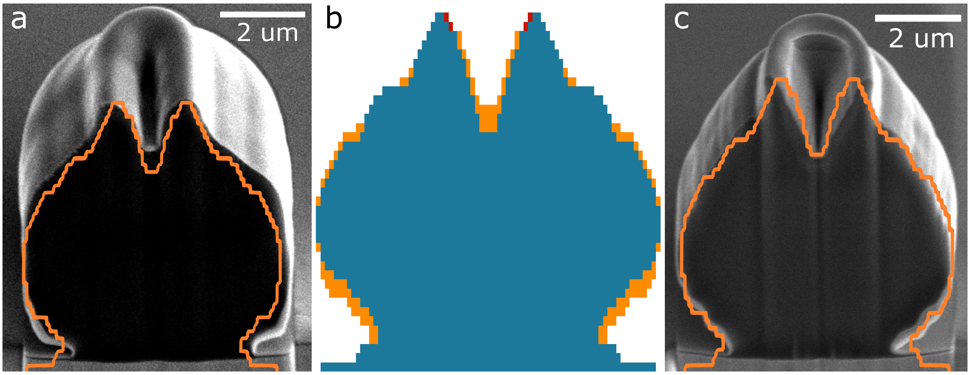

Figure 3.4: Optimizing the lens shape. (a) Lens based on the original binary matrix, with too much material at certain locations compared to the desired shape (orange line); (b) The original binary matrix (all pixels), the pixels that were removed in the first optimization (red and orange), resulting in the lens in (c) and the pixels that were added again in the last optimization (red).

design, but elongated in height by 2%, because SEM analysis showed that the previous set of lenses was slightly too flat.

In this second optimization we found the highest partial directivity of D_{NA}=12.9 and a beaming half angle (σ) of 2.6°, of which the Fourier image is shown in figure 3.5b (for refrence of bare emitters without a lens on top, see figure 3.11). Repeated measurements of the same position were taken to accurately determine the total directivity and the uncertainty on this value, resulting in an average D_{NA}=12.1±0.1 and $D_{4\pi}$=61±3 over ten measurements. Repeated measurement over a longer time show a decrease in directivity, as plotted in figure 3.5c lower panel. We attribute this to degradation of the QDs, since also the signal intensity of both detectors decreases over time (figure 3.12) and degradation was also observed for emitters without a lens on top (figure 3.13). On the other four best performing lenses, 18 repeated measurements were taken, resulting in D_{NA} and $D_{4\pi}$ values as plotted on the right of figure 3.5d. More measurements for determining the accuracy and the effect of excitation power on mutliple lenses can be found in figure 3.15. Results of the 15 best performing lenses, out of the 48 lenses that were fabricated and measured, are summarized in table 3.4. From this analysis we can conclude that we have fabricated at least fifteen lenses with $D_{4\pi}$>45, with probably even better performance before degradation. All lenses with scaling of 106% performed similar and no trend could be observed between the different designs in the final optimization step. Also each of the other size scales had one or two high performing lenses.

As a proof of concept of the wavelength scalability, we fabricated lenses scaled in size for two different wavelengths: 520 nm and 700nm, the emission wavelengths of cesium lead bromide ($CsPbBr_3$) perovskite nanocrystals and methyl-ammonium lead halide ($MAPbBr_{0.2}I_{0.8}$) thin film, respectively. These samples consisted of a continuous film of emitters instead of localized clusters and only the partial directivity D_{NA} could be determined. Even with these limitations the results look promising: both systems reach D_{NA}>11; Fourier images are shown in figure 3.16. This result is surprisingly good for

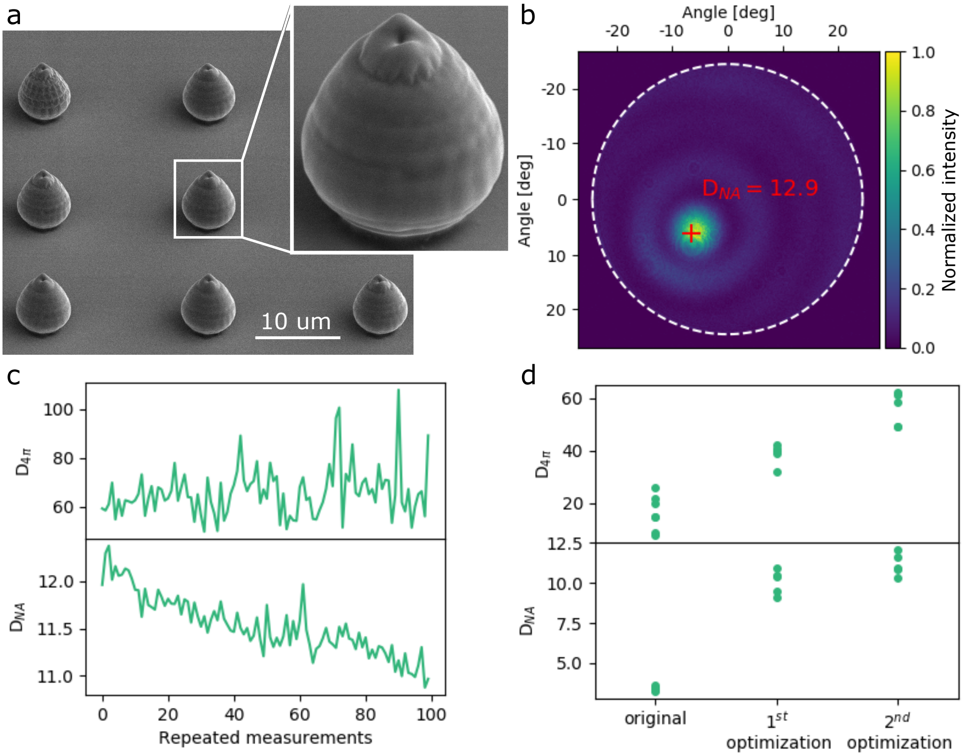

Figure 3.5: Results of the complete process. (a) nanolenses accurately written on an array of CdSe-based QDs clusters; (b) Fourier image of the lens with highest measured directivity, of D_{NA}=12.9; (c) Repeated measurements on a fixed location show degradation of the lens and/or emitter, causing a lowering in D_{NA} (lower panel) and an increase in the noise on $D_{4\pi}$ (top panel); (d) Results of the best performing lenses of each of the optimization steps.

lenses on a continuous film, where no localized emitters were created. However, these halide perovskites are known for their photobrightening.[112] We hypothesize that focusing of the excitation laser by the lens causes local photobrightening in the film, resulting in more localized emission. We have performed optical simulations showing that the FWHM of the excitation spot size created by the nanostructured microlens is approximately 200 nm (figure 3.14)and would lead to a directivity of 200, consistent with the patch size and theoretical directivity of the localized CdSe emitters. This very interesting observation requires further investigation in future work and may enable a self-aligned mechanism for greatly improved performance.

From the large increase in directivity by adjusting the design, we can conclude that the directivity is sensitive to the exact shape of the lens structure. The small variations in the final optimization did not show any significant trend, indicating that lens to lens variation due to fabrication inaccuracy is larger than the designed adjustments in this final step. The dependence of the directivity on the exact shape matches well with results from simulations, where we also noted a large sensitivity to the shape of the structures. Since it is impossible to have perfect agreement between the simulated and the fabricated structures, combining experimental results with simulations will be inaccurate. This shows the importance of our fully experimental measurement, which allows us to investigate the actual fabricated structures without relying partially on simulations. For a cluster of emitters with a diameter of 200 nm, simulations predict a total directivity of $D_{4\pi,theory}$=131 and $D_{NA,theory}$=35. Although our measured $D_{NA,experiment}$=12 is roughly 3 times lower compared to theoretical performance, our measured $D_{4\pi,experiment}$=61 is almost half the theoretical value and thus better than what would be predicted by extrapolating $D_{NA,experiment}$.

The fact that the measured directivity is still significantly lower than the theoretical directivity, we assign to fabrication errors, primarily alignment errors. Simulations show that the directivity is decreased by 50% if the emitter is misaligned by only 130nm with respect to the center of the lens (figure 3.18a). The tilting of the emission peak from the normal is also consistent with a misalignment of approximately 200 nm (figure 3.18). Also small size variations might still play a role, as we predict a drop in directivity of 20% for each 3% offset in size (figure 3.18b). In our last optimization step, the lenses with size 106% performed best, but each of the other sizes also had a positive outlier. This probably corresponds to occasionally very well aligned lenses, such that they perform well despite their slight size offset. The different optimal size found in the last two optimization steps (102% vs 106%) we ascribe to variation in sample absorbance. Since the resulting size of structures made by 2-photon lithography strongly depends on the laser power, a slightly higher absorption in the sample requires larger writing settings in order to obtain the same size.

3.3 CONCLUSION

With accurate nanoscale optimization of the fabrication technique, we have achieved a record in directivity from all-dielectric nanolenses, three times higher than the previous reported value. We have fully experimentally determined a maximum total directivity of $D_{4\pi}$=61±3, corresponding to a partial directivity within the cone of the objective of D_{NA}=12.1±0.1. At low laser power excitation, at which only D_{NA} could be accurately determined, partial directivity values up to 12.9±0.1 were observed. This shows that with accurate fabrication techniques, highly directional emission from CdSe-based QDs can be obtained with all-dielectric nanostructures. An essential step to achieve this was the patterning of emitters with direct e-beam lithography into an ordered array of small clusters with alignment markers, such that an array of lenses could be accurately fabricated on top of the emitters. The combination of an integrating sphere and a Fourier microscope allowed for complete angular measurement of the directivity, which was 35% higher than what would have been predicted by a combination of Fourier microscopy and simulations. With the knowledge obtained here, we can take further steps in directional emission with dielectric nanostructures. This work was focused on single nanolenses. The capability of creating patterned emitters opens up possibilities for future work in which one could make use of array effects on top of the individual nanolens effects or design periodic structures that provide directivity.

3.4 MATERIALS & METHODS

3.4.1 FABRICATION

All samples were fabricated on ITO coated glass cover slips of thickness 170 μm with a resistance of 8-12 Ohms per square from Diamond Coatings. Substrates were cleaned before spin coating the quantum dot layer by 15 mins of sonication in demineralized water, acetone and isopropanol, followed by 15 min oxygen plasma treatment. CdSe-based QDs were fabricated according to an adjusted protocol from[113, 114, 115], described in detail in the Supporting Information. QDs dispersed in toluene were spin coated at 500 rpm for 90 s followed by 30 s at 1000 rpm. These films were exposed in a Raith Voyager commercial e-beam lithography system with an accelerating voltage of 50 kV, MC40 or MC60 column mode with 0.94±0.02 nA or 2.20±0.05 nA beam current respectively. Samples were developed in tetrahydrofuran for 30 s, followed by a 5 sec rinse in anhydrous n-octane, before drying with nitrogen. The alumina layer was applied with an electron beam physical vapor deposition system from Polyteknik. A source of Al_2O_3 was used with additional oxygen inflow to evaporate 15nm of alumina (AlO_x) of unknown composition at a rate of 0.2 nm/s. The spacer layer of transparent SU-8 photoresist was made by spin coating 120μL of 1:10 diluted SU-8:cyclopentanone at 4000 RPM for 60 s. Subsequently the samples were dried on a hot plate at 100° C for 60 s, exposed with a hand held UV lamp at 365 nm for 10 min and a further hardened with final hard bake on the hot plate of again 100° C for 60 sec. The lenses are fabricated with 2-photon lithography (Photonic Pro, Nanoscribe GmbH) from undiluted OrmoComp photoresist (micro resist technology GmbH), which has low fluorescence and high transparency and stability.[116] The alignment markers were used for positioning the lenses. In case the actual clusters of emitters could be seen in the Nanoscribe microscope (ca 30% of the time), small manual adjustments were made to the exact position of the lens. The structures are developed with mr-Dev 600 (micro resist technology GmbH) for 25 min, followed by 5 min in isopropanol. During the rinsing in isopropanol, the structures are exposed to 365nm UV light to make the lenses more robust.[117] For characterization with scanning electron microscope (SEM), lenses were sputter-coated with 5nm chrome and 15 nm gold conductive layers. Focussed ion beam milling for making cross cuts and SEM imaging was done on a FEI Helios Nanolab 600.

3.4.2 MEASUREMENT SETUP

The combined Fourier microscope and integrating sphere setup was created by adding a Fourier microscope to an existing integrating sphere setup, which has been described before.[118] The Fourier microscope was added by placing a pellicle beam splitter (BP145B1 Thorlabs GmbH) right behind the objective. Excitation was done with a 405nm laser (S1FC405 Thorlabs GmbH). The light goes via a long pass filter at 450 nm, a set of telescopic lenses, a Fourier lens that can be taken out for real-space imaging and a tube lens to the CCD camera (Retiga Lumo model 01-RET-LUMO-R-M-16-C, Teledyne Photometrics). Fourier images were taken at 200 and 500 ms integration time, with 2x2 pixel binning.

3.5 Supporting information

3.5.1 Lens optimization

The nanophotonic microlens was optimized for maximizing broadband absorption. This results also in broadband directivity, with some variations with wavelength. The maximum directivity is found for 570 nm emission from the center of the lens.

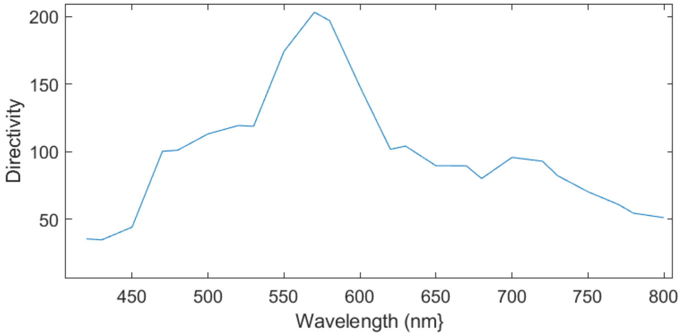

Figure 3.6: The simulated directivity as a function of emission wavelength for the as-optimized lens from the evolutionary algorithm.

3.5.2 Reference measurements and calculation of full directivity

The Fourier microscope was calibrated using a 4 μm square grid. With the tunable laser diffraction patterns in the range of 400 to 800 nm wavelength were collected. An example is shown in figure 3.7 for 550 nm. The Fourier image of the diffraction pattern is summed in vertical and horizontal direction, to obtain the blue graphs in figure 3.7 c and d, respectively. The peaks are fitted with a Gaussian distribution to determine the peak position. From the diffraction equation and the known pixel size of the CCD detector the relation between position in the Fourier image and angle is obtained.

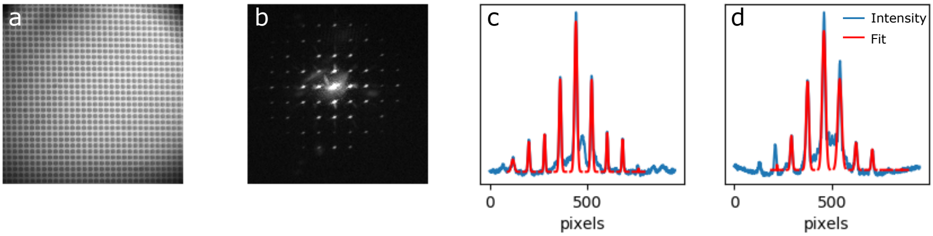

Figure 3.7: a) Real space image of the 4 μm square grid taken in the setup; b) Fourier image of the diffraction pattern obtained by exciting the grid with a parallel laser beam at 550 nm. c) and d) vertical and horizontal summed pixel intensities and Gaussian fits to the peaks.

The detection efficiencies of the Fourier microscope and the IS photodetector were determined using a tunable laser at the emission wavelength (600-650nm) of the CdSe-based QDs. With a calibrated photodetector the number of photons coming from the tunable laser and reaching the location of the sample were determined. The collection efficiency of the Fourier microscope was determined by placing a mirror with a known reflectivity of 95% at the sample position and integrating the counts on the resulting Fourier image, to get the counts/photon of the Fourier microscope. The collection efficiency of the IS photodetector was determined with the sample inside the integrating sphere but focusing the laser just next to the sample. This way reabsorption by the sample of light scattered around in the IS is accounted for in the resulting current/photon value. By weighting the obtained values over the wavelength range of 600-650 nm by the emission spectrum of the CdSe QDs, two single values are obtained, IS_{miss} and F_{mirror}. Since both correspond to the same number of photons with the same spectrum coming from the location of the sample, they can be used to convert the integrating sphere signal for the sample measurements to the same units of the Fourier image, such that they can be added together.

$$IS_{sample,converted} = \frac{IS_{sample}}{IS_{miss}} F_{mirror} \tag{3.2}$$

Which with we can calculate the total amount of emission

$$P_{tot} = IS_{sample,converted} + F_{sample} \tag{3.3}$$

To account for excitation laser light passing through the long pass filters, and for any fluorescence coming from materials other than the QDs, measurements were taken on a reference sample that contains all layers and materials, including the nanolenses, but without QDs. The signals this gave on the IS photodetector and the CCD camera were subtracted from the sample measurements before calculating the total emission. By subtracting the Fourier image of the reference sample from the Fourier image of the real sample (both taken at the exact same settings), also dark current and read-out noise are removed from the CCD signal.

3.5.3 FABRICATION

SYNTHESIS OF CdSe/CdS/ZnS QDs

Materials: CdO (99.99%), Cd(II)-acetate (99.995%), Zn(II)-acetate (99.99%) Octadecene (ODE, 90%), Oleylamine (OLAM, 99.8%), Oleic acid (OA, 90%), Butanol (BuOH, Anhydrous, 99.8%), Methanol (MeOH, Anhydrous, 99.8%), Hexane (99.8%, Anhydrous), Octadecylphosphonic acid (ODPA, 97%), Trioctyl phosphineoxide (TOPO, technical grade, 90%), Trioctylphosphine (TOP, 97%), 1-Octanethiol (>98.5%) and Selenium powder (Se, 99.99%) were all bought from Sigma-Aldrich and used as received unless specifically mentioned. **Synthesis of CdSe core nanocrystals (NCs)**. The CdSe core nanocrystals were synthesized according to a method by Chen et al.[114] In a 50 mL three-necked flask, 60 mg of CdO, 280 mg octadecylphosphonic acid (ODPA), 3 g trioctylphosphineoxide (TOPO) and a magnetic stirring bar were added. This mixture of powders was heated up under vacuum to 150°C, where the mixture melts. The mixture was slowly stirred (it prevents the CdO from creeping up the inside of the flask) and degassed at this temperature for one hour. The mixture was heated up to 320°C, where the liquid turned into a clear and colorless solution. Note that depending on the batch of QDs the time it took for the solution to become clear varied from 20 minutes to 4 hours; this has likely something to do with the impurities in one of the chemicals. 1 mL of trioctylphosphine (TOP) was added to the solution, and the temperature was raised to 380°C, at which point 0.5 mL of a Se-precursor solution (60mg Se in 0.5mL TOP) was swiftly injected. After a specific growth time the reaction mixture was cooled with an air-gun to room temperature. For the CdSe cores in this work, we used a growth time of ±25 seconds. The crude product is washed once by addition of a 1:1 volume ratio of methyl acetate, followed by centrifugation at 3000 RPM, and redispersion into hexane. Solution is then filtered through several milipore filters (the polymerized ligands clog the filters easily) with a pore diameter of 0.2 μm. The filtered solution is washed and centrifuged again as described above, redispersed in hexane and the resulting sample is stored in a nitrogen purged glovebox for further use.

Synthesis of Cd-oleate and Zn-oleate for CdS and ZnS shell growth. For the Cd-oleate synthesis, 1.32 g of Cd-(acetate)$_2$ was dissolved in 52.4 g ODE and 7.4 g OA. The mixture was heated up under vacuum to 120°C and left there for three hours. Afterwards, the reaction was cooled down to room temperature and the Cd-oleate solution was stored in a nitrogen purged glovebox for further use. The Zn-oleate was made in a similar fashion. Zn(II)-(acetate)$_2$ was mixed with 1 g of OA, 1.6 mL ODE and 1.6 mL of OLAM. The oleylamine serves as a stabilizing ligand for the Zn-oleate, since this has the tendency to solidify out of solution at room temperature otherwise. The mixture was heated up in a 20 mL vial inside a nitrogen purged glovebox to 130°C and stored there for further use. Note that the Zn-oleate solution is extremely viscous and should be handled with care when placed into a syringe.

Shell growth of CdS and ZnS. The shellgrowth of CdSe QDs into core-shell-shell CdSe/CdS/ZnS nanocrystals was done according to an adapted method by Chen et al.,[114] Boldt et al.[115] and Hanafi et al.[113] For the CdS shell growth, 50 nmol CdSe cores, 3.0 mL octadecene (ODE) and NO oleylamine (OLAM, after recent work by Hanafi et al.[113]) were added to a 100 mL three-necked flask and degassed for one hour at room-temperature (21°C) and for 20 hours at 120°C to completely remove hexane, oxygen and water. After that, the reaction solution was heated up to 310°C under nitrogen flow and magnetic stirring. During the heating, when the temperature reached 240°C, a desired amount of Cd-oleate (diluted in ODE) and 1-octanethiol (diluted in 8 mL ODE) were injected dropwise into the growth solution at a rate of half a CdS monolayer per hour using a syringe pump. We define one CdS monolayer as one full layer of Cd and one full layer of S on the NC surface (i.e. half a unit cell). After the addition of the CdS shell-precursors was finished, but before the growth of the ZnS shell, the core-shell QDs containing solution was degassed at a pressure of 0.5 mbar for one hour at 120°C. For the ZnS shell-growth, the sulfur precursor consisted again of 1-octanethiol diluted in ODE. The solution with freshly grown CdSe/CdS QDs was heated up to 280°C under nitrogen flow. When the solution reached 210°C, a desired amount of Zn-oleate and 1-octanethiol in 4 mL ODE (in two separate syringes) was injected at a rate of 2 mL/hour (roughly one monolayer of ZnS per hour). After addition of the precursors, the solution was cooled down to room temperature by removing the heat and with an air-gun. The solution was washed twice by addition of methanol:butanol (1:2), centrifugation at 3000 RPM for 10 minutes, and once with methylacetate followed by centrifugation at 3000 RPM. The precipitate was each time redispersed in hexane. Finally, the solution was filtered through milipore filters with a pore diameter of 0.2 μm and stored in a nitrogen purged glovebox for further use.

Using the above methods, we synthesized several batches of core-shell-shell CdSe/8CdS/2ZnS QDs.

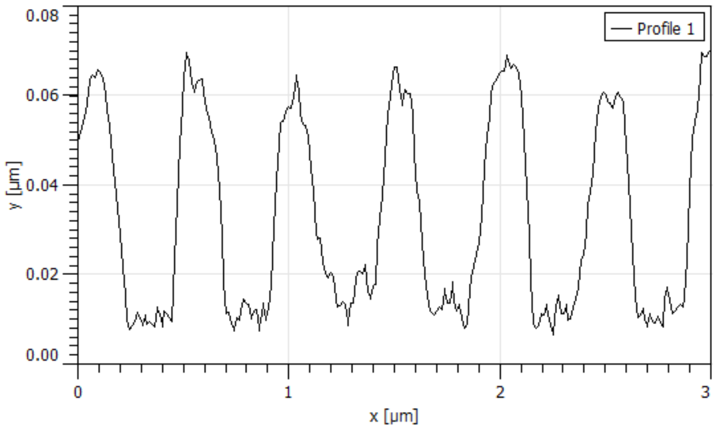

Figure 3.8: Atomic force microscope line scan over an array of CdSe QDs patterned with e-beam lithography, showing the height and width of the patches to be 50 nm and 200 nm respectively. For the actual experiments the patches were spaced further apart (20 μm).

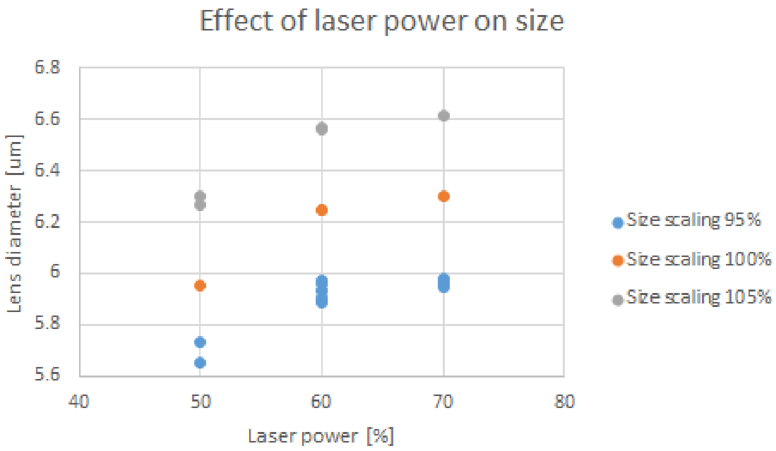

Figure 3.9: 2-photon lithography at higher laser power leads to larger structures. Lens diameters were determined from SEM images.

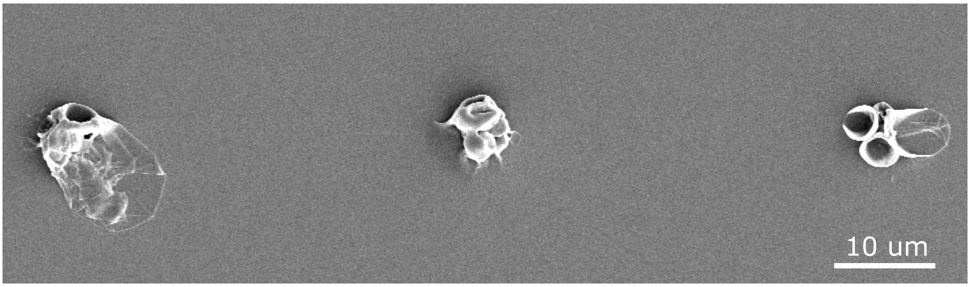

Figure 3.10: SEM image showing how 2-photon lithography at excessively high laser power leads to explosions in the photoresist.

3.5.4 DIRECTIVITY MEASUREMENTS

The integrating sphere signal used for determining $D_{4\pi}$ is quite low and close to the noise level. This causes some uncertainty in the calculated value of $D_{4\pi}$. To check the accuracy of our method, 18 repeated measurements were taken on the 5 best performing lenses at two different laser powers, first at low power (24μW) and then at high power (63μW). The results are shown in figure 3.15. At low power D_{NA} is consistently higher, but the uncertainty in $D_{4\pi}$ is rather large (variations up to 20%). At high power $D_{4\pi}$ can be accurately determined, but performance is already slightly degraded. The values for $D_{4\pi}$ obtained at low and high power are quite similar, confirming the validity of our results. The best result at high power was obtained for lens 5 with a D_{NA}=10.4±0.1 and $D_{4\pi}$=57±3.8.

Table 3.4 shows the measurement results of the 15 best performing lenses. It shows some very high values for $D_{4\pi}$. However, these are single shot measurements at low power, and thus the noise on these signals might be as large as ±20. Lenses marked with * have bean used for repeated measurements at both low and high laser power, from which the results are shown in figure 3.15. The average value for $D_{4\pi}$ for these 15 lenses is 55, with a root mean square standard deviation of 9. Given that they all have quite similar D_{NA}, and that repeated measurements showed that this typically corresponds to $D_{4\pi}$ >45 (after laser induced degradation), we estimate that all these lenses had an initial directivity $D_{4\pi}$ >45.

The reduction in directivity over repeated measurements, especially at high laser power, we attribute to photobleaching of the QDs, as can also be seen from the reduction in photoluminescence signals in figure 3.12. Especially the ones in the focusing hotspot of the lens will experience high laser power. Due to reciprocity, the QDs in the hotspot will have the highest directivity. If their contribution is reduced due to photobleaching, the directivity will go down.

	D_{NA}	$D_{4\pi}$
sc102_orig_lens1	3.5	9
sc102_orig_lens2	3.4	22
sc102_orig_lens3	3.2	8
sc102_orig_lens4	3.4	26
sc102_orig_lens5	3.4	15
sc106_orig_lens1	3.3	20
sc110_orig_lens1	3.6	15

Table 3.2: Results of first directivity measurement on lenses without adjusted design. Lens size was scaled by 102%, 106% and 110%.

	D_{NA}	$D_{4\pi}$
sc102_opt1_lens1	10.4	40
sc102_opt1_lens2	10.5	42
sc102_opt1_lens3	10.9	41
sc102_opt1_lens4	9.5	39
sc102_opt1_lens5	9.1	32

Table 3.3: Best performing lenses after the first iteration, adjusting the design.

	D_{NA}	$D_{4\pi}$	FWHM (°)	σ (°)
sc98_opt1_lens2*	12.4	68	6.6	3.1
sc98_opt2_lens2	12.5	48	6.5	2.8
sc98_opt2_h_lens2*	11.1	50	6.1	2.9
sc100_opt1_lens2	9.6	45	7.2	3.2
sc100_opt2_lens2	10.3	57	6.6	3.0
sc102_opt1_lens2	11.7	63	6.3	2.9
sc102_opt2_lens4	10.2	43	6.5	2.9
sc102_opt2_h_lens1	9.6	48	6.3	2.8
sc104_opt2_lens1	11.5	63	5.6	2.7
sc104_opt2_lens2	9.0	44	5.7	2.8
sc106_opt1_lens2	12.4	76	5.6	2.6
sc106_opt2_lens1	11.7	63	6.0	2.8
sc106_opt2_lens2*	12.7	39	5.7	2.6
sc106_opt2_h_lens1*	11.1	54	5.6	2.6
sc106_opt2_h_lens2*	12.1	65	5.7	2.6

Table 3.4: Best performing lenses after the second iteration, comparing three different designs: from optimization 1 (opt1), the second adjustment, adding two pixels again (opt2) and opt2_h with lenses 2% higher, and different scalings (sc##) Also the full width at half-maximum (FWHM) and the beaming half angle σ were calculated for these lenses for reference with other work. In total 48 lenses were fabricated and measured: four of each of the three design types for scaling 100%, 102% and 104%, and two of each type for scaling 98% and 106%.

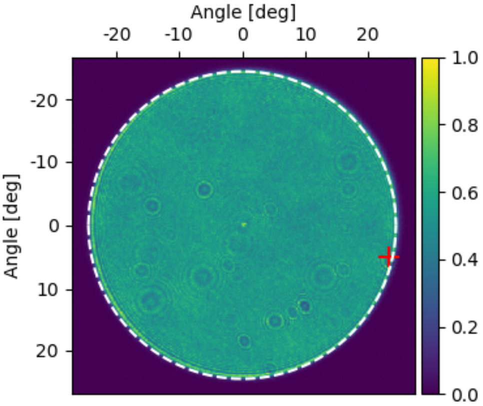

Figure 3.11: Fourier image of bare QDs without lenses on top, showing completely uniform emission. Small pixel to pixel variation causes a partial directivity of D_{NA}=1.8 and a total directivity $D_{4\pi}$=2.5.

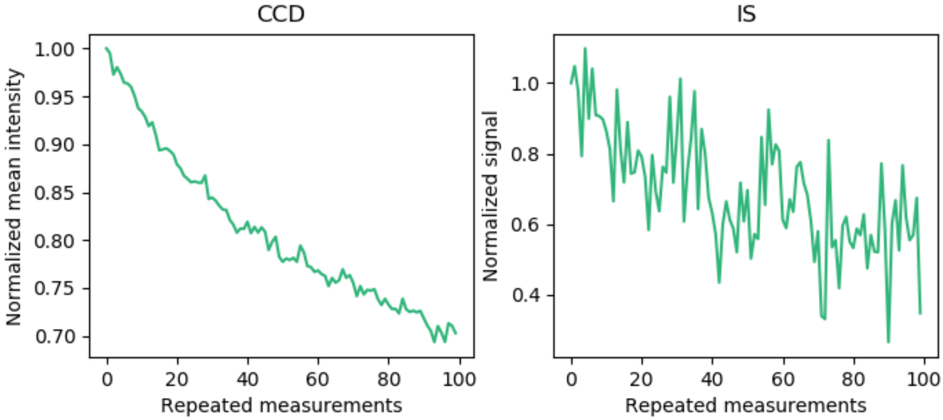

Figure 3.12: Decreasing signals over repeated measurement on the best performing lens. Since the signal also goes down for emitters without lens on top, we conclude that the emitters are degrading rather than the lens.

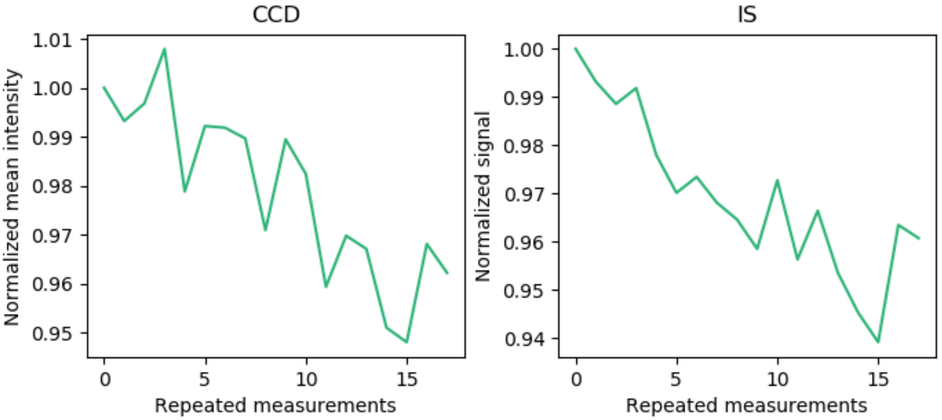

Figure 3.13: Decreasing signals over repeated measurement on emitters without lens on top.

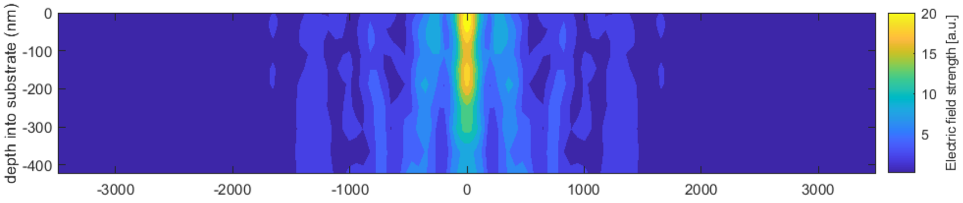

Figure 3.14: Simulated field intensity underneath the lens scaled for 700 nm emission, excited with a plane wave of 400 nm. This results in a hotspot with FWHM of 200 nm underneath the center of the lens.

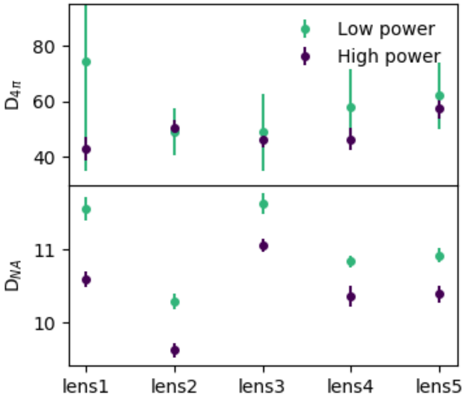

Figure 3.15: Measured directivities for the five best performing lenses of the second optimization, measured at low (24μW) and high(63μW) laser power.

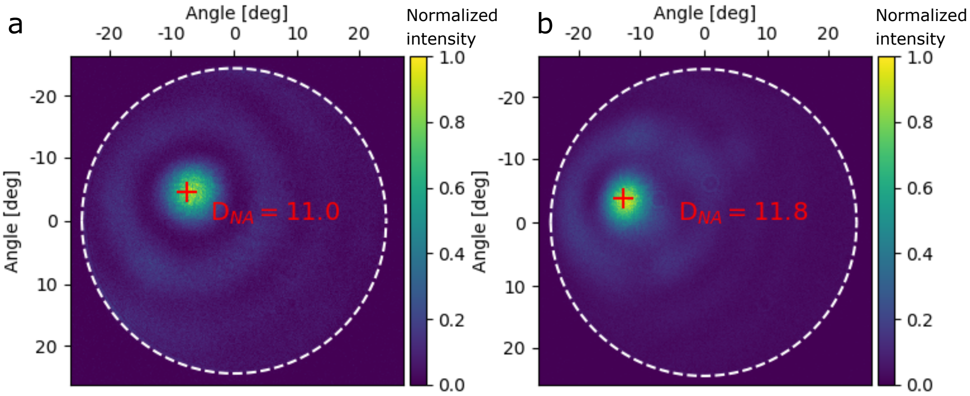

Figure 3.16: Fourier image of the emission pattern from lenses on top of (a) $CsPbBr_3$ nanocrystals, emitting at 520 nm and (b) $MAPbBr_{0.2}I_{0.8}$ thin film emitting at 700 nm.

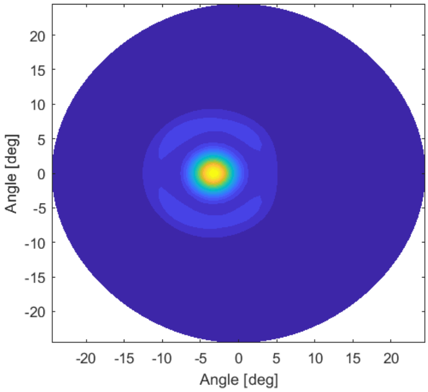

Figure 3.17: Simulated Fourier image of orientation averaged dipole emitter 200 nm off-center of the lens. This shows that misalignment of the lens with the emitter causes emission slightly away from normal direction.

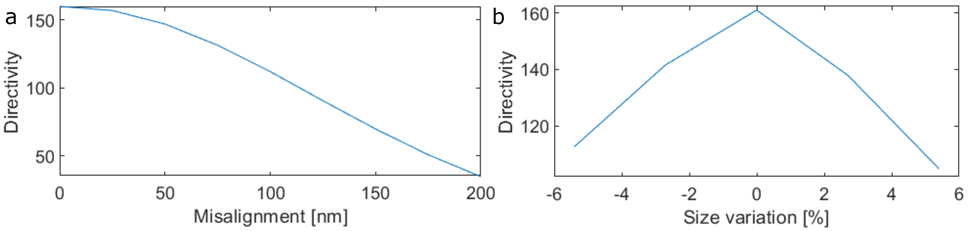

Figure 3.18: Simulations results on the effect of (a) lens alignment with respect to the emitter and (b) lens size on directivity.

4

PEROVSKITE PLASTICITY: EXPLOITING INSTABILITY FOR SELF-OPTIMIZED PERFORMANCE

Halide perovskites are the new wonder material of the optoelectronics community due to their outstanding photoluminescence quantum yield, tunable emission wavelength and simple solution or vapor-phase deposition.[119, 12, 14, 120, 121] *At the same time, their facile ion migration and transformation under optical, electrical and chemical stress are seen as a major limitation for device implementation.*[122, 123, 124, 125] *Mixed halide perovskites are particularly problematic since optical excitation can cause changes in the bandgap that are detrimental for solar cell and light-emitting diode efficiency and stability.*[126, 127, 128, 129, 130] *In this chapter, instead of preventing such changes,*[131] *we exploit photo-induced halide segregation in perovskites to enable responsive, reconfigurable and self-optimizing materials. We show how a mixed halide perovskite film can be trained to give highly directional light emission using a nanophotonic microlens: through a self-optimized process of halide photosegregation, the system mimics the training stimulus. Longer training leads to more highly directional emission, while the different halide migration kinetics in the light (fast training) and dark (slow forgetting) allow for material memory. This self-optimized material performs significantly better than lithographically aligned quantum dots,*[132] *because it eliminates lens-emitter misalignment and automatically corrects for lens aberrations. Our system shows a combination of mimicking, improving over time, and memory, which make it compatible with the basic requirements for learning,*[133, 134, 135] *and give the intriguing prospect of intelligent optoelectronic materials.*

4.1 INTRODUCTION

The instability of halide perovskites that results from their dynamic nature has been seen as a major limitation to implementing them in applications that require long-term stability, such as solar cells and light emitting diodes.[126, 127, 128, 129, 130] In contrast, the push towards intelligent materials has largely taken inspiration from natural and living systems, where instability (material turnover and regeneration) is essential for environmental adaptation, optimized properties and learning.[136, 137] By altering the response and regeneration timescale, nature can span from slowly optimizing and relatively stable materials to those that are much less stable but also respond more quickly. There are now synthetic analogues trying to span this continuum as well. For example the ability of bone to strengthen itself in response to mechanical forces has been artificially mimicked with composite materials that cross-link upon mechanical loading.[138] Neuromorphic computing lies on a faster time scale,[6] where self-learning optical neurosynaptic networks are being pursued to mimic brain plasticity, due to the broad bandwidth and high speed inherent to optical systems.[5]

The combination of rapid ion migration, sensitivity to many external stimuli, and outstanding optoelectronic properties displayed by halide perovskites make them the ideal platform for the next generation of reconfigurable, responsive, programmable, and intelligent materials.[139] In this work, we exploit a photoinstability (light-induced halide segregation) to train a mixed halide perovskite thin film to display user-defined optical properties. Our case study consists of a mixed halide perovskite thin film that is trained to give highly directional light emission using a nanophotonic microlens and exploiting the rules of reciprocity. It exhibits many of the most attractive behaviors being sought out for responsive, adaptive, intelligent, and self-learning materials. First, it interacts with its environment by receiving a certain input (highly collimated light excitation) and adapting its structure to transform initially isotropic emission into highly directional emission, effectively mimicking the training input. In addition to this responsive behavior, it remembers over time: the longer the system is trained with the excitation input, the better the performance, and consecutive light/dark cycles show faster retraining, slower forgetting, and better final performance. The system self-optimizes and is therefore robust against fabrication imperfections, and converges to a global optimum without getting stuck in a local optimum. The self-optimization results in performance significantly beyond what can be achieved by design and nanolithography. This shows that by harvesting the right dynamics, we can transform the instability of mixed halide perovskites from a bug into a feature.

4.2 RESULTS

The system, consiting of nanophotonic microlenses on top of a perovskite film, is depicted schematically in figure 4.1. It consists of a dielectric microlens (~7 μm in size) on top of a film of methylammonium lead iodide/bromide perovskite ($MAPb(I_{0.5}Br_{0.5})_3$). Upon exposure to light, this material shows phase segregation leading to iodide-rich regions with a lower bandgap energy. Due to exciton funneling toward these regions, photosegregation results in strong, localized emission.[140] With the microlens we are able to control the photosegregation and the resulting localized emission, to obtain a desired light output. The process is indicated schematically in figure 4.1 and can be described as follows. Upon

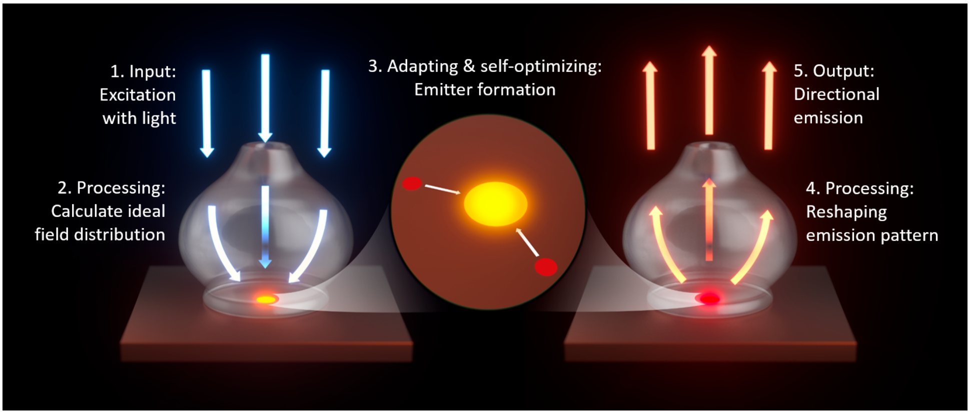

Figure 4.1: Training perovskite for highly directional light emission. A dielectric microlens of ~7 μm in size is placed on top of a methylammonium lead iodide/bromide perovskite film ($MAPb(I_{0.5}Br_{0.5})_3$). When excited by plane wave illumination (step 1), the microlens reshapes the electric field into a strong hotspot (step 2). This causes photosegregation of the halides in the mixed halide perovskite, through which the perovskite adapts and self-optimizes to form an iodide-rich region in the hotspot (step 3). This lower bandgap region acts as a localized emitter. The emitted light is again processed by the lens (step 4) into the desired output of highly directional emission (step 5).

light exposure (step 1), the microlens processes the incoming signal to a reshaped electric field distribution underneath the lens (step 2). In this case, we shape the field to a single hotspot of strong field enhancement. Under influence of the optical field, the mixed halide perovskite adapts and optimizes itself through photosegregation in the hotspot (step 3). A small iodide-rich region is formed, that acts as a localized emitter. The photoluminescence emitted from this region is again processed by the lens (step 4) into the desired pattern of highly directional emission (step 5).

Before studying the full system, the properties of the spin-coated $MAPb(I_{0.5}Br_{0.5})_3$ film without lenses are studied. Characterization of the film confirmed successful formation of perovskite (figure 4.6)a with a bandgap of 1.9 eV(figure 4.6b) and small grains, which lead to stronger photosegregation.[131, 141] Time resolved emission spectra in figure 4.2a show the expected vanishing of the initial peak at 660 nm, corresponding to fully mixed $MAPb(I_{0.5}Br_{0.5})_3$, and the appearance of a peak starting at 700 nm and red-shifting further to the expected emission of the segregated $MAPb(I_{0.8}Br_{0.2})_3$.[129, 142]

Measurements of repeated cycles of light exposure alternating with a one-minute recovery in the dark reveal that this material can be trained and has memory: consecutive cycles show faster and stronger phase segregation, as visible in figure 4.2b. Although in the dark the perovskite returns to its mixed state, some atomic-scale changes remain, which allow the next cycle of phase segregation to happen faster.[143] Extending the dark time revealed that it takes up to one hour for the material to fully return to its original state(figure 4.7). The localized emission spot from a region that was previously excited with a high intensity shown in figure 4.2c confirms this memory effect and the light-induced local emitter formation.

The time dynamics of the emitter formation are investigated with real-space images

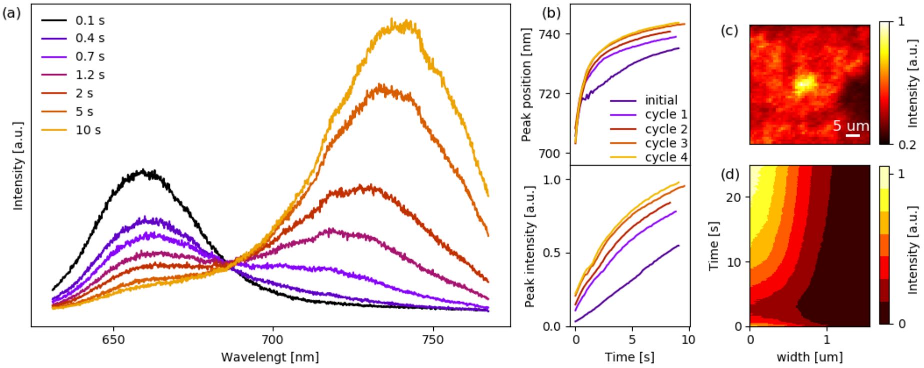

Figure 4.2: Phase segregation dynamics in the $MAPb(I_{0.5}Br_{0.5})_3$ film under 405 nm focused laser excitation. a) Emission spectra at increasing exposure times. The peak at 660 nm, corresponding to the mixed phase, disappears and a new peak at longer wavelength appears and grows over time, corresponding to the formation of an iodide-rich region. b) Development of peak position and intensity over several excitation cycles, alternating with a 1-minute recovery in the dark. After the first illumination the material responds faster. c) Spatial map of the emission intensity between 740 and 760 nm around a previously illuminated spot. A local emitter is formed. d) Emitter spot size over time, obtained from real space image as the average radial intensity. The emission is first quenched upon nucleation of the emitter, and then increases while the emitter grows.

of the film under focused laser excitation. Figure 4.2d shows the spot size as a function of time, obtained by taking the average radial intensity. First, a rapid decrease in emitter spot size is observed, followed by an increase and gradual saturation. The initial decrease is in agreement with the spectral response in figure 4.2a, where the initial peak at 660 nm disappears before the second peak starts to appear. This indicates that the emission is quenched upon the initial nucleation of the segregated region. When the light is off, some of this nucleation remains: in the next cycle, photosegregation occurs faster and the emitter is immediately formed (figure 4.9).

To further support our claim of locally forming an iodide-rich region, we have investigated the nature of the photobrightening in the process. Besides photosegregation, photobrightening has also previously been observed through photochemical surface passivation via environmental gasses.[144] To rule out this surface passivation effect, we encapsulate our samples with aluminum oxide to enhance stability and shield them from the environment.[145] We compared samples of pure bromide perovskite with and without encapsulation. Without encapsulation, it shows a strong increase in emission intensity upon light soaking, while with encapsulation photodarkening occurs (figure 4.8), indicating that the encapsulation fully blocks the photobrightning. The emission enhancement in our encapsulated mixed halide film (figure 4.2a) and the formation of localized emitters can therefore be attributed to halide segregation.

To control the observed photosegregation, we use a nanophotonic structure that reshapes the incoming light field in a designed manner. The self-optimization of our lens-perovskite system relies on the principle of reciprocity, which states that source and detector are interchangeable in an optical system. In our system, light at normal incidence is focused

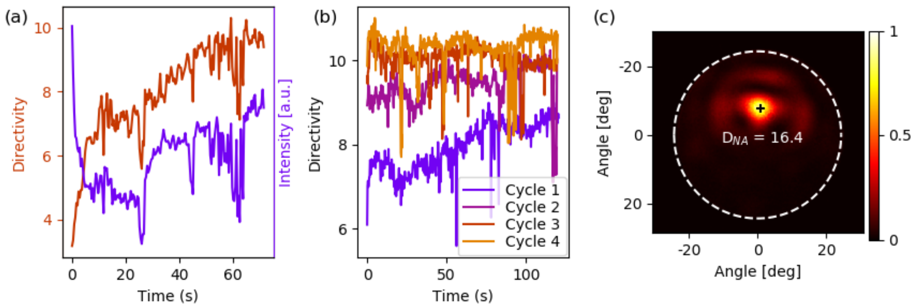

Figure 4.3: Directivity measurements during training of the lens. a) Directivity and intensity as a function of time upon initial illumination of the lens with a focused 405 nm laser. The directivity increases first rapidly and then more gradually, while the intensity first drops and then gradually increases, due to initial quenching while the emitter nucleates, followed by a growth of the emitter. b) Upon consecutive illumination cycles, alternating with a 1-minute recovery in the dark, the directivity increases each cycle due to training of the perovskite. c) Measured Fourier image of the record directivity that was reached after several cycles of light and dark. The white dashed circle corresponds to the NA of the objective of 0.42.

to the location of the hotspot via the microlens, and thus emission from the hotspot also is collimated into a narrow beam in the normal direction. The microlenses used in this study were reported to provide highly directional emission.[132] The size of these lenses can be optimized to obtain maximal directivity at a desired emission wavelength, which in this case is the wavelength of the iodide-rich regions. This lens design is particularly suitable because it is optimized based on the same principle of reciprocity that we use here for self-alignment.[65] Simulations predict a total directivity of 46 and a partial directivity within the numerical aperture (NA) of the objective of 38 for this system (figure 4.5), where directivity is defined as the emission power in the desired direction normalized to the average emission power in all directions.[80]

The directivity measurements were done using a Fourier microscope as described before.[132] This setup has an objective with a relatively low NA of 0.42, which allows for sufficiently intense excitation with a small spot size, while limiting angular spread in the excitation beam to mimic a spatially confined plane-wave source. Figure 4.3a shows the typical dynamics of the emission intensity and directivity as a function of time, when a lens is illuminated for the first time. Initially, the intensity rapidly decreases, with a simultaneous increase in directivity. We attribute this behavior to the nucleation of the emitter, in agreement with what we observed when exciting the bare film with a focused laser beam (figure 4.2a and d): the emission is first quenched before a red-shifted, enhanced photoluminescence peak rises. The concurrent rapid increase in directivity indicates that the emitter in the hotspot is already forming, and although the total intensity is low, this emission originates from the hotspot. After the first 10 seconds, the dynamics slow down. The directivity keeps gradually increasing, and the intensity stabilizes and then starts to increase around 28s, indicating a growth in emitter strength. Figure 4.3b shows the effect of several cycles of illumination separated by a one-minute recovery in the dark. Remarkably, the second cycle starts at higher directivity than the end of the first cycle, indicating the system has been trained. Initially, there likely is a competition for iodide

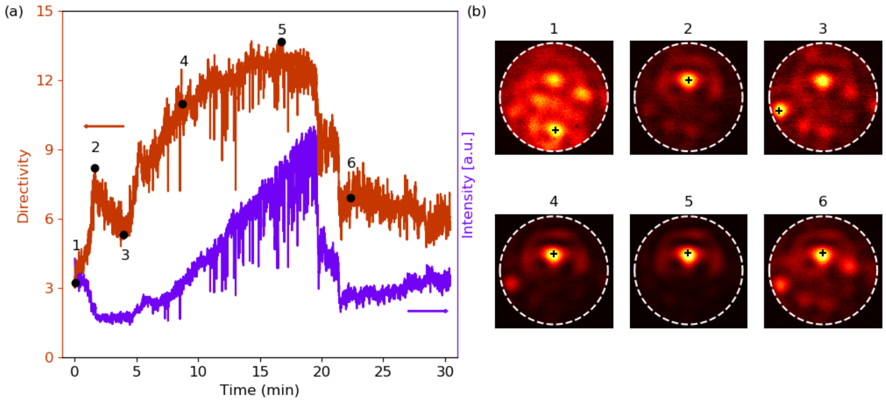

Figure 4.4: Analysis of the competition for iodide through prolonged illumination. a) Directivity and intensity as a function of time during 30 minutes of illumination. Under continuous illumination it takes longer to reach the maximum directivity compared to cycles of illumination and dark. b) Fourier images of the points indicated in panel a. Different spots correspond to different emitting regions underneath the lens. A shift in intensity between these spots indicates a change in iodide distribution. The colormaps correspond to different intensity scales, because of the large range of intensities covered. The white dashed circle corresponds to the NA of the objective of 0.42.

between different spots underneath the lens. There are mechanisms through which iodide rich regions can form away from the ideal location: either, another region also receives a small part of the excitation light due to lens imperfections, or inhomogeneities in the multicrystalline perovskite film promote the halide segregation to take place locally, for example at grain boundaries.[131, 141] This initially causes a competition for iodide between these rivaling regions and the designed hotspot, but with continuous training we observe that the designed hotspot prevails. In the dark the halides remix, but the nucleation of the iodide-rich region in the designed hotspot remains, as it is the most well-trained by the excitation light. Upon the next excitation, this region responds faster, as we have seen before, thus having an advantage over other regions that are not designed to be trained. This training behavior and retention results in higher directivity in consecutive cycles, until the system has reached its optimal configuration and the directivity stabilizes in cycles three and four in figure 4.3b. The Fourier image of the highest measured directivity of 16.4 is shown in figure 4.3c, which was obtained after several cycles of light and dark (figure 4.10).

The proposed mechanism of rivaling iodide-rich regions and subsequent victory of the designed emitter hotspot is confirmed by analyzing the Fourier patterns resulting from prolonged illumination of the system, as shown in figure 4.4. On the left, it shows again the directivity and the intensity as a function of time, but now during continuous training (illumination) over the course of half an hour. Initially, the directivity is very low, due to several bright spots in the Fourier image, most of which do not emit into the target angle (panel 1). Although different spots in Fourier space in general do not necessarily correspond to different real-space emission locations, the presence of the microlens provides a strong correlation between emitter position and angle (figures 4.12 and 4.13). In figure 4.4 the spot closest to the center of the Fourier space images, i.e. normal direction, starts to gain in intensity until point 2. Through competition for iodide, it loses power again, and directivity decreases while intensity remains constant until point 3. Here the system starts to recover and attract more iodide towards the designed hotspot, leading to an increase in intensity and directivity (point 4), until it reaches a maximum directivity of 13.9 in point 5. Then the intensity and directivity suddenly drop (point 6), which can be attributed to damage inflicted to the perovskite during extended exposure to high laser power. Under continuous illumination it takes the system more than 15 minutes to reach the maximum directivity, which is longer than it took during cycles of illumination and dark. This indicates that the emitter has a larger difficulty winning the competition for iodide under prolonged illumination. The emitter in the hotspot, which is trained, has an advantage over rivaling iodide-rich regions in the competition for iodide, as long as we make use of its retention: while the rivaling spots are 'forgotten' during the remixing, the trained spot is retained. The remixing in the dark in combination with the training of the hotspot helps the designed emitter win the competition for iodide, and thus convergence to the optimal configuration. This behaviour shows a remarkable parallel to classical nucleation and growth theory. For example, with the method of melt-recrystallization, large, high quality crystals can be formed by cycling through heating and cooling, where in each cycle the initially nucleated crystal grows. Although the system can lose all memory after an extended period in the dark, the training rate is much faster than the forgetting rate. Thanks to the self-optimizing processes, a well-trained system performs better than what could be achieved in our previous work, where we used nanolithography to spatially confine and align emitters with lenses.[132] Fabrication and alignment errors limited the directivity to 12.9, while the self-optimized system results in directivity as high as 16.4.

4.3 Conclusions and outlook

We have demonstrated how we can train a system of mixed halide perovskite with a microlens to self-optimize and retain the optimized configuration for highly directional emission. To do this, we make use of the dynamic nature of the material and the rules of reciprocity. Usually, the dynamic nature of mixed halide perovskites are regarded as unfavorable instability, but this case study shows how we utilize the process of photosegregation to make a system that mitigates fabrication errors in shape and alignment of the microlens, and therefore performs better than its traditional counterpart that is fabricated by nanolithography. We uncovered the underlying processes in the training and memory by examining the directivity and intensity as a function of time. This revealed the presence of different mechanisms, with each their own timescale. Nucleation of the iodide-rich emitter happens at a millisecond timescale, followed by further light-driven halide segregation during seconds to minutes. Competition for iodide causes further optimization over the course of tens of minutes. In the dark, the halides diffuse back within a minute, but atomic-scale changes that facilitate rapid re-segregation at the designed nucleation site remain for up to one hour. Light emission predominantly originates from the iodide-rich regions, due to energy funneling that happens at the femtosecond to picosecond time scale.[140] The presence of these different time scales makes it possible to train the system over time and provide it with a memory for the previously trained task.

This system has the capability to process an input and optimize itself to provide an output that is an adapted copy of the input signal. Once trained for a specific input pattern (in this case study simply a plane wave), it responds by mimicking this pattern. To any other input, it will reply with a much weaker response. Therefore, it complies with typical requirements for basic learning and memory capabilities in the social sciences,[133, 134] as well as recent characteristics identified for intelligent matter.[135] This proof of concept also gives the prospect for more complex learning tasks, for example leveraging reciprocity to enable pattern recognition. What we present here is the discovery of a new way of looking at the dynamics in mixed halide perovskites and a case study of how this can be used to our advantage. The insight of using material instability as a feature, to reconfigure the perovskite in a desired manner, can lead to a plethora of applications for intelligent optoelectronic materials.

4.4 MATERIALS & METHODS

4.4.1 SIMULATIONS

Optical simulations for the lens design were done with Finite-Difference Time-Domain simulations using the software program Lumerical. The directivity of the system was calculated using the open-source matlab code RETOP for the near-to-far-field transformation.

4.4.2 SAMPLE FABRICATION

Chemicals: lead acetate trihydrate ($Pb(CH_3COO)_2 \cdot 3H_2O$, 99.999%), dimethyl sulfoxide (DMSO, anhydrous ≥ 99.9%), N,N-dimethylformaldehyde (DMF, anhydrous ≥ 99.8%) were purchased from Sigma-Aldrich. Methylammonium bromide (MABr, CH_3NH_3Br, 98%), Lead iodide (PbI_2, >98%), lead bromide ($PbBr_2$, >98%), methylammonium acetate (MAAc, $CH_3NH_3CH_3COO$, >98%), and PMMA were purchased from TCI. Metylammonium iodode (MAI, CH_3NH_3I) was purchased from Solaronix. All chemicals were used as received.

Fabrication of thin films: Borosilicate glass substrate were thoroughly cleaned and UV-ozone surface treated. Mixed halide perovskite films were spin coated in a nitrogen glovebox from an 0.64M equimolar precursor solution of MAI, MABr, PbI_2, and $PbBr_2$ in DMF. 150μL was drop casted and spun for 40 seconds. At 10s, 170μL of chlorobenzene was dropcasted as antisolvent. Subsequently, the samples were annealed at 100◦C for 5 minutes. $MAPbBr_3$ films were fabricated from a precursor solution of 0.56M PbAc, 1.65M MAAc and 3.3M MABr in DMSO. 80μL of precursor solution was drop casted and spun at 5000rpm for 30s, and annealed at 100◦C for 5 minutes. Encapsulation with 15nm AL_2O_3 was done using an electron beam physical vapor deposition system (Polyteknik Flextura M508E). Encapsulation with PMMA was done using a solution of 10g/L PMMA in chlorobenzene. This solution was spin coated at 3000rpm for 30s and annealed at 100◦C for 5 minutes. Encapsulation with AlO_x and SU-8 photoresist and lens fabrication was done as described in.[132] A 1:5 diluted SU-8/cyclopentanone was used to obtain a layer of 250 nm to avoid laser damage to perovskite in the lithography process The lenses are fabricated as described before,[65] with two-photon lithography.

4.4.3 CHARACTERIZATION

Steady state absorbance spectra were measured using a LAMBDA 750 UV/Vis/NIR Spectrophotometer (Perkin Elmer). The spectrophotometer is equipped with an integrating sphere, a deuterium lamp and a tungsten lamp, and an InGaAs detector. X-ray diffraction patterns were recorded using a Bruker D2 phaser, using a Cu Kα tube. Photoluminescence spectra were recorded with a confocal imaging microscope (WITec alpha300 SR) equipped with a 405nm diode laser (Thorlabs S1FC405).

4.5 SUPPORTING INFORMATION

4.5.1 MICROLENS SIMULATION AND FABRICATION

The microlens is designed with an evolutionary algorithm, which optimizes the shape to maximize plane wave absorption, and thus field intensity, in a small region at the center of the lens. Emission from this region is then highly directional into the direction of the plane wave,[65] which is the aim in this study. Figure 4.5a shows the cross-sectional shape of the lens and the insert shows the resulting electric field underneath the lens from plane wave excitation at 405 nm as obtained from Finite-Difference-Time-Domain (FDTD) simulations. Emission from the center of the hotspot results in the simulated Fourier image shown in figure 4.5b, with a total directivity of 46 and a partial directivity within the numerical aperture (NA) of the objective of 38. Note that the directivity is lower than reported before because the continuous film of high index perovskite increases light trapping and the slightly thicker spacer layer reduces performance.

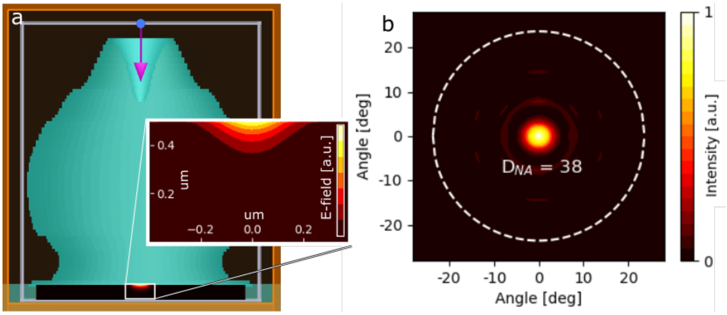

Figure 4.5: Finite-difference time domain simulations of the microlens. a) Schematic rendering of the microlens with plane wave excitation, and the resulting electric field distribution in the MHP film. Insert shows the hotspot at the center of the lens. b) Simulated Fourier image of the emission pattern, originating from a point source emitter in the center hotspot.

4.5.2 Perovskite film characterization

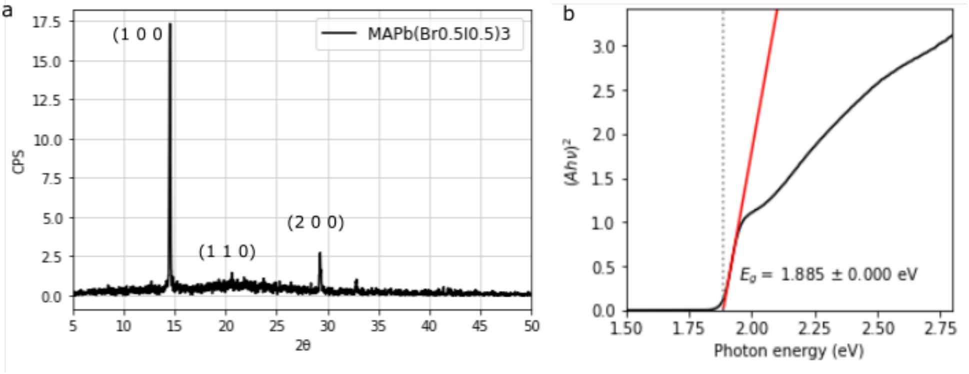

Figure 4.6: a) XRD spectrum of the MAPb($I_{0.5}Br_{0.5}$)$_3$ film showing the characteristic peaks of the cubic perovskite lattice in counts per second (CPS); b) UV-vis absorption spectrum of the MAPb($I_{0.5}Br_{0.5}$)$_3$ film, showing a bandgap of 1.9 eV.

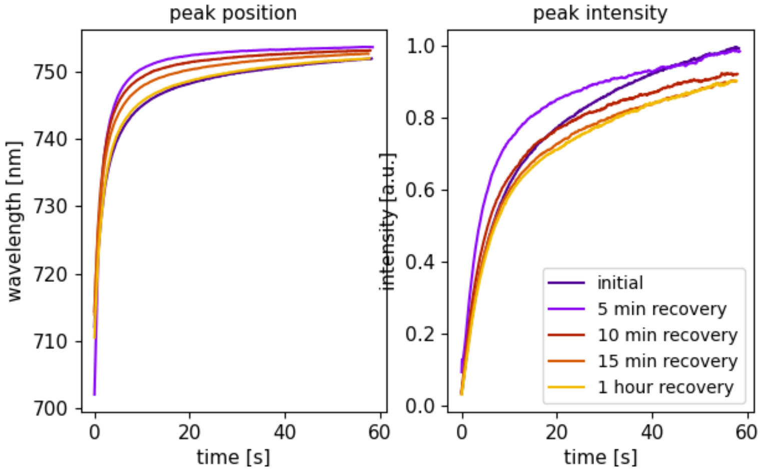

Figure 4.7: Elongating the recovery time in the dark between illumination cycles shows that it takes up to an hour for the perovskite to copmletely return to the original state, where the phase segregation dynamics are the same as for the initial illumination.

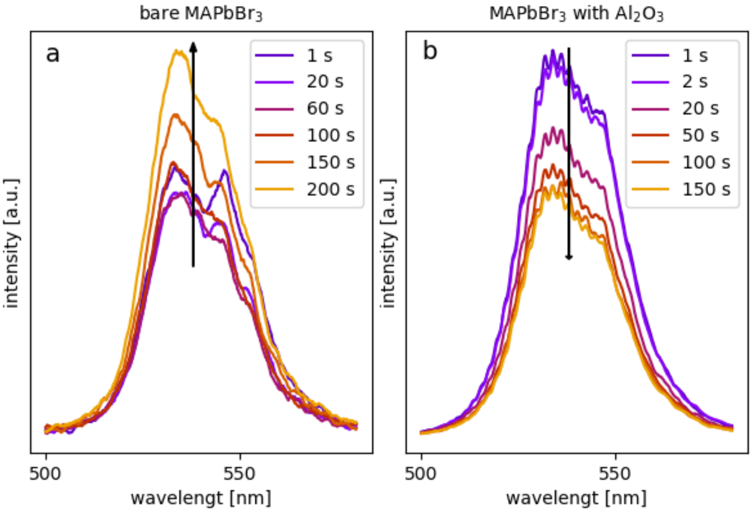

Figure 4.8: Effect of oxygen passivation on photobrightning of a single halide perovskite film. Without alumina encapsulation, the film shows photobrightning, while after encapsulation we see photodarkening. This indicates that the Al_2O_3 shields the perovskite from oxygen passivation.

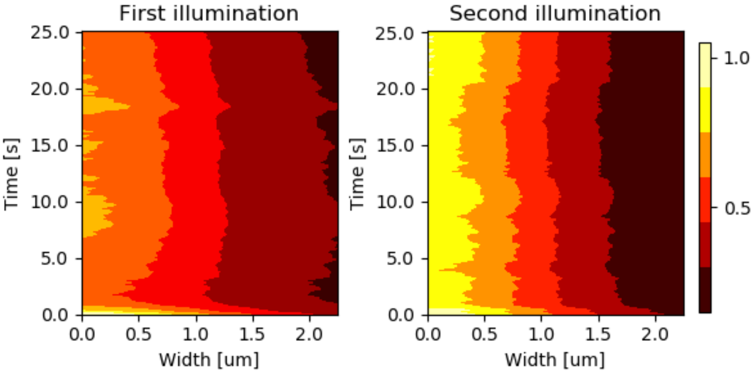

Figure 4.9: Radially integrated intensity to determine the spotsize in repeated illuminations.

4.5.3 Directivity measurements

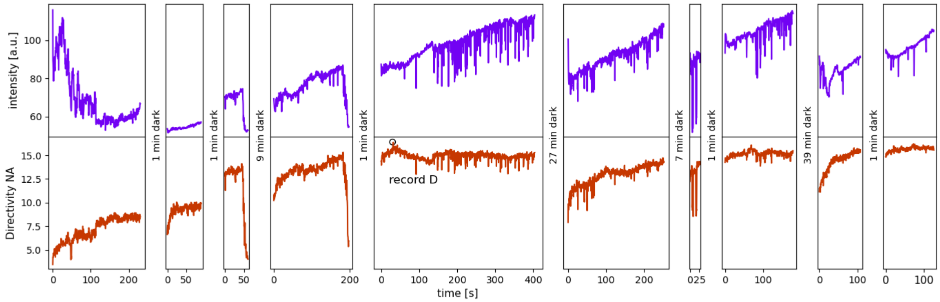

Figure 4.10: Light and dark cycles that lead to the maximum directivity of 16.4. After reaching this value the directivity stabilizes at ~ 15.

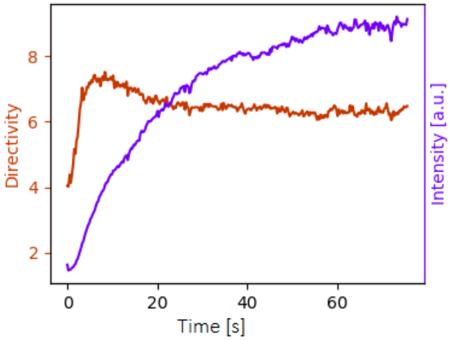

Figure 4.11: In some cases, we observed a decrease in directivity while intensity was still increasing. We attribute this to the emitter region growing too large: more emission from off-center locations underneath the lens reduces the directivity. We expect this to happen for lenses that are positioned exactly on a grain boundary, where phase segregation happens more strongly and the emitter grows more easily.

4.5.4 Simulatiosn of off-center emitters

Simulations show a strong correlation between emitter location and emission angle: when the emitter is located off-center with respect to the lens, the light is emitted under an angle, as we show in figure 4.12. With multiple off-center emitters underneath a lens, we could reproduce in in figure 4.13 the kind of emission patterns we observed experimentally in figure 4.4.

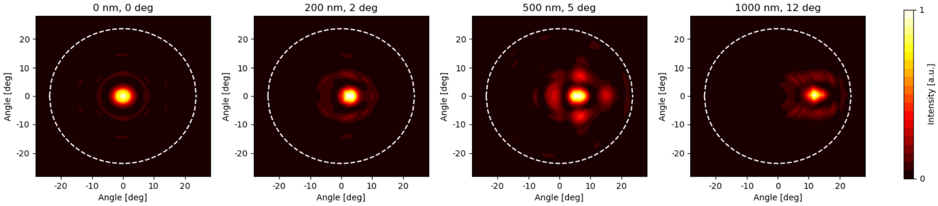

Figure 4.12: Simulated Fourier image resulting from off-center emitters. Above each figure the emitter displacement with respect to the center of the lens and the resulting beaming angle are indicated.

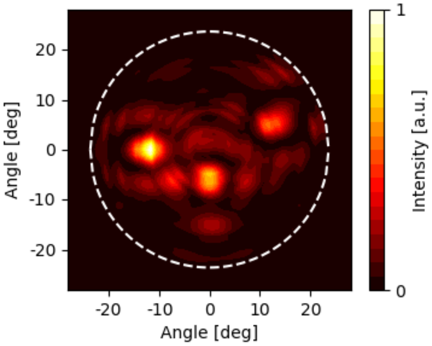

Figure 4.13: Simulated Fourier image resulting from multiple emitters underneath the lens. The three simulated emitters are located at (0,0.2), (1,0) and (-1.1,-0.5) μm with respect to the center of the lens.

5

A Solar Concentrator Exhibiting Self-Tracking and Diffuse Light Utilization

The highest solar cell efficiencies are obtained with concentrating systems. However, for practical application these systems have two major drawbacks: solar tracking is needed and diffuse sunlight is poorly absorbed. Here we present a system that overcomes both limitations, by exploiting light-induced halide segregation in mixed halide perovskite films. This approach also shows that halide perovskite instability, which is usually seen as detrimental to solar cell performance, can instead be leveraged for increased efficiency and environmental adaptability. By placing a monolayer of silica microspheres on top of the mixed halide perovskite film, incoming direct sunlight is focused into a hotspot under each of the microspheres. In the hotspot, light-induced phase segregation takes place, and locally a low bandgap region is formed. This focusing of the spheres, in combination with the funneling of excited states towards the low bandgap regions, results in a voltage increase characteristic for concentrating systems. Diffuse sunlight from any direction will still be absorbed by the high bandgap material, avoiding this loss mechanism of conventional concentrators. The formation of low bandgap regions in the perovskite is dynamic and can follow the position of the hotspot as the sun moves throughout the day, making solar tracking unnecessary. With detailed optical and electrical simulations, we show that this concept can lead to an increase in both voltage and current, due to a combination of enhanced light absorption and carrier concentration. This leads to an up to 6.8% absolute increase in power conversion efficiency compared to the film without microspheres. Experimental verification confirms both the absorption enhancement and directional light emission that, where the latter is a signature of effective concentration. This shows the promising potential for exploiting rather than avoiding halide segregation in perovskite solar cells for a self-optimizing concentrating system.

5.1 Introduction

Concentrator photovoltaics are the record holders in photovoltaic efficiency.[146] However, for practical applications, these systems have two major limitations. The first is the need for solar tracking, which leads to bulky and expensive mechanical systems. The second problem is the fact that diffuse sunlight is not efficiently absorbed in concentrating systems. In most terrestrial applications, the loss in absorption due to the presence of diffuse sunlight completely counteracts the efficiency gain due to concentration.[87] In this chapter, we present a new concentrating solar cell that automatically tracks the sun and is able to collect the majority of diffuse light, overcoming the two major limitations of modern-day concentrators.

To understand the working principle of this concept, we need to understand what makes a concentrating system more efficient. The efficiency of a solar cell is determined by the short circuit current (J_{sc}), the open circuit voltage (V_{oc}), and the fill factor. The V_{oc} is given by the equation $V_{oc} = k_BT/q \ln (J_{sc}/J_0)$, with J_0 the dark recombination current, k_B the Boltzmann constant, T the temperature in Kelvin, and q the elemental charge. In a concentrating system, V_{oc} is enhanced because the ratio of J_{sc}/J_0 is increased. The underlying mechanism for this increase is directivity. Directivity means that emissivity, and thus absorptivity, is high in one direction, and lower in all other directions. This ensures that the sunlight is focused, while most of the thermal background is not. For a macroscopic concentrator, one can see it as a fixed solar cell size with fixed thermal background absorption, where more sunlight is absorbed since it is concentrated from a larger collection area. Alternatively, one can view it as a decrease in thermal background absorption as the solar cell size is decreased for a fixed collection area. In nanophotonic systems, this geometric optics picture breaks down,[21] which makes directivity a more suitable measure for defining the concentration factor.[46] Here one can view the increase in V_{oc} as a reduction in J_0 caused by limiting the angles from which the solar cell absorbs and in which it emits thermal radiation. In all cases, the net effect is an increase in free carrier concentration in the material, resulting in higher quasi-Fermi level splitting and thus higher V_{oc}.

To overcome the limitations in diffuse sunlight absorption, a system is needed that absorbs high energy photons from all directions (the diffuse light) and has a high directivity around the bandgap, such that at the emission wavelength recombination is reduced.[87] High directivity over all wavelengths is what standard concentrator systems show, but for the V_{oc} improvements you can get nearly all the gains making only the bandwidth around the emission peak directive. This allows at the same time for most of the diffuse light also to be collected. This behavior can be achieved by having low-bandgap emitters embedded in a higher bandgap matrix, with concentrating microlenses on top of the emitters. The high-bandgap matrix absorbs high-energy light from any direction. Excited states are funneled to the low-bandgap regions, which gives an effective concentration of carriers. The low-bandgap regions underneath the microlenses absorb most of the direct sunlight down to the low-bandgap energy. Due to the energy funneling, emission predominantly originates from these regions. Through coupling back into the microlenses, the emission will be directive. This concept is shown schematically in figure 5.1.

To make such a system easy to fabricate, and avoid the need for solar tracking, a self-aligning lens-emitter system is needed. This can be achieved with a material that locally

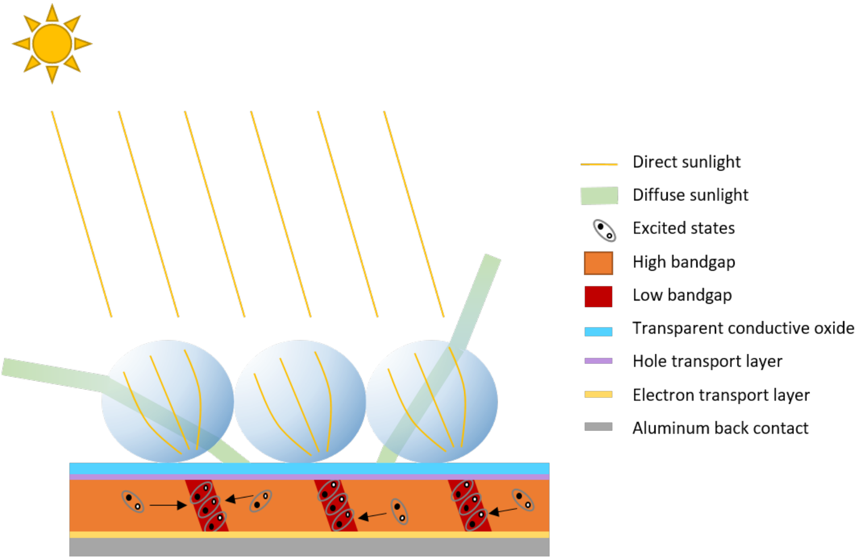

Figure 5.1: Schematic representation of the self-tracking solar concentrator with absoprtion of diffuse sunlight. Microspheres focus the direct sunlight to a hotspot in the underlying film. In the hotspot a low bandgap material is formed, where excited states get concentrated. Diffuse sunlight from any direction is absorbed in the high bandgap matrix and the resulting excited states are funneled to the low bandgap regions. The postition of the hotspot, and thereby of the low bandgap phase, moves along with the motion of the sun.

converts into a lower bandgap under the influence of light. The lens should accept a light beam from any angle of incidence and focus it into a hotspot. In this hotspot, under the influence of light, the low-bandgap material forms. The rules of reciprocity then dictate, that since this hotspot has strong coupling to the incoming sunlight, emission from this region will also be highly directional towards the incoming light beam, in this case direct sunlight. Diffuse sunlight, coming from any other angle, will still be absorbed by the high-bandgap material.

An excellent material with the desired behavior is mixed halide perovskite, which tends to segregate into lower bandgap regions under light illumination. Halide perovskite thin films are in general good candidates for efficient solar cell devices, surpassing all expectations in terms of solar cell efficiency over the past decade.[146] Their facile processability, strong absorption, and long carrier diffusion lengths are a few of their most attractive qualities for photovoltaics.[147,148,149] Additionally, one of their core qualities is that the bandgap of the material can be tuned by mixing halides, where a combination of bromide and iodide can give the highest efficiency single-junction solar cell.[150] Under illumination, the uniform alloy tends to segregate into iodide- and bromide-rich regions, with respectively lower and higher bandgap. This has been considered a major limitation, as without additional measures this segregation reduces photovoltaic efficiency.[150,151] This reduced efficiency is a consequence of carriers funneling towards the low bandgap regions, by which the recombination, and thus J_0 and V_{oc}, become fully determined by this low bandgap phase. However, for the system described above, this halide segregation is exactly the desired behavior. We have shown in previous work that the formation of iodide-rich regions can be controlled through the use of microlenses (chapter 4). The specially designed and fabricated microlenses create a strong hotspot in the underlying material,[132] where through halide segregation and energy funneling a local emitter with high directivity is formed.

Nonetheless, the previous approach has limitations. Due to the special design of the microlenses, the fabrication of each individual lens is time-consuming and not straightforward on a perovskite layer. Furthermore, this system only performs well for normal incidence, while the principle of reciprocity can be applied to any nanophotonic structure that creates a hotspot somewhere in the material when illuminated with a plane wave from any direction. To harvest the beneficial effects that were described for application in self-tracking concentrator photovoltaics, a lens is required that can be processed on larger scales and accept light from any angle of incidence. Silica microspheres are an excellent candidate for this job. They can focus light to produce photonic nanojets,[152, 153] albeit with a lower directivity than the previously reported microlenses.[65] They can be easily synthesized with various sizes and excellent monodispersity,[154] and subsequently assembled in large-scale arrays of hexagonally packed spheres.[155] With a monolayer of microspheres on top of a mixed halide perovskite film, the system as depicted in figure 5.1 can be achieved. The incoming direct sunlight will be focused into a hotspot underneath each sphere, where locally a lower bandgap iodide-rich region is formed. Absorption and emission at the low bandgap wavelength will be only enhanced in the direction of the incoming direct sunlight. Diffuse sunlight from all other directions at higher energy will still be absorbed in the unsegregated regions of the film, avoiding the decrease in absorption of diffuse light displayed by conventional solar concentrator devices. We have seen before (chapter 4) that the emitter formation in the perovskite is not permanent, and ions stay mobile in the perovskite layer. This makes tracking of the sun to ensure normal incidence not needed; the iodide-rich regions can move underneath the spheres and follow the movement of the sun. Assuming the iodide-rich regions extend from the top to the bottom contact, the carriers can be collected for all lateral positions of the low bandgap regions (sunlight incident angles).

In this chapter, we analyze and quantify the effect of placing a monolayer of micrometer-sized silica spheres on top of a mixed halide perovskite film on solar cell performance. With optical simulations, the reciprocity between hotspot formation and directivity of emission is investigated for a varying angle of incidence, and the effect on solar cell absorption and emission is modeled. Through detailed balance calculations and electrical simulations of a full solar cell device, the effect on the solar cell performance is investigated and a large performance increase is found with the use of microspheres. Furthermore, we provide experimental proof of concept by assembling arrays of hexagonally packed spheres on a mixed halide perovskite thin film. Changes in absorption and emission directivity due to the presence of the spheres in agreement with the simulations are observed. This concept, of combining the optical properties of silica microspheres with the dynamic nature of mixed halide perovskites, can overcome the limitations of both concentrator systems and mixed halide perovskite solar cells, which opens up a new pathway to high-efficiency perovskite solar concentrators.

Sphere radius	2 μm	3 μm	4 μm	5μm	6 μm	8 μm	10 μm
Directivity	20	30	40	51	80	97	153

Table 5.1: Directivity from silica microspheres on a glass substrate, from an dipole emitter at the center of the hotspot when illuminated with a plane wave at normal incidence. Directivity increases with sphere size, due to increasing quality factor.

5.2 RESULTS AND DISCUSSION

5.2.1 SIMULATIONS

How the silica microspheres perform in terms of hotspot formation, directional emission, and potential array effects was investigated with Finite-Difference Time Domain (FDTD) simulations. When a single glass sphere is illuminated with a plane wave at normal incidence, a strong field enhancement, a nanojet, is observed in the substrate underneath the center of the sphere (figure 5.2a). The location of the nanojet dictates where a localized iodide-rich perovskite emitter is formed. To investigate the directionality of the light emitted from this region, a dipole emitter is placed at the position of the nanojet. The resulting emission pattern shows narrow beaming into the upwards direction (figure 5.2e). Directivity rapidly increases with sphere size, due to the increasing quality factor of the cavity (the sphere), as summarized in table 5.1. The ideal size of the spheres is a trade-off between maximizing directivity and energy funneling towards the hotspot. If the spheres become too large, emission from the higher bandgap film in between the hotspots might become significant, because the spheres exceed the carrier diffusion length in the perovskite and the carriers cannot reach the low bandgap regions. This reduces the concentrating effect. All further simulations are done on 5 μm diameter spheres, mostly motivated by the commercial availability of this size for experimental verification. Potentially, the ideal size is larger because perovskites are known for their long diffusion lengths up to tens of micrometers. Simulations of 5 μm diameter spheres in a hexagonal array yield the same pattern of a single hotspot underneath each sphere for plane wave excitation, and the same emission pattern from a dipole at the hotspot in the center of the array. This indicates that no array effects are present.

The reciprocity between incoming angle, hotspot location and emission angle was verified on a hexagonal layer of 5 μm diameter spheres on a glass substrate. The array is illuminated with plane wave excitation under increasing angle of incidence, from 0 to 45 degrees. The resulting field intensity in the substrate underneath the spheres is shown in figure 5.2a-d. Upon increasing the angle of incidence in clockwise direction, the hotspot moves towards the left. Subsequently, a second simulation is run, with a dipole emitter placed at the location of the hotspot (with the plane wave excitation turned off). The resulting emission patterns are shown in figure 5.2e-h. Up to a 40 degrees angle of incidence excitation, there is an almost perfect correspondence between the excitation angle and the emission angle, as expected from reciprocity. At 45 degrees, the hotspot is moved almost a full sphere radius to the side, and thus moves underneath the neighboring sphere, as visible in figure 5.2d. Emission from this hotspot location starts to couple to the next sphere, resulting in emission in the opposite direction of -45 degrees, as visible in figure 5.2h. The iodide-rich regions formed in the hotspot can thus follow the movement of the sun over a cone of 80 °. This allows for automatic solar tracking without any mechanics

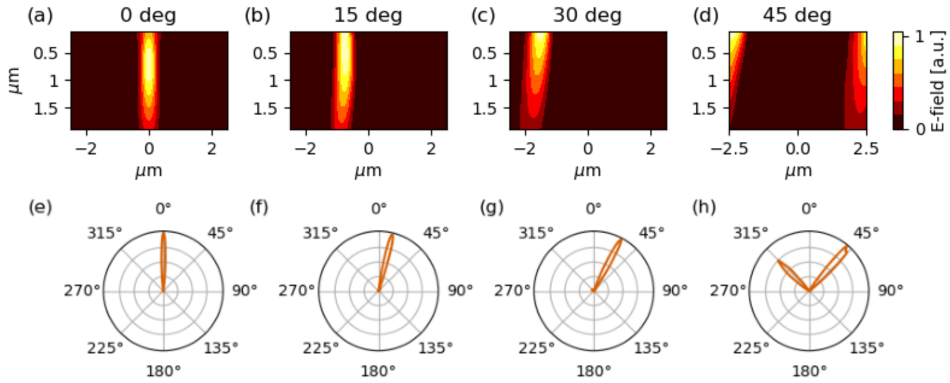

Figure 5.2: Optical simulation results of 5 μm silica spheres on a glass substrate. Top row: electric field intensity in the substrate underneath the center of the sphere for plane wave illumination with increasing angle of incidence. Bottom row: far-field emission pattern from a dipole source placed at the position of maximum field intensity in plane wave illumination. The emission is beaming back into the direction of the incidence field due to laws of reciprocity. At 45°, the emitter starts to couple to the neighboring sphere, and part of the emission is beamed into the opposite direction.

having to be added to the modules, as the cone covers the brightest sun hours of the day.

We have investigated the potential solar cell performance of a mixed halide perovskite film with a monolayer of silica spheres through detailed optical and electrical simulations. The system under study consists of a 500 nm thick film of $MAPb(I_{0.5}Br_{0.5})_3$ on top of an aluminum back contact. As a top contact, a uniform layer of Indium-Tin-Oxide (ITO) is used, with a thin film of SU8 photoresist on top which is needed for encapsulation and adhesion of the spheres. Although carrier selective contacts are not included in the optical model, in the ideal case they are only a few (5-15) nm thick and thus do not substantially effect the optical modeling. A hexagonal array of close-packed silica spheres forms the top layer. Since the ITO and SU8 have a refractive index in between those of the perovskite and air, these layers can also act as an anti-reflection coating. It was found that absorption in the perovskite is maximized for an ITO layer thickness of 50 nm and an SU8 layer thickness of 80 nm, where the lower limit of ITO thickness was set to 50 nm to ensure sufficiently low series resistance values (figure 5.5). For calculating the performance in the radiative limit, accurate modeling of J_0 is required, as this limits the open circuit voltage. J_0 is determined by the external quantum efficiency and the black body radiation spectrum.[33] Since the black body emission exponentially increases at lower energy, J_0, and thus V_{oc}, is very sensitive to the low energy tail states of the absorptivity/emissivity spectrum.[156] This is also the reason that halide segregation is usually undesirable in solar cells. Only one percent of a low bandgap phase can dominate the emission spectrum. This is known as voltage pinning, where the V_{oc} is completely determined by the lowest bandgap phase. Away from the radiative limit, non-radiative recombination becomes the dominant factor in limiting the voltage,[130] but for determining the ideal performance in the radiative limit, it is important to accurately model the tail states of both unsegregated and segregated phases. Details on how this was done can be found in the Supporting Information.

We have investigated several systems of perovskite films in different phases, with and without a monolayer of spheres, which allows us to separate the contribution of the different mechanisms that play a role in the final solar cell performance. We compare an unsegregated film (from now on denoted high bandgap film), consisting of 50:50 iodide:bromide ratio perovskite and a bandgap of 1.9 eV, a film completely consisting of 80:20 iodide:bromide ratio perovskite with a 1.7 eV bandgap, which is the phase in which the mixed halide perovskite locally segregates[129] (denoted low bandgap film), and a perovskite with the high bandgap material as majority phase and 3.6% minority phase of the low bandgap material. We assume that changes in the halide ratio in the high bandgap material are negligible, because of the low fraction of low bandgap phase that is formed. The minority phase regions are modeled as 1 μm diameter cylinders throughout the film underneath each of the spheres. This corresponds to the shape and size of the hotspot that is formed under broadband, plane wave illumination (figure 5.7), and thus how phase segregation is expected to occur. For each of these films we determine the absorption spectrum with and without spheres. The resulting absorption spectra are shown in figure 5.3a. With detailed balance calculations, the performance of these systems in the radiative limit is determined, as summarized in table 5.2 and shown graphically in figure 5.3b, filled markers.

Without spheres, a large drop in V_{oc} of 130 mV occurs when the high bandgap film segregates into the two phases, due to the above-mentioned voltage pinning of the low bandgap phase. The increase in absorption above 650 nm is almost negligible, as can be seen in figure 5.3a, resulting in only 0.2 mA/cm^{-2} increase in J_{sc}, and overall efficiency goes down by 1.2%. The bare low bandgap film has 200 mV lower voltage but significantly higher J_{sc} due to the lower bandgap. The efficiency is higher because the bandgap is closer to the optimum value. A monolayer of spheres enhances the absorption in the high bandgap film by 0.3 mA/cm^{-2}, due to a change in the interference in the film, while the voltage is unchanged. In the low bandgap film, J_{sc} is unaffected. In the two-phase system, however, there is a large increase in both voltage and current in presence of the spheres. The increase in J_{sc} can be attributed to the focusing by the spheres. The incoming sunlight is focused into the low-bandgap material, which gives a large increase in absorption between 650 and 750 nm, despite the fact that there is only 3.6% of the low bandgap phase present. This increase in absorption results in an increase in emission as well, due to effective lowering of the bandgap, but at the same time the directivity of the spheres reduces the radiative recombination, and the overall effect is an increase in V_{oc} of 20 mV compared to the bare segregated film. The increase in J_{sc} gives an increase in voltage of $k_B T/q \ln(16.1/12.3) = 8$ mV, the directivity of the spheres gives an increase of $k_B T/q \ln(27) = 85$ mV, and thus the lowering in the bandgap decreases the voltage again by 73 mV. The spheres give an absolute 6.8% efficiency increase compared to the bare two-phase film. The resulting efficiency of 23.8% is higher than for both unsegregated films. The difference with the low bandgap film is relatively small, because this low bandgap is closer to the ideal value for a single junction solar cell. As we will see in the following, the concentrating effect of the spheres gives some additional benefit in the presence of non-radiative recombination, which makes the segregated system even more favorable over the all low bandgap film. Also for application in tandem configuration, efficient high-bandgap perovskite solar cell designs are needed.

To obtain more realistic performance metrics, which include the effects of electrical contacts and non-radiative recombination, each of the above-mentioned devices is simulated

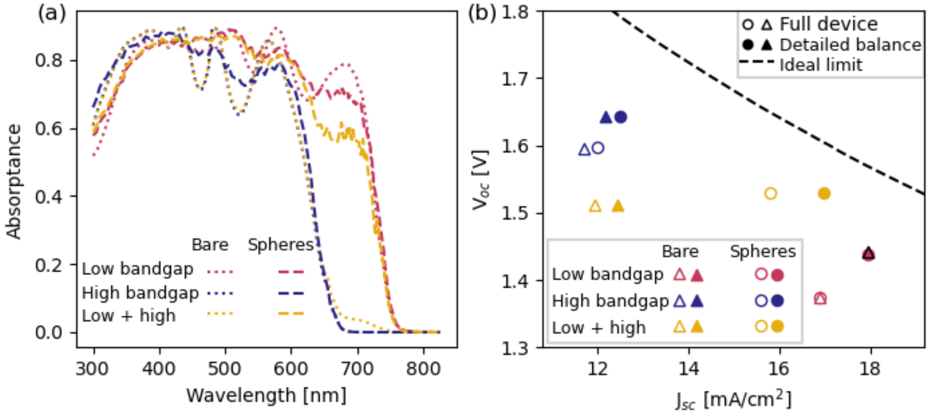

Figure 5.3: Absorption spectra and device performance simulation results for the 6 different systems: low bandgap (1.7 eV) film, high bandgap (1.9 eV) film, and phase segregated film with 3.6% low bandgap regions in a hight bandgap film, each as bare film and with a monolayer of 5 μm silica spheres on top. a) Absorption spectra obtained from FDTD simulations b) Open circuit voltage (V_{oc}) and short circuit current (J_{sc}) obtained from detailed balance calculations and full device simulations, based on the absorption spectra in (a). The black dotted line gives the ideal limit from detailed balance calculations assuming step-wise absorption onset, thus no tail states. The two-phase system with spheres approaches this limit most closely.

	Bare film			With spheres		
	J_{sc}	V_{oc}	η	J_{sc}	V_{oc}	η
Low bandgap (1.7 eV)	18.0	1.44	23.6	18.0	1.44	23.5
High bandgap (1.9 eV)	12.2	1.64	18.4	12.5	1.64	18.9
Low + high bandgap	12.4	1.51	17.2	17.0	1.53	23.8

Table 5.2: Solar cell performance in radiative limit as obtained from detailed balance calculations, based on the absorption spectra in figure 5.3a. The phase segregation lowers V_{oc} and thereby efficiency, while spheres increase J_{sc} and efficiency. The combination of spheres and phase segregation gives rise to a large increase in both J_{sc} and V_{oc}, thanks to absorption enhancement and directional light emission, which results in a 6.8% higher efficiency compared to the segregated film without spheres. J_{sc} in mA/cm^{-2}, V_{oc} in V, η in %.

in Lumerical Device CHARGE. The generation profile from the AM1.5 solar spectrum is obtained with the same optical FDTD simulations as the absorption spectra in figure 5.3a and imported into Device. The electrical model includes hole and electron selective layers and planar contacts on each side. Details on the simulation and materials settings can be found in the Supporting Information. The obtained performance metrics are summarized in table 5.3 and shown graphically in figure 5.3b, open markers. Now the two-phase system with spheres stands out even more. While the drop in voltage compared to the radiative limit for the pure low and high bandgap systems is respectively 60 mV and 40 mV, the two phase system with spheres drops only 20 mV. This reduced voltage drop is caused by a combination of two effects, both related to the enhanced carrier concentration in the low-bandgap cylinders underneath the spheres. This increased carrier concentration leads to the increases in V_{oc} that is always observed in concentrating systems, also in the radiative limit. However, in the presence of non-radiative recombination, there is an additional benefit from increased carrier concentrations. The dominant non-radiative recombination pathway, Shockley-Read-Hall recombination, scales linearly with carrier concentration. The radiative recombination rate scales with the carrier concentration squared. Higher carrier concentrations thus push the system toward the radiative limit, increasing the internal quantum efficiency and thereby the voltage. Furthermore, the long diffusion lengths in perovskite allow for efficient funneling towards the low-bandgap regions: with the lifetime and mobility in the simulations of 1 μs and 15 $\mathrm{cm^2V^{-1}s^{-1}}$ respectively, the carrier diffusion length of 7 μm is large enough compared to the radius of the sphere. Therefore most recombination occurs in the segregated regions, as all carriers are funneled towards the hotspots. Proof of this funneling effect was found by comparing the recombination rates in the segregated system without spheres to the all low bandgap system without spheres. Since there is no focusing of the spheres, absorption per unit volume in the low bandgap cylinders is the same as in the all low bandgap film. However, carrier concentrations are up to an order of magnitude larger in the segregated film, which indicates that electrons and holes from elsewhere in the film recombine in the segregated regions. This funneling effect is not taken into account in the radiative limit calculations and explains the absence of a voltage drop for the segregated film without spheres from the radiative to the non-radiative system.

5.2.2 EXPERIMENTS

The optical effects of adding a monolayer of glass spheres on a perovskite film have also been demonstrated experimentally. A $MAPb(I_{0.5}Br_{0.5})_3$ film is spin-coated on a glass substrate and encapsulated with a 15 nm aluminum oxide layer for enhanced stability as described before chapter 4. Monolayers of silica spheres were created with a simple rubbing technique, where a dry powder of spheres is gently rubbed between two slabs of PDMS.[155] This resulted in large area (several square milimeters) monolayers of spheres on PDMS. The spheres do not stick well to the perovskite/alumina film, potentially due to the difference in hydrophobicity and the surface roughness of the film. Successful transfer to the perovskite film was obtained by spin coating two 100 nm thick layers of SU8 photoresist. The first layer flattens out any irregularities on the film and further protects the perovskite. Directly after spin coating the second layer and before curing it, the slab of PDMS with a monolayer of spheres is pressed into the film, by which the spheres stick into the photoresist and are

	Bare film			With spheres		
	J_{sc}	V_{oc}	η	J_{sc}	V_{oc}	η
Low bandgap (1.7 eV)	16.9	1.38	20.2	16.9	1.38	20.1
High bandgap (1.9 eV)	11.7	1.60	16.3	12.0	1.60	16.7
Low + high bandgap	11.9	1.51	15.6	15.8	1.53	20.7

Table 5.3: Solar cell performance in full device simulations, including non-radiative recombination as Shockley-Read-Hall recombination and surface recombination. Enhanced carrier concentrations due to the focusing of the spheres and funneling to the low bandgap regions drive the system towards more radiative recombination, resulting in less penalty in V_{oc} due to phase segregation. The segregated system with spheres gives the highest efficiency. J_{sc} in mA/cm^{-2}, V_{oc} in V, η in %.

transferred to the sample (figure 5.6). A single layer of SU8 was not sufficient, because the spheres had to be pressed into the film with a large force in order to obtain a proper transfer, but as a consequence the spheres appeared to be pressed into the perovskite, resulting in damage to the perovskite film.

Accurate absorption spectrum measurements on the film with and without spheres, to verify the spectra in figure 5.3, were hindered by the high photoluminescence of the films, which keeps increasing under prolonged illumination (figure 5.8). This complicated accurate absorption measurements around the bandgap. Accurate absorption spectra at short wavelength were obtained using an integrating spheres setup as described before,[118] using short pass filters to remove any photoluminescence (PL) from the signals. Subsequently, simple transmission and reflection measurements were taken over the full spectrum with the detectors far away from the sample, to minimize PL signals. These measurements result in an anomously high apparent absorption, because scattered light is not detected. By matching the spectrum to the integrating sphere measurements at short wavelengths, the amount of scattering could be determined. Assuming that this value is constant over the measured spectrum, accurate absorption values around the bandgap could be obtained from the transmission/reflection measurements, which are shown in figure 5.4a. At short wavelengths, the film with spheres has ca 4% more absorption compared to the bare film, due to the anti-reflection effects of the spheres. Towards the bandgap of the mixed-phase film, absorptance rapidly drops for the bare film, although there is a second bump in the absorption spectrum that corresponds to the absorption of the iodide-rich phase. In this spectral region, the film with spheres shows up to 25% more absorption. This confirms the hypothesis that iodide-rich regions are self-aligned with the spheres, which focus the light into those regions, with a large increase in absorption as a result. The fact that for both samples absorption is higher than in the simulations indicates that there is more iodide-rich phase forming. The absence of the interference pattern in the bare film absorption, as seen in the simulations, can be explained by the surface roughness of the perovskite film, which

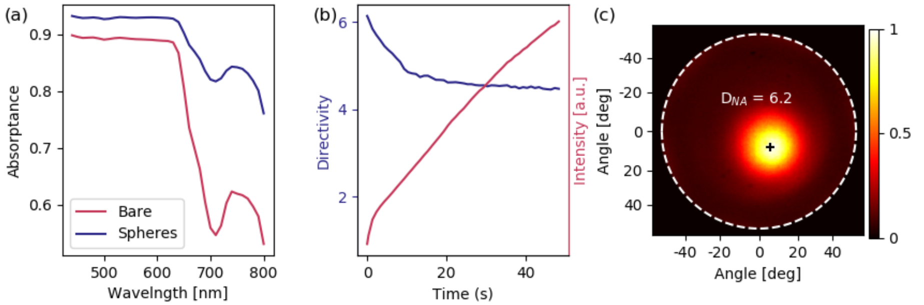

Figure 5.4: Experimental results on mixed halide perovskite films with a monolayer of silica spheres on top. a) Absorption spectra show an increase in absorptance over all wavelengths. At short wavelengths, this can be attributed to anti-reflection effects, while in the 700 to 800 nm range this can be attributed to focussing into the low bandgap regions underneath the spheres. b) Directivity and emission intensity as a function of time. Directivity decreases over time, potentially due to the segregated regions growing too large. c) Fourier image of the highest measured directivity of 6.2. in the NA of the objective

was not taken into account in the simulations. Given the chemical flexibility of halide perovskites and the resulting effects on the light-induced phase separation, we expect that the size of the phase separation at a given light intensity can be controlled.

Directivity measurements were done with a Fourier microscope in full-field illumination mode. In this configuration, the sample is illuminated with a plane wave, and the directivity of an ensemble of ca 50 spheres is measured (figure 5.9). The development of directivity and emission intensity over illumination time is shown in figure 5.4b, with a Fourier image of the highest directivity measurement in figure 5.4c. Upon initial illumination, the highest directivity of 6.2 is measured, but longer illumination results in a decrease in directivity. This trend opposite of what would be expected can be attributed to iodide-rich regions growing too big. Emission in normal direction is only obtained from emission from the center of the spheres. If the iodide-rich region grows and emission happens from a large area underneath the sphere, directivity is decreased. This is in agreement with our absorption measurements in figure 5.4a, where we also observed that more and/or larger iodide-rich regions are formed compared to our simulations.

5.3 CONCLUSION AND OUTLOOK

In this work, we have shown how light-induced halide segregation in mixed halide perovskites can be exploited to improve solar cell performance. By placing a monolayer of silica microspheres on top of the perovskite layer, phase segregation can be controlled to take place in a highly functional manner. Each sphere focuses the incoming sunlight into a hotspot. In this hotspot halide segregation occurs and a lower bandgap region is formed, which acts as a local emitter. Due to the rules of reciprocity, light emitted from this region will be highly directional into the direction of incoming light. With optical simulations, we showed that reciprocity between incoming light, hotspot formation and emitted light works for any angle of incidence between -40° and 40°. When this system is applied in a solar cell, the focusing of the spheres causes an increase in J_{sc} of 4.6 mA/cm^{-2} and an increase in V_{oc} 40 mV in the radiative limit, resulting in an absolute increase in efficiency of 6.8%. In a complete device configuration, including non-radiative recombination and extraction losses, increases in J_{sc} and V_{oc} are 3.9 mA/cm^{-2} and 20 mV respectively, and efficiency is increased by 5.1%. Due to additional benefits of the increased carrier concentration within the segregated regions, the voltage drop in the segregated films from the radiative limit to the full device is less compared to the single phase films. Experimental verification showed that the presence of a monolayer of spheres on a perovskite film indeed increases the absorption significantly. This especially happens in the region between 650 and 800 nm, as light is focused on low bandgap regions that are formed in the film. Also, directional emission was observed experimentally, with directivity of 6.2 within the NA of the objective.

A logical next step after these initial experimental proofs of concept is to measure full device performance experimentally. This requires the fabrication of a fully contacted device. Since the sphere monolayer can be simply added to the device at the end, via the same procedure as described for the optical experiments, full device fabrication is within reach. A more challenging aspect is the further optimization of the mixed halide perovskite film. Our experiments indicate that more phase segregation happens than what was assumed in the simulations. Some of this might be attributed to the relatively small excitation area used in experiments, which might cause the formation of iodide-rich regions everywhere in the illumination area, instead of only underneath the spheres (figure 5.10). The mixed halide perovskite films used here consist of very small grains, which give strong phase segregation. Larger grains might lead to less phase segregation, resulting in smaller emitters and higher directivity. However, initial experiments with large grain films resulted in rough films with large variations in PL intensity and spectrum throughout the sample, which complicated the transfer of spheres and optical characterization. By combining methods to decrease phase segregation, for example by altering the A-site cation which drastically changes the ion photosegregation process, and further optimizing the iodide:bromide ratio for best performance, we believe that the outstanding performance predicted by simulations can become reality.

Overall we can conclude that a simple, scalable technique of placing a monolayer of silica microspheres on top of a mixed halide perovskite film can significantly improve solar cell performance. A combination of anti-reflection and focusing effects causes an increase in J_{sc}. Directivity or concentration (effectively the same effect) increase V_{oc}, with an additional boost in V_{oc} in the presence of non-radiative recombination due to increased carrier concentration, which pushes the system towards the radiative limit. This approach, in which we embrace the light-induced phase segregation rather than preventing it, can open up a new path for high-efficiency perovskite solar concentrators.

5.4 MATERIALS & METHODS

Chemicals: MABr (≥98%), MAI (≥99%), $PbBr_2$ (≥98%), and PbI_2 (≥99.99%) were purchased from TCI. Chlorobenzene (≥99.8%) and dimethyl formamide (DMF, anhydrous ≥ 99.8%) were purchased from Sigma-Aldrich. All chemicals were used as received.

Substrate preparation: Fused quartz substrates of 15 mm×15 mm×1 mm were cleaned with soap and subsequentially sonicated in water, acetone, and isopropanol. The dried substrates were then UV/ozone treated for 20 minutes and quickly brought into a nitrogen glovebox afterwards.

MAPb($Br_{0.5}I_{0.5}$)$_3$ thin film fabrication: Film preparation took place in nitrogen glovebox. An 0.64 M equimolar solution of MABr, MAI, $PbBr_2$, and PbI_2 was made in DMF and stirred over night at 70°C. The solution was filtered using a 0.2 μm syringe filter. Thin films were then fabricated by spin coating 80 μl of the precursor solution at 3000 rmp for 40 seconds. After 10 seconds, 200 μl chlorobenzene antisolvent was dropcasted on the spinning sample. To crystallize, the sample was placed on a hot plate to anneal for 5 minutes at 100°C.

Encapsulation of thin films: Encapsulation with 15 nm AL_2O_3 was done using an electron beam physical vapor deposition system (Polyteknik Flextura M508E). Afterwards, the films were coated with two layers of 100nm SU-8, obtained by a mixture of SU-8/cyclopentanone in a 1:10 ratio that was spin coated on at 4000 rpm for 30 seconds. The first layer is cured on a hot plate at 100°C for 1 minute, exposed to 365 nm UV light for 5 minutes and again placed on the 100°C hot plate for 1 minute. Then the second layer is applied, and directly after spin coating a slab of PDMS with a monolayer of silica spheres is pressed into the soft SU8 and placed on a 100°C hot plate hot plate for 1 minute with a weight of 160 gram on top. The second layer is not cured with UV light to avoid damage to the perovskite film due to the focusing of the UV light by the spheres.

Sphere monolayer self-assembly: 5 μm diameter silica spheres in aqueous solution (Sigma Aldrich 44054-5ML-F) are dried to a powder on a hot plate. PDMS is mixed in a 1:9 ratio, poured into a petridish and cured in the oven at 80°C for 3 hours. The cured PDMS is peeled off and cut into pieces of ca 15x15 mm. Some dry sphere powder is applied to one piece of PDMS and another piece is rubbed across with light finger pressure to spread out the spheres and form a monolayer.

Absorption measurements: Absorption at short wavelength is determined with high accuracy using an integrating sphere setup described before,[118] using 600 short pass filters to remove any PL from the signals. The full absorption spectrum up to 800 nm wavelength is measured with transmission and reflection measurements with a Thorlabs Thorlabs amplified Si detector (PDA100A) for the reflection signal and a passive Newport 818-UV photodetector for the transmitted signal, both read out by Stanford Research Systems SR830 lock-in amplifiers. The sample is excited using a supercontinuum laser (NKT Fianium FIU 15) and acousto-optical tunable filters to select ca 2 nm bandwidth light in steps of 10 nm from 400 to 800 nm.

Fourier measurements: Fourier images were taken in a home built Fourier microscope with NA of 0.85. The sample is excited with 532 nm laser light in full field illumination, resulting in a spot size of ca 60 μm diameter. Fourier images are collected with a 0.85 NA objective and recorded with a Andor Clara CCD camera.

5.5 Supporting Information

5.5.1 Simulations

Optical simulations

Material properties The optical properties of perovskite were implemented in Lumerical FDTD as real and imaginary refractive index values (n and k values). The values used are adjusted from experimental data on $MaPbI_3$ film.[157] These were converted to mixed iodide/bromide perovskite according to,[158] which was shown to be a valid method in.[159] The data were shifted by first converting the imaginary part of the refractive index k to absorption coefficient, using $k = \frac{\alpha\lambda}{4\pi}$, then shift λ by 45 nm and 135 nm for respectively the 80:20 I:Br and the 50:50 I:Br phase, and then converting back to k. For the real part of the refractive index n the spectrum is simply shifted by the above mentioned values. For accurately simulating the emissivity at the bandgap, an Urbach tail is added to the experimental data with an Urbach energy of 18 meV, which was added to the absorption coefficient before converting this back to k. Lumerical FDTD uses a fitting model with polynomials for experimental refractive index data. Close to the bandgap, when the k values approach and eventually become zero, the polynomials often result in bad fitting. To accurately simulate absorption in this region, simulations were split up in small wavelength ranges, each time fitting only to a small part of the data to ensure accurate fitting. The simulation over the full solar spectrum, ranging from 300 to 825 nm was split up in 9 simulations. At short wavelengths, far away from the bandgap of either of the two phases, 5 nm wavelength step size was used, while around the bandgaps a 1 nm step size was used to accurately track changes in the Urbach tail.

Simulation lay-out The FDTD simulation is built up as follows, from bottom to top: Aluminum back side (Al (Aluminium) - Palik), that extends into the metal boundary at the lower z-limit, 500 nm of perovskite with 50:50 I:Br ratio with n and k values as described above, if applicable: vertical cylinders with 600 nm diameter throughout the perovskite film with 80:20 I:Br ratio, 50 nm of ITO (n and k values from[160]), 80 nm of SU8 (n=1.5525+0.00629*λ^{-2}+0.0004*λ^{-4}, k=0), if applicable 5 μm diameter silica spheres (SiO2 (Glass) - Palik) in a background refractive index of 1. Top z boundary is PML, x and y boundaries are Anti-Symmetric and Symmetric, respectively, excitation with plane wave in downward z-direction. The simulation area is 5 μm by 8.66 μm, which is the smallest unit cell for an hexagonal close packed array, with one sphere at the center, and a sphere at each corner, resulting in a total to two spheres in the unit cell.

ELECTRICAL SIMULATIONS

For the electrical simulations in Lumerical Device - CHARGE, the same unit cell is used, but without the SU8 and silica spheres, since these do not contribute to the electrical properties. Their effects are included in the optical generation profile, which is imported from the optical simulations. Hole and electron transport layers of 15 nm of NiO_x and ZnO respectively are used in the electrical simulations. The material properties used are summarized in table 5.4. For the aluminum back contact the default ‘Al (Aluminum) - CRC’ material in Lumerical Device is used.

	50:50 I:Br	80:20 I:Br	ZnO	NiO_x	ITO
Bandgap (eV)	1.94	1.7	3.2	3.75	3.5
DC permittivity	10	10	8.1	10.7	8.9
Work function (eV)	4.88	4.75	5.68	3.98	4.6
m_n	0.229	0.229	0.318	1.076	0.17
m_p	0.289	0.289	0.117	0.801	0.8
SRH carrier lifetime [s]	1.3e-6	1.3e-6	1.3e-8	1.3e-8	-
Surface recombination velocity [cm/s]	20	20	-	-	-
Doping	1e11	1e11	1e19	1e15	-

Table 5.4: Material properties as used in Lumerical Device CHARGE simulations. Perovskite, ZnO and NiO_x properties from,[161] with adjustments in perovskite bandgap and work function to account for mixed phases. m_n and m_p are the effective mass of electrons and holes.

5.5.2 SUPPLEMENTARY FIGURES

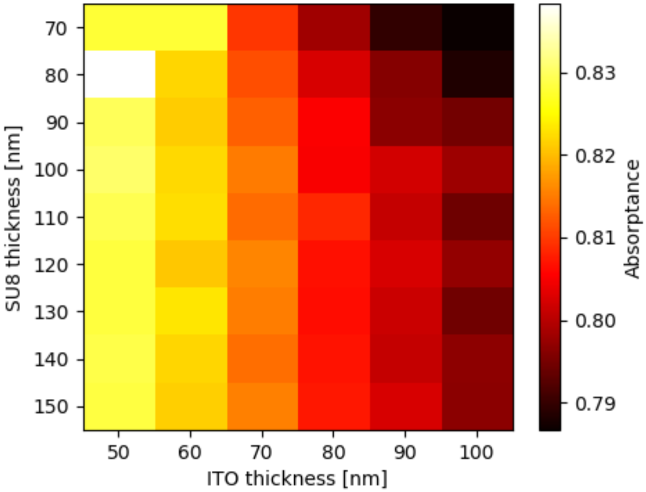

Figure 5.5: SU8 and ITO thickness optimization for maximizing absorption. The average absorptance at 500 and 600 nm was determined while sweeping the ITO thickness from the minimum value for good conductivity of 50 nm to 100 nm, and sweeping the SU8 thickness from 70 to 150 nm, both in steps of 10 nm. The highest absorptance was found for 50 nm ITO and 80 nm SU8 thickness.

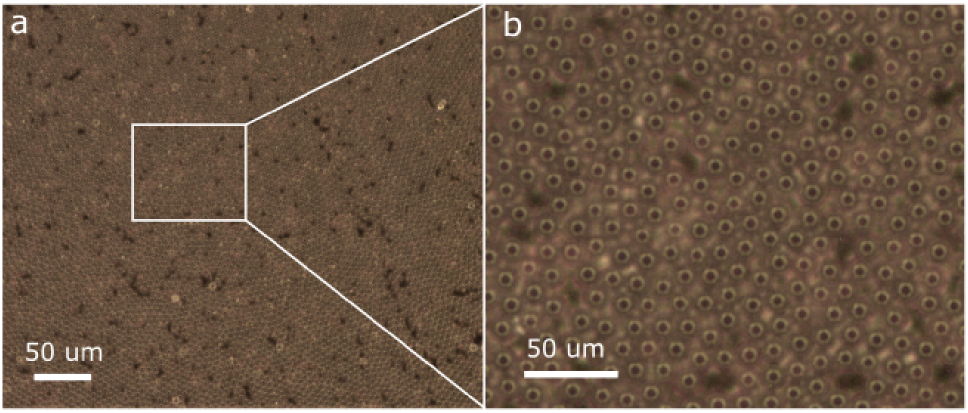

Figure 5.6: Optical microscope image of a self-assembled monolayer of 5 μm silica spheres after transfer to the perovskite film by pressing the spheres into soft SU8 photoresist. a) Overview of large area monolayer. b) Zoom of a.

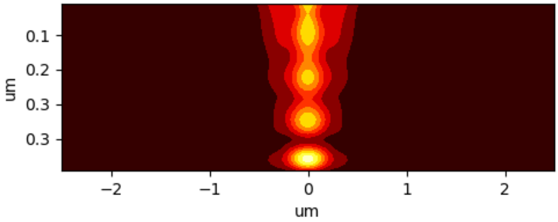

Figure 5.7: Hotspot in low bandgap perovskite film underneath a 5 μm silica sphere under solar illumination.

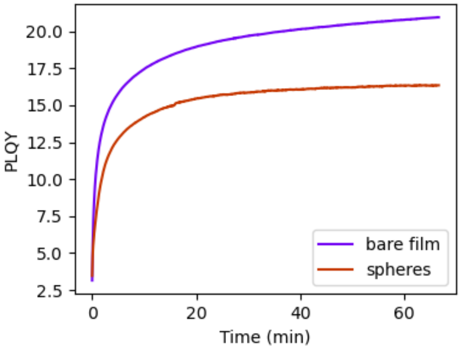

Figure 5.8: The PLQY keeps increasing over prolonged light excitation with full field illumination.

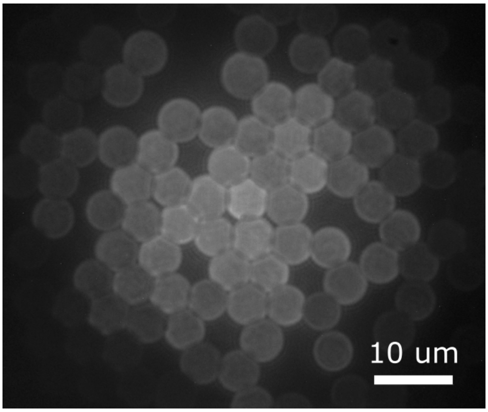

Figure 5.9: Real space image of the microspheres in full field laser illumination. Ca 50 microspheres are illuminated.

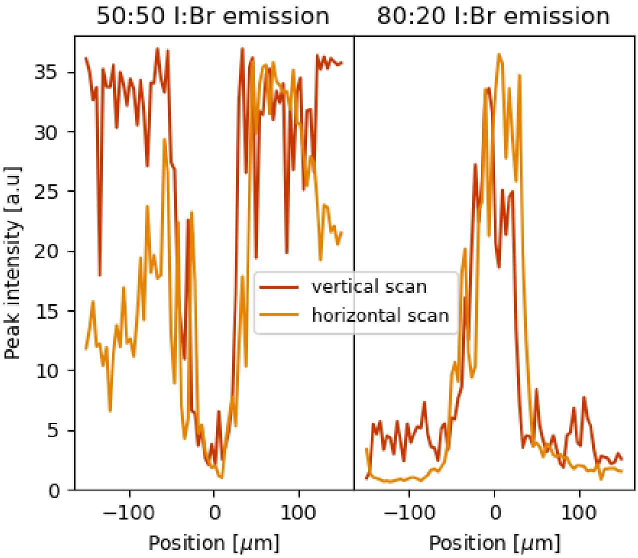

Figure 5.10: Emission intensity of the two phases. First the center is illuminated with full field illumination, such that phase segregation occurs. Consecutively, emission spectra are collected while scanning in a vertical and horizontal line across the illuminated area. In the illuminated region, the emission from the mixed 50:50 I:Br almost completely disappears, indicating that the whole area has segregated into the 80:20 I:Br phase.

6

UNLOCKING HIGHER POWER EFFICIENCIES IN LUMINESCENT SOLAR CONCENTRATORS THROUGH ANISOTROPIC LUMINOPHORE EMISSION

The luminescent solar concentrator offers a potential pathway for achieving low-cost, fixed-tilt light concentration. Despite decades of research, conversion efficiency for luminescent concentrator modules has fallen far short of that achievable by geometric concentrators. However, recent advances in anisotropically-emitting nanophotonic structures could enable a significant step forward in efficiency. Here, we employ Monte Carlo ray-trace modeling to evaluate the conversion efficiency for anisotropic luminophore emission as a function of photoluminescence quantum yield, waveguide concentration, and geometric gain. By spanning the full LSC parameter space, we define a roadmap towards high LSC conversion efficiency. An analytical function is derived for the dark radiative current of an LSC to calculate the conversion efficiency from ray-tracing results. We show that luminescent concentrator conversion efficiency can be increased from the current record value of 7.1% to 9.6% by incorporating anisotropy. We provide design parameters for optimized luminescent solar concentrators with practical geometrical gains of 10. Using luminophores with strongly anisotropic emission and high (99%) quantum yield, we conclude that conversion efficiencies beyond 28% are achievable. This analysis reveals that for high luminescent solar concentrator performance, waveguide losses are as important as the luminophore quantum yield.

6.1 Introduction

Despite outpacing other forms of renewable energy,[162] solar photovoltaics still occupies a limited fraction of the worldwide energy portfolio—with just 580 TWh of solar electricity generated in 2019 compared to over 23,000 TWh of total electricity consumed.[163] Given the disparity between solar generation and worldwide consumption, tremendous research effort is underway to spur further adoption. Building-integrated photovoltaics is one such area, and aims to incorporate solar generation into residential and commercial building components (e.g., envelopes,[164,165,166] roofs[167] windows,[168,169,170] greenhouses.[171,172,173,174,175] The decreasing cost of solar modules and the proportionate increase in balance of system and soft costs[176] motivates integration of photovoltaics into buildings to minimize overall system and installation expenses.[165]

First introduced in the mid-twentieth century for scintillation counting applications,[177] the luminescent solar concentrator (LSC) offers unique advantages for building-integrated devices. An LSC consists of a dielectric waveguide containing suspended luminophore particles at a given concentration (i.e., optical density). Upon illumination of the waveguide top surface, the embedded luminophores absorb photons within their absorption band and re-emit energetically down-shifted photoluminescence (PL) at a radiative efficiency given by the luminophore PL quantum yield (PLQY). The spectral and angular PL emission profiles of the luminophore, along with the index of refraction contrast between the waveguide and surrounding media (often polymer and air, respectively), determine the amount of PL trapped in the waveguide through total internal reflection (TIR). For photovoltaic applications, solar cells can be optically coupled to the waveguide edges. Figure 6.1a illustrates the fundamental operating principles and components of a general, single-edged photovoltaic LSC device.

Thermodynamically, an LSC holds distinct advantages over both traditional geometric concentrator modules as well as conventional, nonconcentrating photovoltaic systems. As has been shown, the Stokes shift (spectral separation between luminophore absorption and emission) sets the maximum achievable concentration limit.[178] Unlike traditional passive concentrators whose limit depends upon the acceptance angle,[179] LSCs can absorb and concentrate off-angle and diffuse irradiance.[180,181] Consequently, LSC photovoltaic cells maintain lower operating temperatures than both geometric concentrators and non-concentrated, flatplate photovoltaics owing to decreased thermalization of high-energy photogenerated excitons of the collection cell.[182]

Economically, LSCs offer potential system-levelcost reductions owing to the flexibility of these devices into building-integrated photovoltaic designs.[183,184] The ratio of top surface waveguide area to the net solar cell area, termed the geometric gain (GG), sets the amount of the photovoltaic material required per LSC module. The optical density of luminophores suspended within the waveguide, as well as the luminophore absorption and emission spectral profiles, determines the visible transparency and color tinting of the LSC.[185] Thus, LSCs can be aesthetically tuned to meet the need(s) of building-integrated photovoltaic designs. The LSC aesthetic tunability also compels such devices for myriad façade components and end-uses.[186,187] Beyond such applications, previous studies have also investigated routes toward high-efficiency photovoltaic applications as a promising area for LSC research—exploring, for example, LSC–LSC[70] and LSC–Si[69,188,189,190] tandem structures.

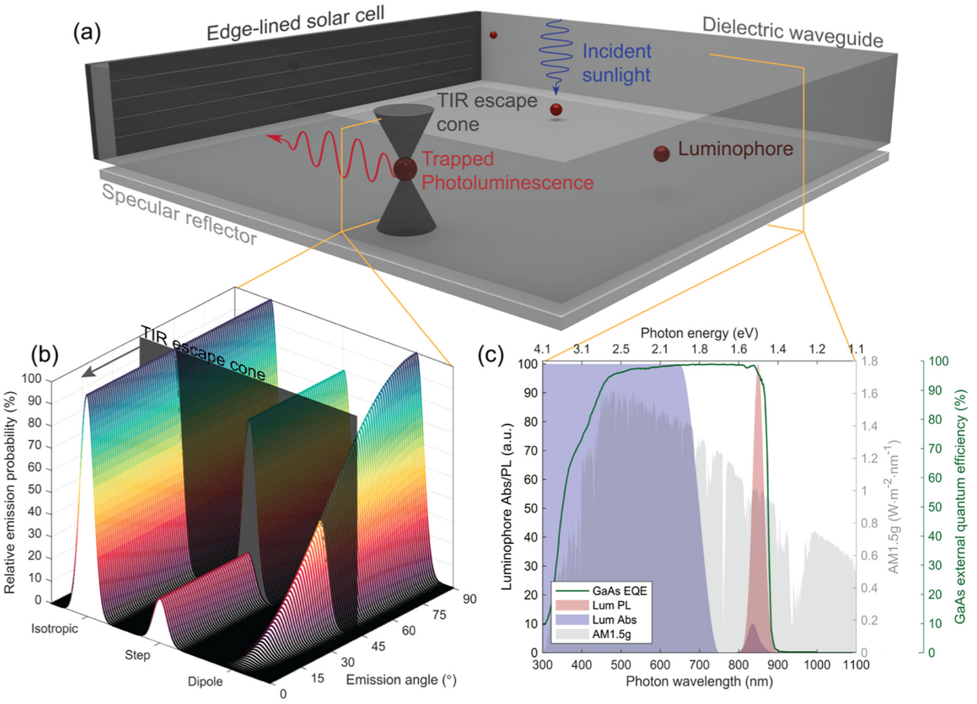

Figure 6.1: (a) 3D rendering of a rectangular luminescent solar concentrator coupled to an edge-lined solar PV cell. Incident sunlight strikes embedded luminophores within the optical, dielectric waveguide where, given the luminophore radiative efficiency (i.e., PLQY), down-shifted PL is emitted. Given the waveguide's index of refraction, a portion of PL emits into the TIR escape cone, while a portion occupies TIR angles. In this work, we assume a waveguide with a broadband specular reflector cladding the bottom surface, as shown here. (b) Three examples of luminophore PL profiles (arbitrary wavelength) given the emission angle relative to the top waveguide surface normal. Here, we show the relative PL emission probability for the case of an isotropic luminophore with equal probability of PL across all angles; a step function like luminophore with a probability, Pesc, of emitting into the escape cone and a complementary probability, P_{TIR}, of emitting into TIR angles; and a dipole emission pattern showing a continuous anisotropic profile. (c) Spectral profile that we assume for this model, where we assume a luminophore with an absorption edge up to 700 nm (left y-axis), a PL center of 800 nm with an FWHM of 20 nm (left y-axis), and a GaAs cell whose external quantum efficiency (EQE) we show in green (far right y-axis). We plot against the AM1.5G spectrum (right y-axis) for reference.

The concentration mechanism for an LSC introduces a large number of design and performance parameters.[191] Among these include the luminophore PLQY, optical density of luminophores, GG of the LSC system, Stokes shift of the luminophore absorption/PL profiles, trapping efficiency of the emitted PL, reabsorption probability by the luminophore species, attenuation and bulk/surface scattering by the host waveguide, and the quantum efficiency of the photovoltaic cell collector.[192] Previous studies have highlighted the most important parameters for LSC optical and conversion efficiency; PLQY, PL trapping, optical density, and GG are observed to be highly influential for a given LSC and luminophore system type.[193, 194, 195, 196, 197] While some parameters need to be maximized (e.g., PLQY) or minimized (e.g., attenuation in the waveguide), others attain optimal values that strongly depend on the entire LSC design, complicating the process (e.g., optical density, GG).[198, 199]

In addition, there exist numerous pathways for photon loss intrinsic to the LSC design. Consequently, the single-junction LSC conversion efficiency remains limited to below 10%, with the current record achieving 7.1% under 1 sun illumination.[200]

Among the many parameters that can be tuned for highly efficient LSCs, the methods by which the waveguide layer traps and guides PL to the optically coupled solar cells remain an active field of research. Common rectangular LSC waveguide materials (e.g., polymer or glass) trap under 75% of the isotropically emitted luminescence radiation by TIR.[177,201] To decrease the waveguide losses through the escape cone, methods for trapping have addressed either cladding the top/bottom LSC surfaces with Bragg mirrors to reflect a portion of the PL emitted within the escape cone[202,203,204] or employing luminophore materials or structures that preferentially emit outside of the escape cone.[205,206,207,208,209,210,211,212] This significant body of research has detailed the effects of LSC parameters on cladding losses (i.e., external dichroic mirrors and photonic crystal structures) as well as anisotropically emitting luminophores. With recent advances in the angular control of luminescence radiation using nanophotonic structures, however, this has become a key focus area for research in LSCs.[56] Together with semiconductor quantum dots whose emission efficiencies can extend beyond 99%,[113] nanophotonic-luminophore designs open new directions for improved LSC efficiency. Unlike previous works, here we quantify the effects of luminophore anisotropic emission for a variety of profiles, for a common edge-lined LSC structure, while covarying the device parameters of interest to unveil the pathway to achieving high power conversion efficiency devices.

In this work, we compare the effects of several types of anisotropic emitters on LSC conversion efficiency. Figure 6.1b illustrates different emission patterns for an arbitrary PL spectrum. An isotropic emitter has an equal probability of emission into any angle, as shown on the left of Figure 6.1b. To quantify the effects of angular emission, we model luminophores with a step-function anisotropic profile, as illustrated in the center of Figure 6.1b. While useful in its analysis, such a step-function emission profile is unphysical. As such, we next discuss and analyze the consequences of more realistic, continuous emission probabilities, like that of the nanophotonic dipole emitter shown on the right-hand side of Figure 6.1b. We assume that the embedded luminophore particles do not anisotropically scatter incident photons below the absorption bandgap. Thus, Figure 6.1b displays the PL profiles of example luminophores for photons with energies greater or equal to the absorption bandgap, as given by Figure 6.1c. Further, unlike the absorption cross section of certain luminescent dyes that depend on their physical orientation and the angle of incidence, we assume isotropically absorbing luminophores regardless of the tilt angle within the waveguide (e.g., two-dimensional transition-metal dichalcogenide heterobilayer absorption/emission[213] or all-dielectric resonant nanostructures coupled to quantum emitters[214,215]).

We quantify the effects of luminophore PL anisotropy in a rectangular planar LSC waveguide, employing four high-efficiency GaAs cells optically coupled to each edge of a polymer matrix. We apply an experimentally validated Monte Carlo ray-trace model to uncover the conversion efficiency performance for such an LSC employing an ideal luminophore. By evaluating the performance of the LSC with respect to power conversion efficiency (rather than, for example, concentration factor), we ensure area-agnostic comparisons across devices of differing GGs. Figure 6.1c highlights the external quantum efficiency

(EQE) of the GaAs cell, the ideal absorption/PL spectral profiles of the luminophore, and the simulated AM1.5G irradiance assumed to strike the device at normal incidence. We include a thorough discussion of the Monte Carlo ray-trace computational method and the implementation of luminophore anisotropy within such a model. In addition, we provide a thorough physical picture of the radiative limit for such LSCs. We discuss the impact of luminophore anisotropy on LSC performance and its covariation with PLQY, GG, and optical density. We then model the impact of luminophore PL anisotropy on the current record LSC. Finally, we end with a detailed thermodynamic breakdown of the loss mechanisms for a variety of LSCs with anisotropically emitting luminophores.

6.2 RESULTS AND DISCUSSION

Here, we discuss the effects of anisotropy on conversion efficiency using Monte Carlo modeling. To unveil the conversion efficiency performance with respect to luminophore anisotropy, we begin with a discussion on the LSC system detailed balance, quantifying the dark radiative current thermodynamics. Next, to consider how LSC parameters for anisotropic luminophores affect conversion efficiency, we simultaneously vary the geometric gain from 1 to 100, luminophore optical density at 750 nm from 0 to 3, and the luminophore quantum yield from 75 to 100%. We introduce the case of a steplike emission pattern and its effect on this conversion efficiency, where we vary the luminescence fraction trapped in TIR modes continuously from 75 to 100%. Finally, we analyze the LSC performance given dipole and forward emitter anisotropy profiles.

6.2.1 THERMODYNAMICS OF ANISOTROPIC LSC DEVICES

To elucidate the conversion efficiency behavior of an arbitrary LSC device, we must quantify both the resulting short-circuit current (J_{sc}) and open circuit voltage (V_{oc}). We can model the resulting short-circuit current density given the high accuracy Monte Carlo ray-trace methods, as described in the Computational Methods section. However, to calculate the open circuit voltage, we first define the radiative limit case and subsequently include the GaAs cell external radiative efficiency nonidealities.[216, 217] Beginning with the radiative limit equation,[22] we have

$$V_{oc}^{rad} = \frac{kT}{q} \ln\left(\frac{J_{sc}}{J_0^{rad}}\right) \tag{6.1}$$

where k, q, and T are the Boltzmann constant, electronic charge constant, and temperature of the LSC (assumed to be at 300 K), respectively. As stated, J_{sc} gives the total exciton generation under direct illumination by the sun (i.e., the short-circuit current), while J_0^{rad} gives the exciton generation under no direct illumination but instead in the ambient, Blackbody background at temperature T for purely radiative recombination and generation.

In thermodynamic equilibrium, the total absorption by the LSC system from the Blackbody background (J_0^{abs}) must equal the total emission by the LSC into free space (J_0^{emit}), as illustrated in Figure 6.2a. Therefore, when solving for J_0, we can choose either the absorption or emission picture.[218] Let us assume that X% of luminophore PL and Y% of GaAs PL enter the escape cone and radiate into free space. Here, X% can be calculated via the specific luminophore radiance profile—as described later in this study—and Y% by the waveguide index of refraction,[177] assumed here to be a constant 1.49 across PL wavelengths (Y% ≅ 25%). Starting with the emission picture, we can distinguish the resulting LSC dark current into the contribution from the luminophore ($J_0^{emit,lum}$) and GaAs cell ($J_0^{emit,pv}$) into free space

$$J_0^{rad} = J_0^{emit} = J_0^{emit,lum} + J_0^{emit,pv} \tag{6.2}$$

Figure 6.2a-c conceptually illustrates this dark current term in both the emission and absorption settings. Given the X% and Y% fractions, we can rewrite eq 6.2 to include the total amount of the luminophore and cell emission rather than emission solely into the escape cone and thereby back into free space. Doing so, we have

$$J_0^{rad} = X\% \cdot J_{total}^{emit,lum} + Y\% \cdot J_{total}^{emit,pv}, \tag{6.3}$$

where $J_{total}^{emit,lum}$ and $J_{total}^{emit,pv}$ give the total amount of PL by the luminophores and GaAs cells, respectively. Given that total absorption into the luminophores or GaAs cells must equal total emission out of the luminophores or GaAs cells, respectively, we can rewrite eq 6.3 in the context of the absorption profiles, as shown by Figure 6.1c

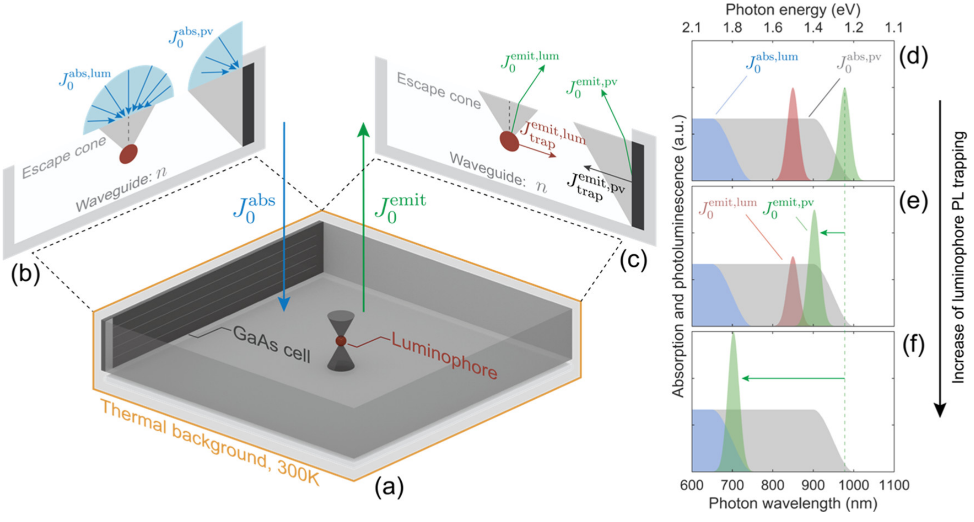

Figure 6.2: Conceptualization of the LSC system when in thermal equilibrium with the ambient Blackbody background at 300 K. In this case, we know that absorption into and emission out of the LSC system must be equal as shown in (a). Therefore, we can choose to analyze the system in either the absorption (b) or emission (c) pictures. (d), (e), and (f) conceptually illustrate the spectral consequence to outgoing, free space PL via the GaAs cell as the luminophore PL trapping increases. (d) depicts the case of no photoluminescence trapping, where the luminophore absorption (blue) and luminescence (red) are shown to be separated by the Stokes shift energy, and there is some spectral width to the cell PL (green) for an arbitrary cell absorption (gray). (e) and (f) show how varying the amount of luminophore PL trapping affects the spectral location of the cell emission?where, as shown in (f), complete trapping yields the highest open circuit voltage condition, which is given by the luminophore absorption bandgap.

$$J_0^{rad} = X\% \cdot J_{total}^{abs,lum} + Y\% \cdot J_{total}^{abs,pv}. \tag{6.4}$$

As shown in Figure 6.2b, we know that the total GaAs cell absorption ($J_{total}^{abs,pv}$) must be a sum of both the trapped luminophore PL (i.e., 1 - X%) and photons entering the waveguide and striking the edge-lined cell directly from the Blackbody spectrum at ambient temperature, T—where the GG gives this amount of incident light reaching the edge-lined cell. We assume, given the absorption profile of the luminophores and the fact that GaAs PLQYs are significantly lower than that of the luminophores, that the TIR-trapped GaAs PL contributes a negligible amount of the total absorption of the luminophores. Therefore, we can write

$$J_0^{rad} = X\% \cdot J_{total}^{abs,lum} + Y\% \cdot ((1 - X\%) \cdot J_{total}^{abs,lum} + \frac{1}{GG} \cdot J_0^{abs,pv}). \tag{6.5}$$

Where, as shown in eq 6.5, we distinguish between $J_{total}^{abs,lum}$) and $J_0^{abs,pv}$, where the former gives the total amount of absorption by the luminophore species—which must equal the total amount of PL—while the latter indicates the amount of irradiance absorbed by the GaAs cells exclusively from free space, Blackbody radiation and not by luminophore PL. We can now define each of these terms given our known absorption profiles and the Planck spectrum

$$\begin{aligned} J_0^{rad} = {} & [X\% + Y\%(1 - X\%)] \cdot \int_\omega \int_\Omega A_{lum}(\omega) \cdot \Phi_{bb}(\omega) d\Omega d\omega \\ & + Y\% \cdot \frac{1}{GG} \cdot \int_\omega \int_\Omega A_{pv}(\omega) \cdot \Phi_{bb}(\omega) d\Omega d\omega), \end{aligned} \tag{6.6}$$

where A_{lum} and A_{pv} are the absorption profiles of the luminophore and GaAs cell, respectively, Φ_{bb} is the Planck spectra at 300 K, ω is the frequency of the photon, and Ω is the solid angle (2π steradians for this case of background radiation). With this expression and our simulated photocurrent term from the Monte Carlo ray-trace model, we can fully define the LSC open circuit voltage in the radiative limit. Given eq 6.6, we can conceptually understand the effect of luminescence trapping within a waveguide in terms of spectral shifting of the GaAs cell, highlighted by Figure 6.2d-f. In the limit where the geometric gain is large and the luminophores exhibit perfect PL trapping within the waveguide (i.e., X% = 0), the dark radiative current is given by that of the luminophore absorption profile (that is, electronic bandgap). In this limit, the LSC open circuit voltage is limited by the bandgap of the luminophore and not the photovoltaic cell.

As shown in Figure 6.2d, if we assume general luminophore and GaAs cell absorption and emission profiles—where the luminophore absorption and PL are separated by a certain Stokes shift energy—we can qualitatively observe the impact of trapping on PL of the GaAs cell. As seen in Figure 6.2e, partial trapping will yield blue-shifted cell PL, while full trapping (Figure 6.2f) shows how the effective cell open circuit voltage saturates to the luminophore bandgap for the limit of high GG. To include nonradiative effects of the GaAs cell, we apply an explicit form of the GaAs external radiative efficiency, as well as approximate fill factor calculations, as described in the Computational Methods section.

6.2.2 EMITTERS WITH STEPLIKE ANISOTROPY

To begin, we assume a steplike luminescence angular emission distribution, as shown in Figure 6.3a,b. We vary the luminescence intensity fraction, P_{TIR}, emitted at TIR angles, and assume this angular distribution to be symmetric about the z-axis (i.e., normal to the waveguide plane). By representing the luminophore anisotropy with a single variable, we can uncover the relationship between anisotropic emission, GG, optical density, and PLQY. First, we vary the luminescence quantum yield and P_{TIR} of the luminophores, assuming a high optical density of 3, such that 99.9% of the incident light is absorbed in a single pass and a modest geometric gain of 20. As shown in Figure 6.3c, the optimal conversion efficiency occurs for unity PLQY and P_{TIR}, where for this luminophore/cell system, we observe a global maximum of approximately 29% under 1 sun illumination—approaching the detailed balance limit with respect to the luminophore absorption and reabsorption bandgaps, including nonradiative effects within the GaAs cell. In contrast, the isotropic case (P_{TIR} = 75%) falls short of 5%.

Within Figure 6.3c, we plot contours of the product (PLQY,P_{TIR}) for constant values of 0.60, 0.70, 0.80, 0.90, 0.95, and 0.99, finding qualitative agreement between these contours and the simulation results. This agreement can be understood from the fact that the product of luminescence quantum yield and P_{TIR} sets the probability that a trapped photon survives an absorption event by a luminophore and is guided to the solar cell. Whether the photon is lost through nonradiative recombination (for low PLQY) or by escaping the waveguide (low P_{TIR}) is irrelevant for the resulting efficiency. Significantly, increasing P_{TIR} is as important as increasing the luminescence quantum yield.

To examine the relationship between PL trapping, PLQY, GG, and optical density, Figure 6.3d,e shows stacked contour maps for TIR-limited and ideal trapping cases, respectively. As seen in Figure 6.3d, there exists a global optimum optical density for all PLQY and GG values of approximately 0.50 for PLQYs between 75 and 100%. As GG increases for PLQYs at or below 99%, we observe a steep and monotonically decreasing conversion efficiency at constant optical density. However, importantly, we find that for ideal emitters (near-unity PLQY and unity trapping) lower GG limits the maximum concentration of the system thereby constraining the open circuit voltage to the GaAs electronic bandgap. As the GG increases for this high PLQY and trapping cases, the system bandgap tends toward the luminophore absorption bandgap yielding higher overall performance.

We find a similar trend with a global optimum optical density near 1.0 for cases where the PLQY falls below 95%. However, for higher PLQYs, we observe a shift in maximum conversion efficiency with respect to optical density—in the case of unity PLQY, higher optical density yields a higher conversion efficiency. Only in the case of unity trapping and unity PLQY do we observe that conversion efficiencies remain nearly constant with increasing GG. Figure 6.3c,e demonstrates the importance of achieving both near-unity PLQY and PL trapping.

To more closely quantify the role of optical density and GG, Figure 6.4a,b examines how various (PLQY, P_{TIR}) pairs impact conversion efficiency. As seen in Figure 6.4a, the optimal luminophore optical density depends strongly upon the waveguide trapping and luminophore radiative efficiency. Since this density determines both the amount of absorbed sunlight as well as the amount of PL reabsorption within the waveguide, a poor PLQY and P_{TIR} results in detrimental nonradiative recombination and high escape cone

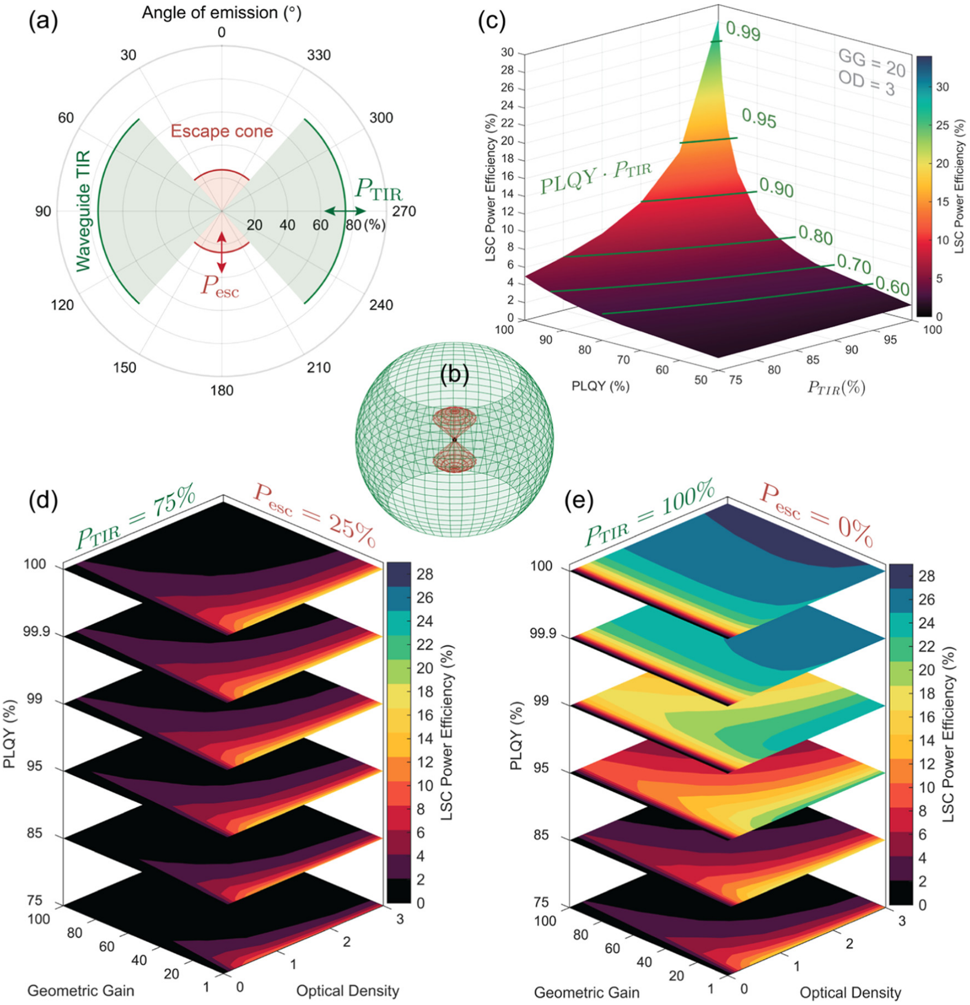

Figure 6.3: (a) Two-dimensional (2D) polar plot of the step-function emitter profile, illustrating how the TIR escape cone probability (P_{esc}) and TIR trapping probability (P_{TIR})affect the overall luminescence angle of emission probability. As shown in (c), we assume symmetry about the polar angle (i.e., about the z-axis). (b) Effects of luminophore anisotropy on the conversion efficiency of an LSC. Here, we vary the PLQY and amount of TIR emitted radiation by the luminophore, assuming a geometric gain (GG) of 20 at a waveguide optical density of 3. The analytical predictions for the waveguide efficiency (green contours) show close matching with the Monte Carlo results. (d, e) Monte Carlo ray-trace simulations for the conversion efficiency of an LSC with luminophores that emit 75% into TIR angles (i.e., anisotropic) vs 100% into TIR angles (i.e., anisotropic) as a function of GG, optical density, and PLQY.

losses for the absorbed incident and re-emitted PL photons. As the (PLQY, P_{TIR}) product increases, the drawback of reabsorption diminishes while the advantage of increased sunlight absorption remains, thereby increasing the optimal optical density. Figure 6.4b illustrates the difficulty in achieving a high conversion efficiency for the increasingly large waveguide to cell area ratios for products less than unity. In all but the ideal case, efficiency monotonically decreases with increasing GG. Even in this special case of unity PLQY and P_{TIR}, increasing the GG beyond a certain value yields higher likelihood of photoluminescence scattering inside the escape cone, resulting in lowered conversion efficiencies. For efficiencies above 15% at GGs above 10, the (PLQY, P_{TIR}) product must be greater than 85%. Having demonstrated the upper performance limits of the LSC with a steplike emission profile, we can readily observe the interplay between the various LSC parameters as well as quantify how to reach increased power conversion efficiencies. However, to understand the limitations of more experimental anisotropic profiles, we next discuss several more realistic emission patterns.

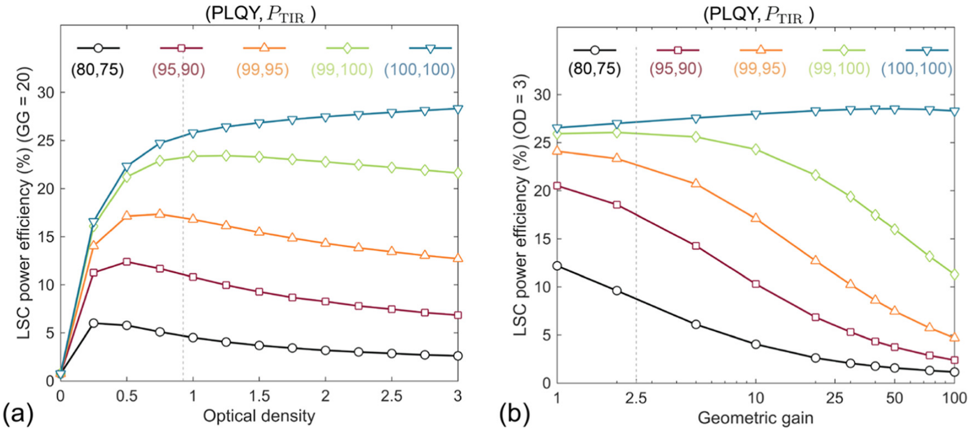

Figure 6.4: (a) LSC power efficiencies as a function of optical densities for several (PLQY, P_{TIR}) pairs, illustrating how an increase in the (PLQY, P_{TIR}) enables higher efficiencies and shifts the optimum OD to higher values. Here, we assume a GG of 20. (b) LSC power efficiencies as a function of GG for the same (PLQY, P_{TIR}) pairs as (a), assuming an OD of 3. We observe monotonically decreasing efficiencies with increasing GG, regardless of the PLQY and P_{TIR} due to the unavoidable surface and bulk scattering by the waveguide. The dotted lines in both (a) and (b) correspond to the OD and GG for the current record LSC with a conversion efficiency of 7.1%, respectively.

6.2.3 EMITTERS WITH DIPOLELIKE ANISOTROPY

For a more realistic approximation of a luminescent concentrator employing anisotropic emission, we model a system comprised of dipolelike emitters. Figure 6.5a,b illustrates the polar and 3D plots of the far-field dipole emission pattern, where we again observe symmetry about the z-axis. We find upon integration that approximately 91% of the generated luminescence is emitted into TIR angles. Varying the PLQY, GG, and optical density, we find that—similar to our previous analysis for nonunity (PLQY, P_{TIR}) pairs—there exist optimal optical densities. A PLQY of 95% and GGs below 60 yield optimal optical densities of approximately 0.67. We find maximum conversion efficiency of approximately 25% for the case of unity PLQY, an optical density of 3, and GG of 1. For a GG of 10, a geometry of practical experimental interest, the maximum conversion efficiency is approximately 18.5% for unity PLQY and an optical density of 0.75.

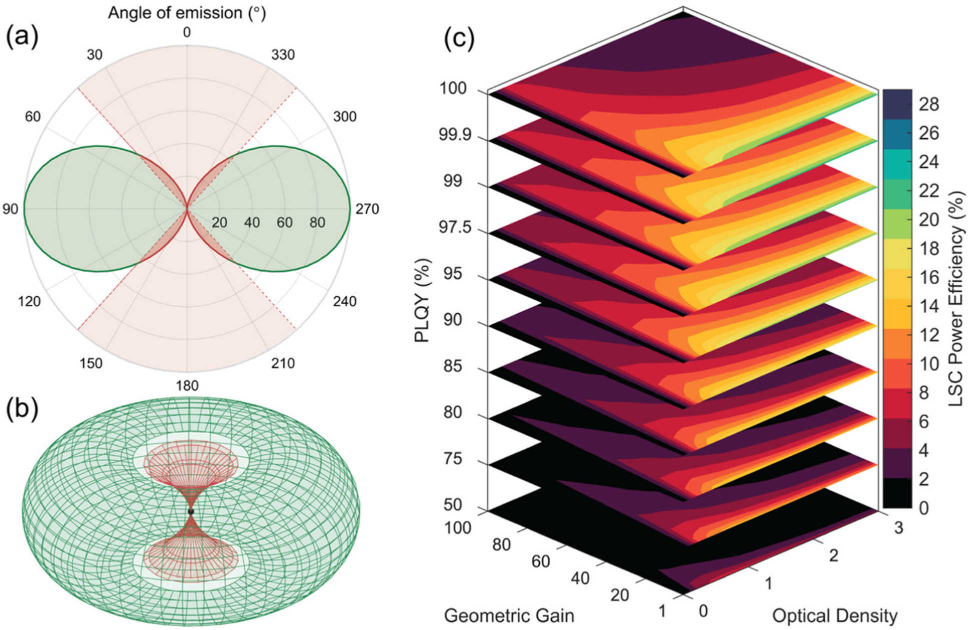

Figure 6.5: Monte Carlo ray-trace results for the dipolelike emission pattern, where (a) shows a polar 2D plot of the simulated PL profile with respect to the azimuthal angle and (b) illustrates the polar angle symmetry (i.e., about the z-axis). (c) Conversion efficiency of the LSC module with respect to GG, optical density, and PLQY.

6.2.4 Emitters with Forwardlike Anisotropy

Thus far, our analysis has employed anisotropic emitters with far-field radiation symmetric about the z-axis. We now turn attention to optical structures that exhibit strong emission in a single direction, breaking this symmetry. In the case of emission systems symmetric about the z-axis, photons perform random walks throughout the waveguide. By contrast, forward-emitting luminophores exhibit a decreased mean free path for photon propagation to the collector cells. As detailed in the Methods section, we simulate forward-emitting luminophores consisting of spherical absorbing/emitting nanoparticles embedded within a nanocone. For such a forward-emitting luminophore, Figure 6.6a-c highlights the polar radiation plot, spatial radiation profile, and nanocone structure. Integrating the luminescence intensity, we observe that approximately 88% of the intensity from such structures couples into the TIR waveguide angles—slightly less than for the dipole emitter.

As shown in Figure 6.6d, the dependence of forward emitter conversion efficiency on optical density, GG, and PLQY closely parallels that of the dipole emitter case. However, even though the forward emitter is 33% more likely to emit photons into the escape cone relative to dipole structures, we observe a maximum conversion efficiency of 24%, approximately 96% of the dipole emitter maximum. We find fewer luminescence reabsorption events for forward emitters compared to their dipole emitter counterparts, suggesting that breaking this z-axis symmetry enables shorter luminescence mean free paths within the waveguide. This shorter path almost completely compensates the increased escape cone loss. Further, we observe that for a GG of 10, the maximum conversion efficiency reaches

17.3% for the case of unity PLQY and an optical density of 0.75.

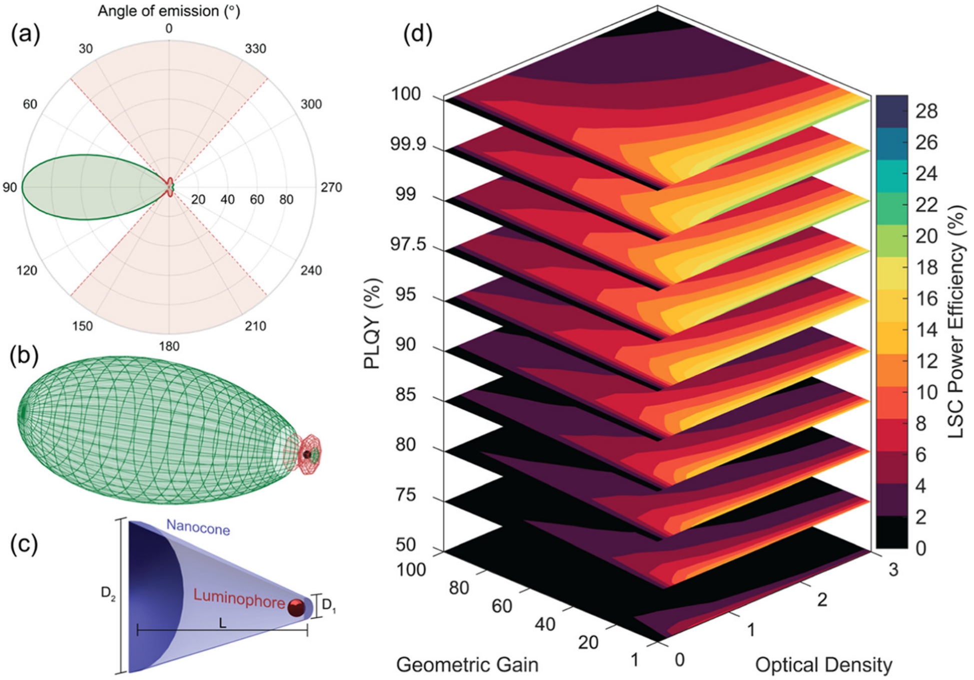

Figure 6.6: Monte Carlo ray-trace results for the forward, nanocone emission pattern, where (a) shows a polar 2D plot of the simulated PL profile with respect to the azimuthal angle and (b) illustrates the polar angle asymmetry of the forward emitter, where the structure preferentially emits into angles along a single direction of the horizontal x-axis. (c) 3D rendering of a cross section of the forward-emitting structure, consisting of the luminophore (red sphere) at the narrow end of the cone (R_2) of length L with a final, large radius of R_2. (d) Conversion efficiency of the LSC module with respect to GG, optical density, and PLQY.

6.2.5 Enhancing the efficiency of the Record LSC

While the dipole and forward emission cases correspond to physically realizable emitters, the LSC structure itself assumes certain idealities. Specifically, we thus far have assumed record GaAs PV cells coupled to ideal luminophore emitters with a narrow PL profile matched to the GaAs bandgap (as shown in Figure 6.1c). Additionally, our simulated LSC waveguide matrix assumes a constant index of refraction for generated PL. To illustrate how anisotropic emission can significantly benefit less idealized systems, we model the current record conversion efficiency LSC fabricated by Slooff et al.[219] As shown in Figure 6.7a, this device employs two luminophore species: Lumogen Red and Fluorescence Yellow dyes, with peak optical densities of 0.71 and 2.36, and luminescence quantum yields of 87 and 98%, respectively. With a square waveguide side length of 5 cm and an overall thickness of 0.50 cm, the fabricated LSC yields an overall GG of 2.5. Figure 6.7a displays the refractive index of the waveguide polymer matrix material, poly(methyl methacrylate), as well as the external quantum efficiency of the GaAs solar cell. Finally, a diffuse Lambertian-scattering back reflector is coupled to the bottom surface of the waveguide, with approximately 97% averaged reflectance at PL wavelengths.

We first simulate this record efficiency LSC and validate our model by obtaining conversion efficiencies equal to the experimental measurement. As a next step, we systematically vary the luminescence fraction emitted into TIR angles in the waveguide. As shown in Figure 6.7b, the isotropic emission case (i.e., P_{TIR} of 75%) attains the experimentally measured conversion efficiency value of 7.1% under 1 sun illumination. However, upon increasing the anisotropic luminescence fraction, we find a monotonic increase in performance up to 9.6% in the ideal case of unity P_{TIR}—a relative increase of 35%. The observed conversion efficiency enhancement resulting from luminophore anisotropy underscores the crucial role waveguide trapping plays in enabling high conversion efficiency.

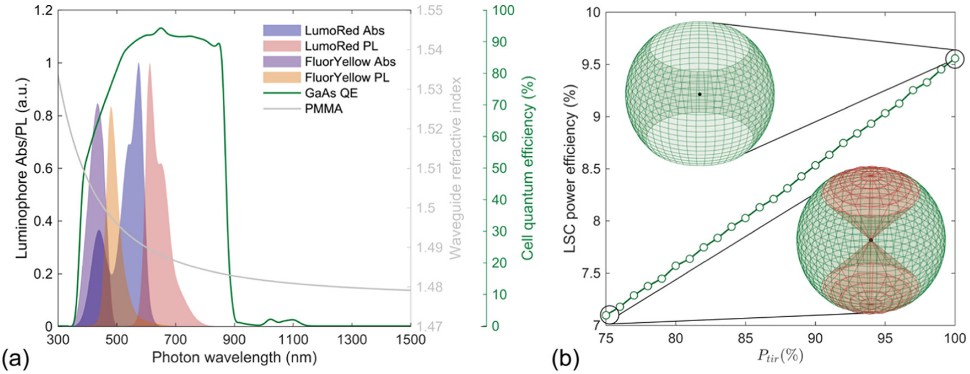

Figure 6.7: (a) Spectral characteristics of the current record LSC device, consisting of two luminophores within the waveguide (Lumogen Red, Fluorescence Yellow) (left y-axis), four edge-lined GaAs cells (cell quantum efficiency at far right y-axis), and a PMMA waveguide matrix (refractive index at right y-axis). (b) Monte Carlo ray-trace simulations showing the impact of anisotropy on the conversion efficiency for the current record device. At the isotropic limit (P_{TIR} of 75%), we observe close matching between measured and modeled efficiencies (7.1% measured and 7.096% modeled). At the anisotropic limit, power efficiencies reach 9.6%, a relative increase of approximately 35%.

6.2.6 LOSS MECHANISMS WITHIN ANISOTROPIC LSCs.

As discussed in the Methods section, we track photons collected as well as photons lost. For the luminescent concentrator, we categorize losses into five thermodynamic mechanisms. Figure 6.8a-c illustrates these losses as a function of the luminophore optical density at an LSC GG of 20, assuming PLQY of 95%. For each of the three emitter types (step, dipole, and forward), losses can be understood as either: (i) nonabsorbed incident photons, either due to sub-bandgap photon energy or low luminophore optical density; (ii) thermalization, i.e., energetic relaxation of photogenerated excitons to the luminophore bandgap energy; (iii) waveguide escape cone loss; (iv) subunity PLQY loss; and (v) loss from the photovoltaic cell itself, owing to thermalization from the luminophore emission energy to the cell bandgap, subunity collection efficiencies (i.e., EQE), fill factor, and cell contact resistance.

Figure 6.8a-c illustrates the trade-off between optical density and maximum conversion efficiency (black). Although a higher optical density minimizes the nonabsorbed incident light (blue), waveguide escape cone loss (yellow) and luminophore nonradiative recombination (orange) adversely affect the overall performance for the dipole and forward emitters. For the perfect step emitter, we observe that increased luminophore optical density yields substantially higher amounts of luminophore nonradiative recombination (orange). As expected, we observe lower escape cone loss in the dipole emitter case compared to that of the forward emitter. However, the forward emitter loses comparatively less power through luminophore nonradiative recombination compared to the dipole case given shorter mean free PL path lengths, as previously discussed.

Figure 6.8d compares four nonideal systems to an ideal case of unity PLQY and P_{TIR}, a high optical density of 3, and a GG of 20 (yielding a maximum conversion efficiency of approximately 29%). For isotropic emission (i.e., P_{TIR} of 75%) at a PLQY of 95%, the dominant loss mechanism is PL coupling into the escape cone. We also observe that for dipole, forward, or perfect step emission and PLQY of 95%, the primary loss mechanism is luminophore nonradiative recombination. In the ideal case of complete PL trapping and perfect luminophore radiative efficiency, the LSC conversion efficiency reaches the detailed balance limit of a photovoltaic system whose bandgap is given by the luminophore absorption spectra rather than the GaAs bandgap. This can be understood given that incident light with energies greater than the bandgap of the cell, but less than the luminophore absorption edge, will not be absorbed by either the luminophore or waveguide matrix—assuming a dielectric waveguide with an arbitrarily large bandgap (i.e., insulator). As demonstrated by previous studies,[220, 221] LSCs can retain the detailed balance limit only if this condition holds where the dark radiative saturation current is not scaled with the short-circuit current.

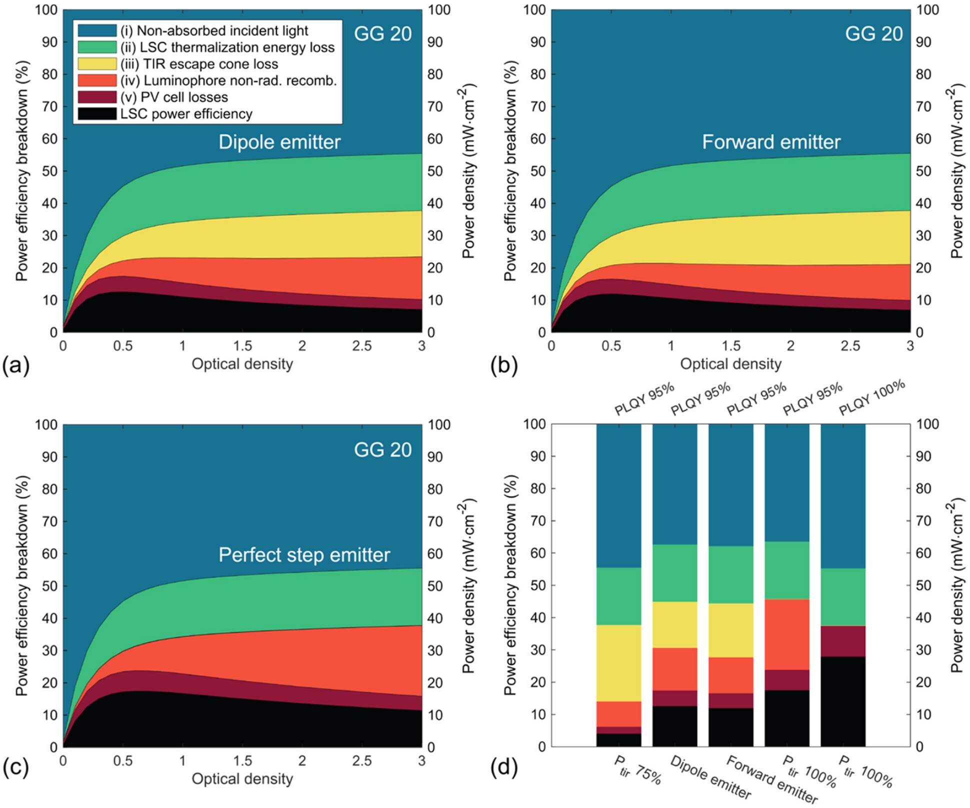

Figure 6.8: Overall conversion efficiency loss mechanisms of an LSC with respect to the optical density of the luminophores within the optical waveguide for the case of the dipole emitter (a), forward emitter (b), and perfect anisotropic step emitter (c). (a), (b), and (c) assume a PLQY of 95%. Here, we define the losses as (i) incident irradiance not absorbed by the LSC, limited by both the absorption spectrum of the luminophore and, for lower optical densities, the amount of in-band luminophore absorption; (ii) LSC thermalization energy loss, owing to the thermalization of photogenerated excitons within the luminophore that relax to the PL band; (iii) TIR escape cone loss of the PL, which can result from emitted PL coupling into the cone from an emission event or a scattering event by the waveguide; (iv) luminophore nonradiative recombination of photogenerated excitons given nonunity PLQYs; and (v) PV cell losses, which include parasitic absorption, given the limited internal quantum efficiency of the coupled cell material and thermalization from the PL emission wavelength to the bandgap of the cell. (d) Comparison of five cases at optimal OD given the emitter and GG of 20 for (from left to right): a PLQY of 95% and TIR-limited PL trapping, the dipole emitter at 95% PLQY, the forward emitter at 95% PLQY, a PLQY of 95% and perfect PL trapping, and the upper performance limit of unity PLQY and perfect PL trapping.

6.3 Conclusions and future work

In this work, we investigate the role that anisotropy plays in improving LSC conversion efficiency. Through Monte Carlo simulations, we illustrate the importance of maximizing the waveguide trapping efficiency, P_{TIR}, in addition to the luminophore radiative efficiency, PLQY. By systematic variation of critical design parameters, we explore the role of anisotropic luminophore emission for ideal step, dipole, and forward emitters on LSC conversion efficiency. We find that for the experimental luminophores and LSC design used for the present record LSC (conversion efficiency 7.1%), the upper anisotropic emission limit (P_{TIR} = 100%) increases this efficiency to 9.6%. Our model also shows that a modest geometrical gain (GG = 10) can be realized with a conversion efficiency of greater than 15% via anisotropic luminophore emission (P_{TIR} = 95%) with a luminescence quantum yield of 99%. Notably, a conversion efficiency above 25% is achievable for PLQY = 99% and full light trapping (P_{TIR} = 100%) at such a geometric gain. The recent demonstration of luminophores with ultrahigh luminescence quantum yield, combined with well-developed nanophotonics design and fabrication methods for anisotropic scatterers, can open the door to previously unreachable LSC conversion efficiencies.

6.4 Computational Methods

We employ a Monte Carlo ray-trace model to evaluate LSC conversion efficiency for varying GG, luminophore optical density, PLQY, and PL emission patterns. Previous studies have validated this model both with experimental data and also LSCs reported in the literature.[222] The Monte Carlo stochastically traces individual photons throughout each layer of the LSC. We initialize a constant grid matrix across the waveguide top surface area of 150 by 150 for all GGs, simulating photon wavelengths between 300 and 1200 nm in steps of 10 nm. Following the previous methods,[223] we model approximately 2 × 106 photons for each LSC module type to achieve statistically reliable results. We adopt an ideal luminophore absorption and PL profile with a Stokes shift of approximately 200 nm from the absorption edge (750 nm) to the PL center (950 nm). Each luminophore exhibits reabsorption, as shown in Figure 6.1c. We base the luminophore absorption band tail and PL full width at half maximum archetype core/shell quantum dot structures.

We track the photon's previous and current positions (x, y, z), previous and current velocity vectors (vx, vy, vz), and original and current wavelengths (λ_0, λ). Photons propagate through the LSC in discrete steps of 5 µm, where the current velocity determines the resulting direction. To determine the probability of luminophore absorption, we apply the Beer-Lambert law, given the optical density constant of that particular LSC for a given simulation step. To determine reflection and refraction angles at LSC layer interfaces, we apply Fresnel and Snell laws, respectively, for an assumed waveguide with a refractive index of 1.49 at the PL emission wavelengths, approximately 800-900 nm. We model current record high-efficiency Alta Devices' GaAs cells and simulate the photon-cell interaction through the measured reflectance and internal quantum efficiency, where we assume 2.5% of the cell surface area to be entirely reflective, representative of the front metal contact area. We assume GaAs edge-lined cells to optically couple to each of the four perimeter edges of 100 µm thick LSC waveguides, where we set the edge length according to the GG (GG of 1 corresponds to a 400 µm perimeter). We assume a perfect specular back reflector optically coupled to the bottom surface of the LSC to evaluate escape cone loss for only the top waveguide surface.

For each photon striking the LSC, we mark whether the photon is collected by one of the four edge-lined GaAs cells or lost via a particular mechanism. If collected, we weigh the original incident photon wavelength by the AM1.5G solar spectrum to calculate the resulting photocurrent density of a given GaAs cell. We assume the four GaAs cells to be connected in parallel. Once all photons are simulated and determined, collected or lost, we calculate the open circuit voltage and fill factor. To calculate the former, we assume an arbitrarily large dielectric waveguide electronic bandgap, such that any contribution from the waveguide matrix to the radiative dark saturation current of the GaAs cell is negligible. We then calculate the radiative limit open circuit voltage given the absorption spectra of the luminophore—scaling by the luminophore optical density and the emission out of the waveguide and into the escape cone. We also consider the contribution to the radiative dark current via background spectra photons reaching the GaAs cells directly—scaling by the system GG and emission out of the waveguide given by the refractive index. To account for cell nonradiative combination of photogenerated excitons, we apply an explicit approximation within such GaAs cells, as given by eq 7.60 Finally, we calculate the fill factor given previous explicit models that have shown close experimental matching and apply series and shunt resistances to match the diode behavior for current, record GaAs cells.[224]

$$V_{oc}^{nonrad} = \frac{kT}{q} \ln \left(\frac{2.5}{1 + 1/J_{sc}} \right) \tag{6.7}$$

To vary the angular distribution of emission for embedded luminophores, we generate a probability distribution function for each radiation pattern (i.e., a steplike, dipolelike, and forwardlike emission). We assume a uniform alignment of all luminophore emitters within the waveguide. The step emission profile, as depicted in Figure 6.1b, assumes a constant probability of emission for angles inside the escape cone for a waveguide refractive index of 1.49. We employ a dipole emission profile following previous studies of the emission angle.[209]

Finally, we model directional forward radiation to evaluate the LSC performance for a luminophore whose angular distribution is anisotropic in both the azimuthal and polar directions. Here, we assume a nanocone structure of a refractive index 2.5 hosting an embedded spherical luminophore. We performed full-wave electromagnetic simulations using the finite-difference time-domain (FDTD) method to model the far-field radiation pattern. In the full-wave simulations, we varied the nanocone central axis length, front and end radii, and emitter position along the central axis. We implemented a particle swarm optimization routine within this four-dimensional design space (i.e., axis length, front radius, end radius, emitter position) to probe the optimal performing structure, where the fraction of emission into the forward direction is taken as the figure of merit. The champion structure has an 887 nm axis length and radii of 180 and 1367 nm.

7

Unidirectional Luminescent Solar Concentrators

Luminescent solar concentrators have the potential to create low-cost solar energy conversion systems with reasonable conversion efficiency, if one succeeds in sufficiently reducing waveguide losses. Together with non-radiative recombination in the luminophores, escape cone losses of light that exits the waveguide before reaching the solar cells is one of the main loss mechanisms. It has been shown with optical simulations that these losses can be efficiently reduced by creating anisotropic emitting luminophores, which predominantly emit in the plane of the waveguide. So far, these simulations considered only anisotropy in emission. Reciprocity dictates, that such emitters will also demonstrate anisotropic absorption. In the case of aligned, unidirectional emitting structures, which emit the light in only one direction into the waveguide, the anisotropy in absorption can form an additional benefit in the reduction of photon reabsorption events. As the structures have high emissivity in the forward direction and low emissivity in the backward direction, light absorption from the backside will be reduced. This facilitates efficient traveling of photons in the forward direction and reduces waveguide losses. By implementing the effects of anisotropic absorption in a Monte Carlo ray-tracing model (MC model), the effect on luminescent solar concentrator performance is investigated. A large increase in efficiency is found, especially for high geometric gain values, while scattering losses due to the high index structures turn out negligible. This reveals the promising potential of unidirectional emitters for high efficiency, high geometric gain luminescent solar concentrators.

7.1 INTRODUCTION

Luminescent solar concentrators (LSCs) are gaining interest with the growing demand for photovoltaic (PV) systems for the transition to renewable energy.[225] Due to their ability to concentrate light from a large area with cheap glass or polymer sheets to small area solar cells, they can help in overcoming some of the foreseen material scarcity for the production of PV systems.[4] Furthermore, with their potential for semi-transparent and colorful designs, they are excellent candidates for building integrated PV[185] and other niche applications.[225] In the past decades, large improvements have been made in creating highly efficient luminophores, which are essential for creating efficient LSC devices.[226] In chapter 6, we have shown the great potential of engineering anisotropic emission patterns to reduce the escape cone losses, which up till now form one of the major loss mechanisms in LSCs. We showed that reducing escape cone losses is equally important as reducing the non-radiative recombination in the luminophores. In the analysis, we only focused on the effects of the emission pattern. This was done by implementing anisotropic emission patterns in a detailed Monte Carlo ray-tracing model. However, due to rules of reciprocity, also the absorption pattern will be influenced and become angular dependent and additional scattering might be induced. Given the encouraging results for anisotropic emitters, and especially the unidirectional forward emitting nanocones, a more detailed investigation including all optical effects is needed to reveal the full potential of this concept.

Anisotropic absorption will have both positive and negative consequences for the LSC performance, and the balance between these deserves further investigation. On the one hand, reduced emission into the escape cone will also lower the absorption of incoming sunlight. On the other hand, in the case of the unidirectional, aligned nanocones, reabsorption of photons traveling in the waveguide will be reduced. Again due to reciprocity, high emissivity in the forward direction and low emissivity in the backward direction will result in low absorption from the backside and high absorption from the front side. Light emitted by the luminophores will predominantly travel in the forward direction, and thus experience low absorption probability in the next, aligned nanocone. Any photons emitted in the backward direction will have a large chance of reabsorption, with subsequent re-emission in the forward direction. The path traveled by the photons in the waveguide will no longer be a random walk like it is for isotropic emitting luminophores, but will be a more straight path towards the solar cells. This reduces the total path length, and thereby reduces reabsorption probability even further. Finally, there is the presence of higher index nanophotonic structures in the waveguide, which introduce additional scattering. The amount and direction of this scattering also require further investigation.

In this work, we have implemented anisotropic absorption and additional scattering in the Monte Carlo ray-tracing model. To obtain the best LSC performance with these aspects included in the model, a new particle swarm optimization was run for the design of the unidirectional emitting nanocone. This time the structure was not only optimized for maximizing emission in the forward direction, but also for maximizing sunlight absorption and minimizing scattering. With these changes implemented in the Monte Carlo ray-tracing model, we analyze LSC performance for several design parameters.

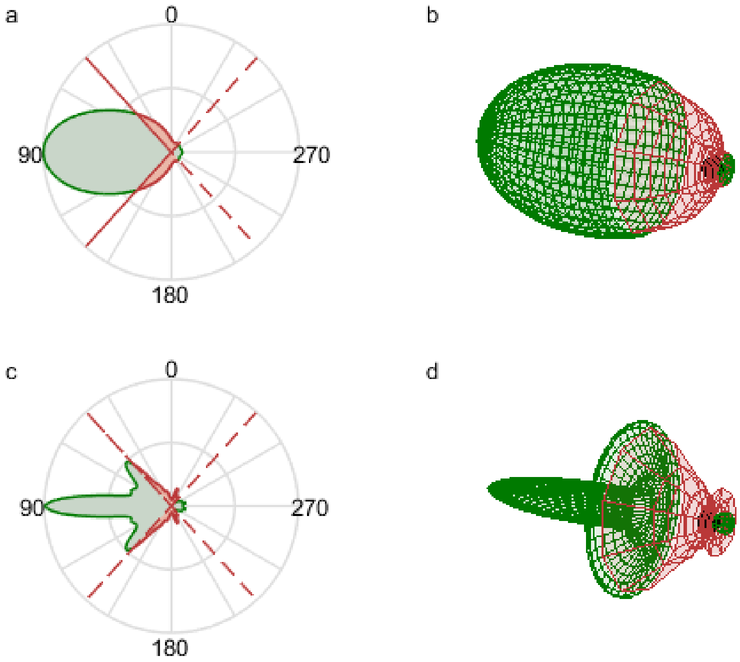

Figure 7.1: Emission and scattering profiles of the forward emitting nanocones. (a) and (b) 2D and 3D polar plots of the emission profile of a luminophore embedded in the nanocone, emitting at 850 nm. 49% of the light is emitted in forward direction and 16.5% is emitted into the escape cone. (c) and (d) 2D and 3D polar plots of the emission profile from an ensemble of 20 aligned but randomly positioned nanocones. Scattering with surrounding nanocones only slightly reduces the forward fraction to 45% and increases the escape cone losses to 17.5%. Parts in green experience total internal reflection and are guided by the waveguide, while parts in red are lost through the escape cone.

7.2 Results and discussion

A new particle swarm optimization was used to find a structure with a combination of high forward emission and sunlight absorption and low scattering. In addition to the two radii and length of the cone, also the refractive index was left as an optimization parameter, as this parameter plays an important role in the amount of scattering. The figure of merit was defined as the fraction of forward emission plus the amount of absorption minus the amount of scattering, each normalized to a value close to one, resulting in equal weight in the figure of merit calculation. The forward emission and scattering were calculated at the luminophore emission wavelength of 850 nm and absorption was determined at normal incidence in the wavelength range of 400 to 650 nm. From an initial random particle swarm with an average figure of merit of 0.79, the structures were optimized to an average figure of merit of 1.17. The best performing structure is a cone with end radii of 65 and 325 nm, a length of 234 nm, and a refractive index of 3.3 and has a figure of merit of 1.51. This structure has five times more absorption and two times less scattering than the forward emitter in the previous chapter, which results in ten times lower scattering for the same amount of sunlight absorption. The emission pattern in shown in figure 7.1 a and b.

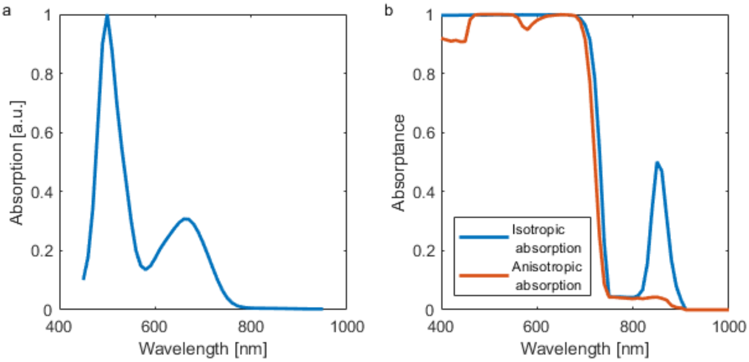

Figure 7.2: Absorption spectra of new optimized forward emitting nanocones. (a) Absorption spectrum of only the cone, as obtained from FDTD calculations with fixed imaginary part of the refractive index for all wavelengths. Due to the combined optimization for high absorption up to 700 nm and high emissivity in forward direction at 850 nm, absorption for normal incidence drops above 700 nm. (b) Absorption spectrum of the LSC device as obtained from the MC model, with and without the anisotropic absorption of the nanostructures implemented. Anisotropic absorption slightly reduces sunlight absorption, especially at the emission wavelength of the luminophores.

Scattering due to the nanocones is primarily problematic for light emitted by the luminophores: these are the photons that have to travel along the waveguide towards the PV cells, and thus have many chances of interacting with adjacent nanocones, while ideally they experience minimal disturbance along their way. We thus looked at scattering of forward traveling light, and investigated how the emission profile is altered after interaction with surrounding nanocones. When a plane wave hits the nanocones in forward direction, there is predominantly forward scattering, with a forward fraction of 60%. The performance of the nanocones is significantly better than the scattering behavior from isotropic particles like conventional luminophores, which give a forward fraction of 17%. This indicates that scattering will not significantly decrease LSC performance. When looking at an ensemble of nanocones, we observe only a small decrease in the forward fraction. The angular emission pattern resulting from an ensemble of 20 aligned, but randomly positioned nanocones is shown in figure 7.1c and d, and has has a fraction of 45% of light going in forward direction and 17.5% into the escape cone. For random scattering in the waveguide material, there is no decrease in performance for scattering distances down to 2.5 mm, where efficiency starts to drop. This is in agreement with results for isotropic emitters.[222] A complete analysis of the effect of scattering due to the nanocones would require the implementation of the full scattering profile for each possible angle of incidence of the cone. Since most light will be traveling in the forward direction through the waveguide, we believe that the current analysis is sufficient to conclude that increased scattering due to the presence of the nanocones will not significantly degrade performance.

The absorption spectrum for normal incidence purely due to the optical effects of the nanocone is shown in figure 7.2a. This spectrum is generated disregarding the absorption spectrum of the luminophore, by using a fixed absorption coefficient over all wavelengths. Over the visible part of the solar spectrum, for which the absorption was optimized, absorption is high. Above 700 nm it starts to drop, and at the emission wavelength of 850 nm absorptivity and emissivity in normal direction are almost zero, since the emission is guided in the forward direction. By implementing this nanocone absorption spectrum in the MC model, where it is combined with the absorption spectrum of the luminophores, the absorption spectrum of the LSC device can be determined. For approximately the same optical density over the visible spectrum, implementing the anisotropic absorption properties leads to a small decrease in sunlight absorption, as shown in figure 7.2b, especially at the emission wavelength of the luminophores. However, as we will see in the following, this lower absorption can be compensated by a higher luminophore loading, as reabsorption is reduced with the anisotropic absorption implemented.

With the absorption spectrum and angular profile implemented in the model, LSC performance was investigated for several design parameters. By comparing the nanocone design of the previous work, with ten times more scattering, to the new optimized design, we find an absolute increase of 2% in efficiency for the same optical density of 1, a geometric gain of 10, and photoluminescent quantum yield (PLQY) of 95%, revealing the importance of the three-fold optimization. Figure 7.3a shows the efficiency of the devices with the new cone design for varying optical density (OD), PLQY of 80% and 95%, and a geometric gain (GG) of 10, and shows the effect of implementing the anisotropic absorption properties. Performance is significantly increased by the implementation of anisotropy in absorption. For a PLQY of 95%, the maximum efficiency goes up from 11% to over 16%. While for isotropic absorption the efficiency drops for optical densities above 0.5 due to increased reabsorption losses, the anisotropic absorber peaks at an optical density of 1 and efficiency barely drops for higher OD values. These trends hold independent of luminophore PLQY. For increasing geometric gain the benefit becomes even more pronounced, as visible in figure 7.3b. The isotropic absorber shows a rapid drop in efficiency with increasing GG, but with anisotropic absorption, photons travel over longer distances with lower losses, and efficiency stays above 10% up to a GG of 75. One could think that solar cells on only one out of four LSC waveguide edges are required with this unidirectional emitter design, resulting in a four-times higher geometric gain. However, simulations show that it is still beneficial to have them on all four sides. With 50% of light emitted in the forward direction, the other half is still partly guided in other directions, resulting in the efficiency being halved with only one PV cell on the forward edge. As visible in figure 7.3b, the efficiency goes down by only a few percent when the collection area is increased by factor four, while keeping PV cells on all edges, which is thus the preferred way to increase GG. The low drop in efficiency with increasing geometric gain opens up possibilities for high efficiency, high geometric gain LSCs.

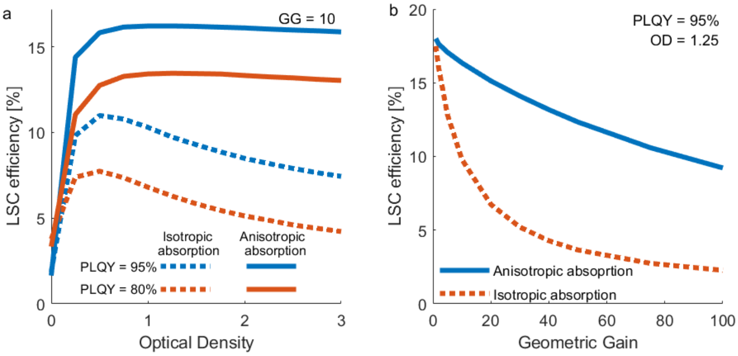

Figure 7.3: LSC performance with forward emitting nanocones, comparing the model with and without anisotropic absorption included. (a) LSC efficiency for varying optical density, for geometric gain of 10 and 20. Due to reduced reabsorption probability with anisotropic absorption included, higher optical densities can be used, and efficiency is significantly enhanced. The penalty for increased geometric gain is lower. This becomes more visible in (b), with efficiency as a function of geometric gain. With isotropic absorbing structures, efficiency drops rapidly due to the large losses associated with reabsorption. With anisotropic absorption, these losses are reduced and efficiency stays above 10% up to a geometric gain of 75.

7.3 CONCLUSIONS AND OUTLOOK

From this analysis, we can conclude that the effects of anisotropic absorption profiles, which are inherently related to anisotropic emission profiles, have a significant effect on LSC performance. Although the forward emitting nanocones cause a small reduction in sunlight absorption and increase scattering, the net result is a large efficiency increase due to reduced reabsorption probability and efficient paths towards the photovoltaic cells. The reduction in sunlight absorption can be compensated with higher luminophore loading, without directly being penalized with higher reabsorption losses. Light traveling in the forward direction through the waveguide will predominantly experience forward scattering from the nanocones, which therefore also does not lead to higher losses. To reach this situation, optimization of the nanocones for directional emission, high sunlight absorption, and low scattering is necessary.

In the current optimization, we focused on investigating the physical principles and their effects on performance. Practical fabrication limitations were not considered, to first see the maximum gain that can be obtained with this concept. As the improvements found are large, also with practical limitations the system has great potential. The next step would be a theoretical design and optimization of unidirectional emitting structures that can be fabricated for experimental verification and subsequent experimental realization.

SUMMARY

Many modern technologies involve some means of absorbing or generating light. This can vary from simply absorbing as much light as possible in solar cells, or brightly emitting with an LED light, to accurately detecting light signals from glass fibers or sending a single photon into an on-chip optical circuit. For all of these technologies, accurate light management is needed. This can be achieved with nanophotonics, where nanometer-sized objects interact with light in an accurately tunable manner. With transparent dielectric structures, light of a specific wavelength (range) can be sent into a specific direction, with minimal losses. Combining this with new materials, like the fascinating group of perovskite materials, directional light emission can be used to realize high-efficiency solar cells and more efficient optoelectronic devices, which we need for the transition to renewable energy.

Light management for solar cell performance does not only include maximizing light absorption, also controlling light emission is important. This counterintuitive fact, that a solar cell emits light, and actually has to be an efficient light emitter, is explained in Chapter 2 of this thesis. We derive that for reaching the absolute thermodynamic efficiency limit, the emission of a solar cell should match the incoming sunlight, both in spectrum and in angular spread. Sunlight comes in with a narrow beam, hence highly directional emission is needed to achieve such matching. We then present different nanophotonic techniques with which the spectral and angular emission properties of the solar cell can be better matched to the incoming sunlight. We model two theoretical solar cell designs that involve directional emission based on nanophotonic structures and analyze the performance in terrestrial application. We do so by calculating power conversion efficiency based on measured solar spectra throughout the year, to take into account the effect of cloudy days with a high fraction of diffuse sunlight and variations in the solar spectrum. Using nanostructures that reduce the cone of emission, while maintaining sensitivity to diffuse light, the performance can be increased by 15% compared to a regular planar cell. A bifacial LSC-tandem configuration based on nanophotonic structures can increase performance compared to a bifacial silicon cell by 41%, while a more conventional current matched tandem gives an increase of 28%. This shows the potential of nanophotonic engineering for further increasing solar cell efficiency.

In Chapter 3 we present a nanostructured microlens with a theoretical directivity of 160, for which it was optimized with an evolutionary algorithm. An experimental full directivity of 61±3 was measured, three times higher than the value found in previous work. Earlier limitations were overcome by making adjustments on three levels. Since the microlens performs best for point-source-like emission at the center of the lens, a more well-defined, localized emitter was fabricated with direct electron beam patterning of quantum dots. This resulted in clusters of ca 200 nm in size in an array with 20 μm pitch. Alignment markers helped in accurately positioning the lens on top of the emitter. Secondly, the lens fabrication with two-photon lithography was refined to achieve better

agreement between the designed and fabricated structures. Finally, a new setup was built in which a Fourier microscope is combined with an integrating sphere setup. This allowed for measuring the full directivity into all angles, contrary to other work, where emission in the back is typically ignored or estimated from simulations. The combination of these three improvements led to a record experimentally achieved directivity from dielectric structures.

The challenges of accurately positioning the lens on top of the emitter were overcome in the work described in Chapter 4, where we present a self-aligning and self-optimizing system. We exploit the light-induced halide segregation in mixed-halide perovskites to create a system that can be trained with an input stimulus of collimated light and responds with directional light emission. The same microlens as is in Chapter 3 is used, which creates an intense hotspot of strong field enhancement underneath the lens. This induces local halide segregation, leading to an iodide-rich region in the hotspot. Excited states funnel to this lower bandgap region, and as a consequence, almost all light emission originates from the location of the hotspot. Reciprocity dictates that since this hotspot has strong coupling to the incoming plane wave, there is also a strong coupling of the emission to this direction. Therefore the excitation at normal incidence results in highly directional emission into the normal direction. The resulting partial directivity into the numerical aperture of the objective of 16.4 is significantly higher than in the lithography-defined system, where a maximum value of 12.9 was found. In addition, the system shows some of the basic requirements for material learning or intelligent matter. It does not only mimic the input stimulus, but it also shows memory and learning over time: directivity is higher each time the lens is exposed again, and longer training leads to higher directivity. By analyzing the dynamics of emission intensity and directivity, some of the underlying mechanisms and their different time scales are revealed.

In Chapter 5 we further exploit the self-optimizing properties of mixed halide perovskite. Using simple silica microspheres, the self-aligning lens-emitter concept is used to make a self-tracking solar concentrator with diffuse sunlight utilization. Hereby we overcome the two main limitations of conventional solar concentrator systems, and at the same time harvest functionality from the usually undesired phase segregation in mixed halide perovskite solar cells. Although directivity from the spheres is lower than the microlenses in the previous chapters, their commercial availability and facile self-assembly in to large area monolayers makes them very suitable for application in solar cells. Optical simulations show that placing a monolayer of 5 μm silica spheres on top of a mixed halide perovskite film can give an absolute efficiency increase of 6.8% absolute. In full device configuration, including contacts and non-radiative recombination, the gain in efficiency is 5.1% absolute. Due to the concentrating effect of the spheres and the funneling towards the low bandgap regions, the higher carrier concentrations push the system closer to the radiative limit. This makes the two-phase-with-spheres system outperform any single-phase system. Experiments show that indeed a monolayer of spheres on top of the perovskite leads to directivity from a large area, and enhanced absorption into the low bandgap phase.

The final two chapters contain a study to the effect of anisotropic light emission on the performance of luminescent solar concentrators (LSCs). With an extensive Monte Carlo ray-tracing model, the different processes and loss mechanisms in an LSC could be accurately monitored. In Chapter 6 we present a systematic study of the effect of several design parameters on power conversion efficiency and their interdependencies. We show that reducing the probability of light emission into the escape cone of the waveguide is equally important as reducing the probability of non-radiative recombination. With out-of-plane dipole emission patterns, that have a doughnut shape in the plane of the waveguide, photon escape probability can be reduced to 9%, compared to 25% for isotropic emission. This increases efficiency by more than factor two, to a maximum efficiency of 25%. High index cone structures around the emitters can give emission into one in-plane direction. When these structures are aligned in the waveguide, light travels predominantly in one direction. This reduces the total path length in the waveguide and reduces the associated losses. While escape cone losses are slightly higher compared to the dipole emitter, the maximum efficiency is still 24%, thanks to the reduced path length. Modeling of the current world record LSC reveals that if the escape cone losses are reduced to zero using anisotropic emitters, the performance can be increased from 7.1% to 9.6%. This comprehensive analysis shows that by combining anisotropic emission, highly efficient luminophores, and optimization of the other design parameters, power conversion efficiencies of above 28% are achievable with LSCs.

In Chapter 7 we further investigate the effect of the unidirectional emitting nanocones on LSC efficiency. While in the previous chapter only anisotropic emission profiles were considered, we now implement also the anisotropic absorption that comes with such structures. While absorption of sunlight is slightly reduced, the net effect is a large increase in efficiency due to reduced reabsorption. As the nanocones emit predominantly in forward direction, absorption from the back side is reduced. This results in low reabsorption probability of photons traveling in the waveguide, and more direct paths towards the photovoltaic cells on the sides. Additional scattering due to the high index structures will not degrade performance, because the structures scatter mostly in the forward direction. This allows for reaching power conversion efficiencies above 10% with achievable PLQY of 95% for geometric gains up to 75.

Overall, this thesis shows the potential and application of directional light emission from dielectric nanostructures for optoelectronic devices, and in particular for efficient solar energy conversion. We provided a detailed background of how nanophotonic engineering can increase solar cell performance and a detailed study on how anisotropic emission can improve LSC performance. With a combination of theoretical and experimental work, we gave several examples of directional emission from dielectric nanostructures. On the one hand, we studied highly optimized nanophotonic microlenses that resulted in record directivity values. On the other hand, we show that with simple glass microspheres, which are easily self-assembled in large monolayers, moderate directivity over large areas can be achieved. By combining our photonic structures with mixed halide perovskite and exploiting the photo-induced halide segregation in the material, self-optimization and characteristics of material learning are observed. The insights from this thesis can lead to new approaches in light management for photovoltaics and result in further improvement in solar cell performance, which will be an essential aspect of the worldwide transition to renewable energy.

SAMENVATTING

Veel hedendaagse technologieën bevatten enige vorm van licht absorptie of uitstraling. Dit kan variëren van simpelweg zoveel mogelijk licht absorberen in een zonnecel of zo helder mogelijk licht uitstralen met een LED lamp, tot het zeer nauwkeurig detecteren van lichtsignalen uit glasvezelkabels of het uitzenden van één enkel lichtdeeltje in een optisch circuit op een chip. Voor al deze technologieën is het nodig om nauwkeurige controle over het licht te hebben. Dat kan worden bereikt met nanofotonika, waarbij objecten van nanometerformaat op nauwkeurig afstembare wijze met licht interageren. Met transparante diëlektrische structuren kan licht met een specifieke golflengte een specifieke richting ingezonden worden, met minimale verliezen. Door dit te combineren met nieuwe materialen, zoals de fascinerende groep van perovskiet materialen, kan directieve straling worden gebruikt om hoog efficiënte zonnepanelen en efficiëntere opto-elektronische toepassingen te realiseren, welke nodig zijn voor de transitie naar duurzame energie.

Goede controle over de interactie tussen licht en zonnecellen gaat niet alleen over het maximaliseren van licht absorptie, maar ook over het beheersen en sturen van licht dat wordt uitgezonden door de zonnecel. Dit tegen-intuïtieve gegeven, dat een zonnecel licht uitzendt, en zelfs een efficiënte lichtbron moet zijn, wordt uitgelegd in Hoofdstuk 2 van dit proefschrift. We tonen aan dat, om de maximale thermodynamische efficiëntie limiet te bereiken, het uitgezonden licht overeen moet komen met het invallende zonlicht, zowel in spectrum als in hoekverdeling. Zonlicht valt in met een smalle bundel, en dus is zeer directieve uitstraling nodig om een dusdanige overeenkomst te bereiken. Vervolgens presenteren we verschillende nanofotonische technieken waarmee het spectrum en de hoekverdeling van het door de zonnecel uitgezonden licht beter in overeenstemming kunnen worden gebracht met het invallende zonlicht. We modeleren twee theoretische zonnecelontwerpen die directieve licht uitzending gebaseerd op nanofotonische structuren bevatten, en analyseren hun prestatie in aardse omstandigheden. Dat doen we door de omzettingsefficiëntie te berekenen gebaseerd op een jaar rond gemeten zonlichtspectra, om op die manier de gevolgen van bewolkte omstandigheden met veel diffuus zonlicht en variaties in het zonnespectrum mee te nemen. Door gebruik te maken van nanostructuren die de hoeken waarin licht wordt uitgezonden verkleinen, terwijl de zonnecel tegelijkertijd wel gevoelig blijft voor diffuus licht vanuit andere hoeken, kan de prestatie worden verbeterd met 15% in vergelijking met een reguliere zonnecel. In een tweezijdige LSC-tandem configuratie gebaseerd op nanofotonische structuren kan de prestaties ten opzichte van een gewone tweezijdige silicium zonnecel worden verbeterd met 41%, terwijl een traditionele stroom-gelimiteerde tandemconfiguratie een verbetering van 28% oplevert. Dit toont de potentie van nanofotonisch ontwerpen om het rendement van zonnecellen verder te verhogen.

In Hoofdstuk 3 presenteren we een microlens met nanoschaal structuur met een theoretische directiviteit van 160, waarvoor de lens was geoptimaliseerd met een evolutionair algoritme. We maten een experimentele volledige directiviteit van 61±3, een driemaal hogere waarde dan gemeten in eerder werk. Eerdere beperkingen overwonnen we door aanpassingen op drie vlakken. Ten eerste, aangezien de microlens het best presteert voor een puntbron van licht in het midden van de lens, is een beter gedefinieerde en gelokaliseerde lichtbron gefabriceerd door middel van directe elektronenbundel-lithografie in kwantumdots. Dit resulteerde in clusters van ca 200 nm in omvang met een onderlinge afstand van 20 μm. Uitlijnmarkeringen hielpen bij het nauwkeurig positioneren van de lens bovenop de lichtbronnen. Ten tweede is de lensfabricage door middel van twee-foton lithografie verder verfijnd, om betere overeenstemming te krijgen tussen de ontworpen en de daadwerkelijk gefabriceerde vorm. Ten slotte is er een nieuwe meetopstelling gebouwd, waarin een Fourier microscoop is gecombineerd met een integrerende bol. Hiermee is het mogelijk de volledige directiviteit te meten in alle hoeken, in tegenstelling tot eerder werk, waarin de bijdrage van licht dat naar achteren wordt uitgezonden wordt verwaarloosd of afgeschat op basis van simulaties. Door de combinatie van deze drie verbeteringen bereiken we een record in experimenteel behaalde directiviteit van diëlektrische structuren.

De uitdagingen van het nauwkeurig plaatsen van de lens bovenop de lichtbron zijn overwonnen in het werk dat wordt beschreven in Hoofdstuk 4, waar we een zelf-uitlijnend en zelf-optimaliserend system introduceren. We maken gebruik van halidenscheiding onder invloed van licht in gemengde haliden perovskieten, om een systeem te creëren dat kan worden getraind met een input stimulus van een parallelle lichtbundel, en dat reageert met directieve licht uitzending. We maken gebruik van dezelfde microlens als in Hoofdstuk 3, die een intens focuspunt met sterke verhoging van het elektrische veld onder zich creëert. Dit veroorzaakt lokale halidenscheiding, wat leidt tot een jood-rijk gebied in het focuspunt. Aangeslagen elektronen bewegen naar dit gebied met lagere bandgap, en als gevolg hiervan komt vrijwel al het uitgezonden licht van de locatie van het focuspunt. Reciprociteit vereist dat aangezien het focuspunt een sterke koppeling heeft met de inkomende vlakke golf, er ook een sterke koppeling is tussen het uitgezonden licht en de richting van de inkomende golf. Daardoor veroorzaakt het aanslaan met een loodrecht invallende lichtbundel zeer directieve lichtuitzending terug in loodrechte richting. De resulterende gedeeltelijke directiviteit in de numerieke apertuur van het objectief van 16.4 is significant hoger dan in het eerder beschreven, op lithografie gebaseerde system, waarin een maximale waarde van 12.9 is gemeten. Daarbij vertoont dit systeem een aantal basiskenmerken van lerende, dan wel intelligente, materialen. Het imiteert niet alleen het inkomende signaal, maar het heeft ook een geheugen en kan leren over tijd: de directiviteit is iedere keer dat de lens wordt beschenen hoger, en langere training leidt tot hogere directiviteit. Door de dynamieken in licht intensiteit en directiviteit te analyseren, konden enkele van de onderliggende mechanismen en de daarbij horende tijdschalen worden geopenbaard.

In Hoofdstuk 5 benutten we de zelf-optimaliserende eigenschappen van gemengde haliden perovskieten verder voor het verbeteren van zonnecelprestaties. Door gebruik te maken van simpele glazen microbolletjes, wordt het zelf-uitlijnende lens-straler concept gebruikt om een zonneconcentrator te maken die zelf de beweging van de zon kan volgen en diffuus zonlicht kan benutten. Daarmee overwinnen we de twee voornaamste beperkingen van conventionele zonneconcentratoren, en tegelijkertijd benutten we de normaalgesproken ongewenste haliden scheiding in gemengde haliden perovskiet zonnecellen. Hoewel de directiviteit van de bolletjes lager is, maakt hun commerciële beschikbaarheid en eenvoudige zelforganisatie in monolagen met groot oppervlak ze erg geschikt voor toepassing in zonnecellen. Optische simulaties laten zien dat met het plaatsen van een monolaag van 5 μm grote glasbolletjes bovenop een gemengde haliden perovskiet film, een absolute verhoging in efficiëntie van 6.8% kan worden behaald. In een complete zonnecel-configuratie, waarin elektrische contacten en niet-stralende recombinatie zijn meegenomen, is de winst in efficiency 5.1%. Door het concentrerings-effect van de bolletjes en de gebiedjes met lage bandgap, ontstaan hogere concentraties van ladingdragers, waardoor het systeem meer richting de stralingslimiet wordt gedreven. Hierdoor doet het twee-fasen-met-bolletjes systeem het beter dan enig enkel-fase systeem. Experimenten laten zien dat het aanbrengen van een monolaag bolletjes op de perovskiet inderdaad zorgt voor directiviteit vanaf een groot gebied, en dat absorptie in de lage bandgap fase is verhoogd.

De laatste twee hoofdstukken bevatten een studie naar het effect van anisotrope lichtuitzending op lichtgevende zonne-concentrators (LSCs). Met een uitgebreid Monte Carlo lichtstraal-traceringsmodel konden de verschillende processen en verliezen in een LSC nauwkeurig in kaart worden gebracht. In Hoofdstuk 6 presenteren we een systematische studie naar het effect van verschillende ontwerpparameters op energie-omzettingsefficiëntie en hun onderlinge afhankelijkheden. We tonen aan dat het verkleinen van de kans op lichtuitzending in de ontsnappingskegel van de lichtgeleider even belangrijk is als het verkleinen van de kans op niet-stralende recombinatie. Met stralingspatronen van uit-het-vlak-wijzende dipolen, die een donut-vorm in het vlak van de lichtgeleider hebben, kan de ontsnappingskans gereduceerd worden tot 9%, ten opzichte van 25% voor isotrope straling. Dit verhoogt de efficiëntie met meer dan factor twee, tot een maximale efficiëntie van 25%. Nanokegels met een hoge brekingsindex rondom de lichtgevende deeltjes kunnen zorgen voor emissie in één specifieke richting. Als deze structuren zijn uitgelijnd in de lichtgeleider, zal het licht voornamelijk één richting op gaan. Dit verkort de totale weglengte in de lichtgeleider en vermindert de daarbij horende verliezen. Terwijl de verliezen in de ontsnappingskegel een fractie hoger zijn in vergelijking met de dipool lichtbron, is de maximale efficiëntie nog steeds 24%, dankzij de verkorte weglengte. Modelering van de huidige wereldrecord houdende LSC onthult dat als de ontsnappingskegel-verliezen naar nul kunnen worden gebracht door middel van anisotrope lichtbronnen, de prestatie kan worden verbeterd van 7.2% naar 9.6%. Deze omvangrijke analyse laat zien dat met anisotrope stralingspatronen, hoog efficiënte lichtgevende deeltjes, en optimalisatie van de andere ontwerpparameters, energie-omzettingsefficiënties hoger dan 28% haalbaar zijn met LSCs.

In Hoofdstuk 7 zoeken we het effect van unidirectioneel stralende nanokegels op LSC efficiëntie verder uit. Terwijl in het vorige hoofdstuk enkel anisotrope stralingsprofielen werden meegenomen, hebben we hier ook de anisotrope absorptie die hoort bij dergelijke structuren geïmplementeerd. Terwijl de opname van zonlicht iets afneemt, is het netto effect een grote toename in efficiëntie dankzij afgenomen reabsorptie. Aangezien de nanokegels voornamelijk in voorwaartse richting stralen, is absorptie aan de achterkant verkleind. Dit resulteert in kleinere kans op reabsorptie voor fotonen die zich door de lichtgeleider bewegen, en directere paden richting de zonnecellen aan de zijkanten. Bijkomende verstrooiing van het licht door de aanwezigheid van de structuren met hoge brekingsindex vermindert de prestatie niet, omdat de structuren voornamelijk in voorwaartse richting verstrooien. Dit maakt het mogelijk om efficiënties boven de 10% te halen met haalbare luminicentie kwantumrendement van 95% voor geometrische versterking van 75.

In zijn geheel laat dit proefschrift de potentie en toepassing zien van directieve licht uitstraling door middel van diëlektrische nanostructuren voor opto-elektronische apparaten, en in het bijzonder voor efficiënte zonne-energie conversie. We hebben een gedetailleerde achtergrond gegeven van hoe nanofotonische ontwerpen zonnecel efficiëntie kunnen verhogen, en hebben in detail bestudeerd hoe anisotrope straling de prestaties van LSCs kan verbeteren. Met een combinatie van theoretisch en experimenteel werk, hebben we verscheidene voorbeelden gegeven van directieve straling van diëlektrische nanostructuren. Aan de ene kant hebben we sterk geoptimaliseerde nanofotonische microlenzen bestudeerd, die resulteerden in record waardes in directiviteit. Aan de andere kant lieten we zien dat met simpele glazen microbolletjes, die zichzelf gemakkelijk organiseren in monolagen, redelijke directiviteit over een groot oppervlak bereikt kan worden. Door onze nanofotonische structuren te combineren met gemengde haliden perovskiet, en door gebruik te maken van de lichtgedreven halidenscheiding in dit materiaal, zijn zelf-optimalisatie en kenmerken van lerende materialen waargenomen. De inzichten uit dit proefschrift kunnen leiden tot nieuwe benaderingen in licht sturing en controle voor zonnecellen en kunnen resulteren in verdere verbeteringen in zonnecel prestaties, wat een essentieel onderdeel zal zijn van de wereldwijde transitie naar duurzame energie.

ACKNOWLEDGEMENTS

A PhD is often considered a solitary job, but nonetheless I could not have completed this thesis without the help and support of many great people. In the very first place I want to thank AMOLF as a whole, with everybody that contributed to the wonderful working atmosphere. There is no place other than AMOLF where I would have wanted to do my PhD. While of course almost all postdocs, PhD and master students are different from those that were around when I started, the atmosphere has stayed the same. Even though social contacts and activities have been limited in the past two years, I still feel like I have a good connection with many of you, thanks to the active involvement whenever there are opportunities to interact with each other. This has led to many valuable collaborations and scientific discussions, but also to lots of fun and good conversations over tea, at the balcony and at great activities organized by the personeelsvereniging.

Of course I start with saying thank you to my supervisor **Erik Garnett**. He gave me the opportunity to work at this place, be involved in very interesting and relevant research and develop myself as a scientific researcher. I've very much enjoyed our scientific discussions, for which I could always walk into your office. We could get lost in some complex discussions about thermodynamic limits, ending usually with more questions than we started with, but also with many new insights and ideas. Although sometimes slightly overwhelming, your infinite flow of interesting ideas and suggestions is impressive and inspiring. I also have great respect for how you combine your scientific career with family life, and it was lovely to see you in your father role during the group trip, where you showed endless energy for both scientific activities and family matters.

Speaking about family, the next big 'thank you' goes to my direct family. In de eerste plaats natuurlijk naar **Daan**, die in de afgelopen jaren het dichts bij mij heeft gestaan. Als je me plaagde of me met leuke, interessante of onbenullige dingen van mijn werk hield, dreigde ik dat ik behalve een Dankwoord voor jou ook een Ondankswoord in mijn proefschrift zou opnemen. Maar niets is natuurlijk minder waar! Je hebt me altijd gesteund met goede vragen en advies als ik het moeilijk had of gefrustreerd was, en was er altijd voor een luisterend oor en een knuffel. Je hebt nooit geklaagd als ik opeens veel later thuis was vanwege labwerk en was altijd flexibel en klaar om bij te springen wanneer dat nodig was.

Sinds de komst van onze dochter Yara is hulp van familie heel belangrijk geweest. Hoewel ik van mening ben dat het vanzelfsprekend zou moeten zijn dat ook vaders minder gaan werken om voor de kinderen te zorgen, ben ik heel dankbaar dat dit bij ons ook inderdaad vanzelfsprekend was, en het is heerlijk om te zien wat **Daan** allemaal met onze Yara onderneemt op zijn papadag. Daarnaast hebben we fantastische hulp gehad van onze ouders. Zowel Daans beide ouders, **Maud** en **Jan Willem**, als mijn moeder **Caroline**, zijn

de eerste maanden elke week komen oppassen, waardoor ik met een goed gevoel weer aan het werk kon. Daarna is dat over gegaan in elk om de week oppassen. De overige twee dagen ging Yara naar Het Kleine Huis van onze fantastische Marga. Heel veel dank voor de fijne plek die jij hebt gecreëerd, Marga! Hier kon ik Yara altijd met een gerust hart achterlaten en lekker weer even de wetenschap induiken.

Tot slot wil ik mijn vader **Geert-Jan**, mijn zus **Fiona** en haar vriend **Wytze** bedanken voor hun aanwezigheid, support en interesse in de afgelopen jaren. **Geert-Jan**, bij jou kan ik terecht voor goede inzichten bij moeilijke keuzes, en gewoon lekker praten over de interessante aspecten van ons werk. **Fiona** wil ik bedanken voor haar onvoorwaardelijke aanwezigheid wanneer ik haar nodig had. Ik weet dat ik je altijd kan bellen voor een fijn gesprek, met empathie maar ook een nuchtere blik op de zaken. En **Wytze**, met wie ik de passie voor wetenschap deel, voor leuke gesprekken over onderzoek maar ook alles daarbuiten, en inzichten over hoe het er in andere vakgroepen en onderzoeksgebieden aan toegaat.

Many results presented in this thesis would not have been achieved without the direct help of and collaboration with my colleagues. This started with help, advice and training from **Eric Johlin**, whose project I took over at the start of my PhD. Throughout the years you have always been available for questions and discussions and for help with using the great evolutionary algorithm that you have written. Thank you for all of this! Most of my PhD I have shared the office with **Sven**. Although our research topics are quite different, we have had many good conversations. You are a great researcher and gave me a lot of good advice and practical tips, but also valuable insights about personals matters and life in general. Together with Sven we made sure that **Susan** would join our office when she started her PhD, which was a great call. You always cheer up the office with a good chat, or open up a relieving grumbling session about how frustrating PhD life can be. You did a great job in supervising the master students in our shared projects when I was on maternity leave, such that a great amount of work was done when I returned. I'm happy that we have continued working together on these projects and will keep doing so in the near future, and I'm sure some nice publications will come out. We have also had valuable conversations about personal matters and I felt support and empathy from you in difficult times. Thank you for everything! The great work that was done while I was on maternity leave was conducted by **Jeroen** en **Francesca**. Thanks to you the projects continued and some beautiful results have come out. It was great to work with such intelligent, motivated and diligent people and I'm happy you've stayed at AMOLF for your PhD.

Before Yara was born, my little baby was the optical setup that I have been working with since the start of my PhD. A big part of this had been built several years before by **Sander Mann**, who had already left when I started. Nonetheless you were available for consultancy and advice for working with this rather complex setup. But most of the training I received from **Parisa** and **Jenny**. Even though this setup was not fully your field of expertise, you both helped me the best you could. And outside the dark optical lab we had a good time talking about life as a PhD and I learned a lot from you. Most of the struggles with this setup, however, I have shared with **Eitan**. From the moment you started your postdoc in our group I've appreciated your attitude and personality. We have faced a lot of challenges with the setup and the laser, but together we could handle it. You have helped me shaping my projects by asking critical questions, thinking along and sharing interesting publications about related topics. After I joined the team of ‘young parents’, I felt an extra connection with you within the group and it was nice to have someone to share also these aspects of life with. I think you are a great researcher and a great person and I strongly hope that you find a position that fits both your intellect and family matters and brings you joy.

For building my part of the optical setup, I’ve received help from many people. For the optics parts I frequently consulted **Marko Kamp** to figure out the right lenses, filters, mounting constructions and the camera. I designed a new sample holder with **Ricardo**: thank you for the nice drawings and good suggestions. Several iterations were accurately manufactured by **Wouter**, thank you for your careful work. The holders work great now! And for many small technical issues and quick fixes I could always walk into **the workshop** and get help immediately. It is amazing that we have such a place at AMOLF and the added value of quickly solving little technical problems can’t be overestimated. For running my measurements smoothly I have to thank **Jorijn**, who updated the control software of the setup to my wishes, with all the features and options I needed.

A fancy setup is nice, but it is worthless without samples to measure. Also in the sample preparation many people have been involved. The beautiful results of my first experimental paper would not have been possible with the great e-beam lithography skills of **Christian Dieleman**. Thank you for optimizing your process to get it to work for my needs and for the many samples you have fabricated for me! And again I want to thank **Susan**, **Jeroen** and **Francesca** for preparing perovskite samples for me, which were essential for the experimental projects that followed. Further processing of the samples I did mostly in the cleanroom, where I received excellent support from **Dimitri, Bob, Igor and Dylan**. Whenever I called with a little panic or small uncertainty you would be there in a minute to help me out! Finally a very big thanks goes to our group technician **Marc Duursma**. I feel more at home in a laser lab; in the chemical lab I always feel a bit uncomfortable. Luckily you were there to answer any questions, search for missing parts or bottles and to just help out with anything I would ask you. You have no problems finding your way in any lab, so also in the optical lab you have helped me with a nice box around the setup and to install the new laser.

For probably any aspect of my PhD, my dear colleague **Tom Veeken** has played an important role. Although you started your PhD not so long before me, I’ve always looked up to you for your knowledge and skills. Our research topics showed close resemblance and it was great when we found a suitable project to join forces. This resulted in a beautiful publication, also in great collaboration with **David Needell**. Next to the inspiring discussions and good team work in this project you have contributed to the completion of this thesis in many other aspects: practical help with optical measurements on your setup, tips, scripts and clear explanations to do optical simulations and use the supercomputer. Moreover, all our good conversations cheered up my mood and motivated me even more for my PhD and working in sustainable development in general. And finally you will stand by my side during the defense of this thesis as one of my paranymphs! Thank you for everything!

Then there are many other colleagues that made my PhD a success, by contributing to the great working atmosphere at AMOLF, providing feedback or inspiring me during talks or poster sessions, answering small questions and solving little issues in the lab, building and maintaining setups that I benefited from, and just by having fun conversations over coffee or tea. From the Nanoscale Solar Cells group **Sarah, Linde, Daan, Elaina, Hongyu, Rohit** and again **Susan**, thank you for being great colleagues and especially thank you for the good company and fun during the group trip, with great organization thanks to **Sarah**. Thank you **Nelson** for doing some optical measurements I could not do on my own setup. Hopefully these make it into a publication soon. And furthermore **Lucie, Imme, Magda, Verena, Nasim, Robin, Dominique, Silvia, Gianluca, Jeroen, Yorick, Daphne, Mees, Francesca, Jesse, Roel, Jente, Marloes, Lukas, Nick and anybody I might forget now**: thank you for being part of AMOLF and I'm happy I got to know you. And finally **Mareike**, although you work in a very different field and we have no scientific collaboration or interaction whatsoever, I just really liked your sparkling personality from the moment we met at one of the AMOLF activities. Of course general PhD struggles and experiences transcend specific research fields, so here we could exchange experiences. I'm very happy that you will be at my side during my defense as my paranymph and I look forward to preparing for this day with you!

Of course the group leaders at AMOLF play an important role in setting the working atmosphere at AMOLF and in training and coaching students to become good scientists. Not only Erik has guided me throughout my PhD, also many of you have guided my projects into the right direction by asking good questions and through the inspiring work that is being done in each of your groups. **Wim N.**, we had some nice ideas for collaborations and tried several of them. The fact that not every scientific idea turns into a great success doesn't make these collaborations less valuable. I love the work that is being done in your group and I have always enjoyed talking with you and your group members. **Bruno**, as one of the LMPV group leaders we have had many interactions. You were the one to suggest at a poster session that Christians e-beam patterning could be useful for me, which it definitely turned out to be. Thank you for your input to my projects and our nice conversations. **Esther**, I've not had direct collaborations with your group members, but nonetheless your questions and input have been of great value. Also it means a lot to me to see how a female scientist can combine family life with great scientific work; you are a role model for all of us! **Femius**, at the beginning of my PhD we have had some insightful discussions about nanophotonic effects that got me deep into the topic. Although my projects have moved in a slightly different direction, some of these questions are still relevant. Thank you for your input and for being part of my defense committee.

Last but not least: **Albert**. Recently at a panel discussion at a conference, the difference between a mentor and a supervisor was discussed, and that these do not have to be the same person. While Erik has been a great supervisor for me, I think I can call you a true mentor, guiding me in the non-scientific aspects of a PhD. I have deep respect for you as a person and the way you set a very positive vibe within LMPV, your optimism and your enthusiasm. The positive impact of your influence on people and the life and career of young scientists cannot be overestimated. Thank you for everything you have done for me, for AMOLF and for the PV community in general!

I have mentioned several names from the support staff that were directly involved in my work. However, behind the screens many more people have done important work, which made everything run smoothly at AMOLF. Activities I was probably most of the time not even aware of, because it was just done so well. From the ICT department I thank specifically **Wiebe** for jumping in for PC problems, and the rest of the **ICT team** for all their work in the past years. **Juliette** from the reception and **Gerda** from the canteen, who always showed sincere interest in how I was doing. **Sharlene** from human resources, with who I shared the experience of early motherhood and the hassle of pumping during working hours. **Teressa** from the secretarial office, with all your enthusiasm at social activities. The people in **finance** and the **stockroom**, thank you for helping out with ordering and sending things I needed. And finally a big thank you to everybody at AMOLF in **all the support teams** that made my life so much easier without me even being aware of it!

AMOLF is a wonderful place with wonderful people and I'm very grateful that I found this place to do my PhD. Fortunately Erik offered me the opportunity to stay a little longer as a postdoc, to help organizing the rapid growth that the Nanoscale Solar Cells group will go through in the coming year. I look forward to sharing my knowledge with current and future PhD and master students and I hope I can contribute to giving them the same wonderful experience of working at AMOLF. AFter that I will take my experiences with me in future steps in life and I will cherish all the good memories of the people at AMOLF. Thank you!

LIST OF PUBLICATIONS

This thesis is based on the following publications:

- **Chapter 2:** *Nanophotonic Emission Control for Improved Photovoltaic Efficiency*, J.S. van der Burgt and E.C. Garnett, ACS Photonics, 2020, 7, 7, 1589–1602
  Author contributions: JSB performed simulations and data analysis, created figures and wrote the manuscript, ECG provided supervision and helped with constructing the story line.
- **Chapter 3:** *Integrating Sphere Fourier Microscopy of Highly Directional Emission*, J. S. van der Burgt, C.D. Dieleman, E. Johlin, J.J. Geuchies, A.J. Houtepen, B. Ehrler, and E.C. Garnett, ACS Photonics, 2021, 8, 4, 1143–1151
  Author contributions: JSB fabricated and optimized the lenses, built the measurement setup, performed all measurements and data analysis and wrote the manuscript. CDD provided the e-beam patterned quantum dots, which were synthesised by JJG. EJ wrote the evolutionary algorithm and used this to optimize the lens design. AJH, BE and ECG provided supervision.
- **Chapter 4:** *Perovskite Plasticity: Exploiting Instability for Self-Optimized Performance*, J. S. van der Burgt, F. Scalerandi, J. de Boer, S. Rigter and E.C. Garnett, Adv. Func. Mat. under review
  Author contributions: JSB fabricated the lenses, performed all measurements and data analysis and wrote the manuscript. FS and JdB did the early work and initial experiments and FS provided spin coated perovskite substrates for the final experiments. SR helped with experiments and characterization, ECG provided supervision.
- **Chapter 6:** *Unlocking Higher Power Efficiencies in Luminescent Solar Concentrators through Anisotropic Luminophore Emission*, J. S. van der Burgt, D.R. Needell, T. Veeken, A. Polman, E.C. Garnett, and H.A. Atwater, ACS Appl. Mater. Interfaces 2021, 13, 34, 40742–40753
  Author contributions: JSB, DRN and TV worked together on implementing anisotropic emission into the Monte Carlo model, designing the simulations, analyzing the data and writing the manuscript. AP, ECG and HAA provided supervision.

In preparation:

- **Chapter 5:** *A Solar Concentrator Exhibiting Self-Tracking and Diffuse Light Utilization*, J.S. van der Burgt, S. Rigter, N. de Gaay Fortman, E.C. Garnett
  Author contributions: JSB did all simulations and data analysis, self-assembly of spheres and absorption measurements and wrote the manuscript, S.R. provided perovskite sampled and contributed to the writing, NGF performed the Fourier microscope measurements and ECG provided supervision.
- **Chapter 7:** *Unidirectional Luminescent Solar Concentrators*, J.S. van der Burgt, E.C. Garnett
  Author contributions: JSB implemented anisotropic absorption in the Monte Carlo model, ran simulations, analyzed the dat and wrote the manuscript, ECG provided supervision.

Other publications by the author:

- *Cuboidal Supraparticles Self-Assembled from Cubic $CsPbBr_3$ Perovskite Nanocrystals*, J.S. van der Burgt, J.J. Geuchies, B. van der Meer, H. Vanrompay, D. Zanaga, Y. Zhang, W. Albrecht, A.V. Petukhov, L. Filion, S. Bals, I. Swart, and D. Vanmaekelbergh, J. Phys. Chem. C 2018, 122, 27, 15706–15712
- *Direct Patterning of $CsPbBr_3$ Nanocrystals via Electron-Beam Lithography*, C.D. Dieleman, J.S. van der Burgt, N. Thakur, E.C. Garnett, and B. Ehrler, ACS Appl. Energy Mater. 2022, 5, 2, 1672–1680

REFERENCES

REFERENCES

[1] F. Hutmacher, “Why Is There So Much More Research on Vision Than on Any Other Sensory Modality?,” *Frontiers in Psychology*, vol. 10, p. 2246, 2019.

[2] World Energy Council, “Energy Resources: Solar,” *World Energy Resources: Solar*, pp. 1–28, 2013.

[3] IRENA, “World energy transitions outlook,” tech. rep., IRENA, 2021.

[4] J. C. Goldschmidt, L. Wagner, R. Pietzcker, and L. Friedrich, “Technological learning for resource efficient terawatt scale photovoltaics,” *Energy and Environmental Science*, vol. 14, pp. 5147–5160, oct 2021.

[5] J. Feldmann, N. Youngblood, C. D. Wright, H. Bhaskaran, and W. H. Pernice, “All-optical spiking neurosynaptic networks with self-learning capabilities,” *Nature*, vol. 569, no. 7755, pp. 208–214, 2019.

[6] W. Zhang, B. Gao, J. Tang, P. Yao, S. Yu, M. F. Chang, H. J. Yoo, H. Qian, and H. Wu, “Neuro-inspired computing chips,” *Nature Electronics*, vol. 3, no. 7, pp. 371–382, 2020.

[7] J. Ramanujam, D. M. Bishop, T. K. Todorov, O. Gunawan, J. Rath, R. Nekovei, E. Artegiani, and A. Romeo, “Flexible CIGS, CdTe and a-Si:H based thin film solar cells: A review,” *Progress in Materials Science*, vol. 110, p. 100619, may 2020.

[8] E. C. Garnett, B. Ehrler, A. Polman, and E. Alarcon-Llado, “Photonics for Photovoltaics: Advances and Opportunities,” *ACS Photonics*, vol. 8, pp. 61–70, jan 2021.

[9] K. R. Catchpole, S. Mokkapati, F. Beck, E. C. Wang, A. McKinley, A. Basch, and J. Lee, “Plasmonics and nanophotonics for photovoltaics,” *MRS Bulletin*, vol. 36, no. 6, pp. 461–467, 2011.

[10] A. Polman, M. Knight, E. C. Garnett, B. Ehrler, and W. C. Sinke, “Photovoltaic materials: Present efficiencies and future challenges,” *Science*, vol. 352, no. 6283, 2016.

[11] A. Kojima, K. Teshima, Y. Shirai, and T. Miyasaka, “Novel Photoelectrochemical Cell with Mesoscopic Electrodes Sensitized by Lead-halide Compounds,” *ECS Meeting Abstracts*, pp. MA2007–02 352, sep 2007.

[12] L. Protesescu, S. Yakunin, M. I. Bodnarchuk, F. Krieg, R. Caputo, C. H. Hendon, R. X. Yang, A. Walsh, and M. V. Kovalenko, “Nanocrystals of Cesium Lead Halide Perovskites ($CsPbX_3$, X = Cl, Br, and I): Novel Optoelectronic Materials Showing Bright Emission with Wide Color Gamut.,” *Nano letters*, vol. 15, pp. 3692–3696, jun 2015.

[13] L. Schmidt-Mende, V. Dyakonov, S. Olthof, F. Ünlü, K. M. T. Lê, S. Mathur, A. D. Karabanov, D. C. Lupascu, L. M. Herz, A. Hinderhofer, F. Schreiber, A. Chernikov, D. A. Egger, O. Shargaieva, C. Cocchi, E. Unger, M. Saliba, M. M. Byranvand, M. Kroll, F. Nehm, K. Leo, A. Redinger, J. Höcker, T. Kirchartz, J. Warby, E. Gutierrez-Partida, D. Neher, M. Stolterfoht, U. Würfel, M. Unmüssig, J. Herterich, C. Baretzky, J. Mohanraj, M. Thelakkat, C. Maheu, W. Jaegermann, T. Mayer, J. Rieger, T. Fauster, D. Niesner, F. Yang, S. Albrecht, T. Riedl, A. Fakharuddin, M. Vasilopoulou, Y. Vaynzof, D. Moia, J. Maier, M. Franckevičius, V. Gulbinas, R. A. Kerner, L. Zhao, B. P. Rand, N. Glück, T. Bein, F. Matteocci, L. A. Castriotta, A. Di Carlo, M. Scheffler, and C. Draxl, "Roadmap on organic-inorganic hybrid perovskite semiconductors and devices," *APL Materials*, vol. 9, p. 109202, oct 2021.

[14] M. A. Green, A. Ho-Baillie, and H. J. Snaith, "The emergence of perovskite solar cells," *Nature Photonics*, vol. 8, no. 7, pp. 506–514, 2014.

[15] International Renewable Energy Agency, "Renewable Power Generation Costst in 2017," 2018.

[16] D. Chung, C. Davidson, R. Fu, K. Ardani, and R. Margolis, "U.S. Photovoltaic Prices and Cost Breakdowns : Q1 2015 Benchmarks for Residential , Commercial , and Utility-Scale Systems," *National Renewable Energy Laboratory*, 2015.

[17] International Energy Agency, "Technology Roadmap Solar Photovoltaic Energy," 2014.

[18] M. L. Brongersma, Y. Cui, and S. Fan, "Light management for photovoltaics using high-index nanostructures," *Nature Materials*, vol. 13, no. 5, pp. 451–460, 2014.

[19] H. A. Atwater, A. Polman, E. D. Kosten, D. Callahan, P. Spinelli, C. Eisler, M. Escarra, E. Warmann, and C. Flowers, "Nanophotonic design principles for ultrahigh efficiency photovoltaics," *AIP Conference Proceedings*, vol. 1519, pp. 17–21, 2013.

[20] A. F. Koenderink, "Single-Photon Nanoantennas," *ACS Photonics*, vol. 4, no. 4, pp. 710–722, 2017.

[21] S. A. Mann, S. Z. Oener, A. Cavalli, J. E. Haverkort, E. P. Bakkers, and E. C. Garnett, "Quantifying losses and thermodynamic limits in nanophotonic solar cells," *Nature Nanotechnology*, vol. 11, no. 12, pp. 1071–1075, 2016.

[22] W. Shockley and H. J. Queisser, "Detailed Balance Limit of Efficiency of pn Junction Solar Cells," *Journal of Applied Physics*, vol. 32, no. 1961, pp. 510–519, 1961.

[23] G. L. Araújo and A. Martí, "Absolute limiting efficiencies for photovoltaic energy conversion," *Solar Energy Materials and Solar Cells*, vol. 33, no. 2, pp. 213–240, 1994.

[24] E. D. Kosten, B. K. Newman, J. V. Lloyd, A. Polman, and H. A. Atwater, "Limiting light escape angle in silicon photovoltaics: Ideal and realistic cells," *IEEE Journal of Photovoltaics*, vol. 5, no. 1, pp. 61–69, 2015.

[25] M. Peters, J. C. Goldschmidt, T. Kirchartz, and B. Bläsi, "The photonic light trap-Improved light trapping in solar cells by angularly selective filters," *Solar Energy Materials and Solar Cells*, vol. 93, no. 10, pp. 1721–1727, 2009.

[26] M. Peters, J. C. Goldschmidt, P. Löper, B. Groß, J. Üpping, F. Dimroth, R. B. Wehrspohn, and B. Blasi, "Spectrally-Selective photonic structures for PV applications," *Energies*, vol. 3, no. 2, pp. 171–193, 2010.

[27] A. Martí, J. L. Balenzategui, and R. F. Reyna, "Photon recycling and Shockley's diode equation," *Journal of Applied Physics*, vol. 82, no. 8, pp. 4067–4075, 1997.

[28] Y. Cui, D. Van Dam, S. A. Mann, N. J. Van Hoof, P. J. Van Veldhoven, E. C. Garnett, E. P. Bakkers, and J. E. Haverkort, "Boosting Solar Cell Photovoltage via Nanophotonic Engineering," *Nano Letters*, vol. 16, no. 10, pp. 6467–6471, 2016.

[29] D. Zhang, L. Gu, Q. Zhang, Y. Lin, D. H. Lien, M. Kam, S. Poddar, E. C. Garnett, A. Javey, and Z. Fan, "Increasing Photoluminescence Quantum Yield by Nanophotonic Design of Quantum-Confined Halide Perovskite Nanowire Arrays," *Nano Letters*, vol. 19, no. 5, pp. 2850–2857, 2019.

[30] A. F. Koenderink, A. Alù, and A. Polman, "Nanophotonics: Shrinking light-based technology," *Science*, vol. 348, pp. 516–521, may 2015.

[31] A. De Vos and H. Pauwels, "On the thermodynamic limit of photovoltaic energy conversion," *Applied Physics*, vol. 25, no. 2, pp. 119–125, 1981.

[32] G. Kirchhoff, "Ueber das Verhältniss zwischen dem Emissionsvermögen und dem Absorptionsvermögen der Körper für Wärme und Licht," *Annalen der Physik*, vol. 185, no. 2, pp. 275–301, 1860.

[33] T. Kirchartz and U. Rau, "What Makes a Good Solar Cell?," *Advanced Energy Materials*, vol. 8, pp. 1703385 (1–19), 2018.

[34] M. A. Green and S. P. Bremner, "Energy conversion approaches and materials for high-efficiency photovoltaics," *Nature Materials*, vol. 16, no. 1, pp. 23–34, 2016.

[35] J. F. Guillemoles, T. Kirchartz, D. Cahen, and U. Rau, "Guide for the perplexed to the Shockley–Queisser model for solar cells," *Nature Photonics*, vol. 13, no. 8, pp. 501–505, 2019.

[36] M. A. Green, E. D. Dunlop, D. H. Levi, J. Hohl-Ebinger, M. Yoshita, and A. W. Ho-Baillie, "Solar cell efficiency tables (version 54)," *Progress in Photovoltaics: Research and Applications*, 2019.

[37] E. C. Garnett, M. L. Brongersma, Y. Cui, and M. D. McGehee, "Nanowire Solar Cells," *Annual Review of Materials Research*, vol. 41, no. 1, pp. 269–295, 2011.

[38] H. Savin, P. Repo, G. Von Gastrow, P. Ortega, E. Calle, M. Garín, and R. Alcubilla, "Black silicon solar cells with interdigitated back-contacts achieve 22.1% efficiency," *Nature Nanotechnology*, vol. 10, pp. 624 – 629, 2015.

[39] J. Oh, H. C. Yuan, and H. M. Branz, “An 18.2%-efficient black-silicon solar cell achieved through control of carrier recombination in nanostructures,” *Nature Nanotechnology*, vol. 7, no. 11, pp. 743–748, 2012.

[40] L. E. Black, A. Cavalli, M. A. Verheijen, J. E. Haverkort, E. P. Bakkers, and W. M. M. Kessels, “Effective Surface Passivation of InP Nanowires by Atomic-Layer-Deposited Al2O3 with POx Interlayer,” *Nano Letters*, vol. 17, no. 10, pp. 6287–6294, 2017.

[41] Q. Zhang, M. M. Tavakoli, L. Gu, D. Zhang, L. Tang, Y. Gao, J. Guo, Y. Lin, S. F. Leung, S. Poddar, Y. Fu, and Z. Fan, “Efficient metal halide perovskite light-emitting diodes with significantly improved light extraction on nanophotonic substrates,” *Nature Communications*, vol. 10, pp. 727 (1–9), 2019.

[42] O. Isabella, Klaus Jäger, Arno Smets, René van Swaaij, and Miro Zeman, *Solar Energy: The Physics and Engineering of Photovoltaic Conversion, Technologies and Systems.* UIT Cambridge Ltd., 2016.

[43] U. Rau, U. W. Paetzold, and T. Kirchartz, “Thermodynamics of light management in photovoltaic devices,” *Physical Review B - Condensed Matter and Materials Physics*, vol. 90, no. 3, pp. 1–16, 2014.

[44] J. M. Richter, M. Abdi-Jalebi, A. Sadhanala, M. Tabachnyk, J. P. Rivett, L. M. Pazos-Outón, K. C. Gödel, M. Price, F. Deschler, and R. H. Friend, “Enhancing photoluminescence yields in lead halide perovskites by photon recycling and light out-coupling,” *Nature Communications*, vol. 7, pp. 13941 (1–8), 2016.

[45] N. Anttu, P. Kivisaari, and Y. Chen, “Tailored emission to boost open-circuit voltage in solar cells,” *Journal of Physics Communications*, vol. 3, no. 5, pp. 055009.1 – 055009.14, 2019.

[46] S. A. Mann, R. R. Grote, R. M. Osgood, A. Alù, and E. C. Garnett, “Opportunities and Limitations for Nanophotonic Structures to Exceed the Shockley-Queisser Limit,” *ACS Nano*, vol. 10, no. 9, pp. 8620–8631, 2016.

[47] S. Sandhu, Z. Yu, and S. Fan, “Detailed Balance Analysis and Enhancement of Open-Circuit Voltage in Single-Nanowire Solar Cells,” *Nano Letters*, vol. 1015, no. 2, pp. 1011 – 1015, 2014.

[48] U. Rau, “Reciprocity relation between photovoltaic quantum efficiency and electroluminescent emission of solar cells,” *Physical Review B - Condensed Matter and Materials Physics*, vol. 76, no. 8, pp. 085303 (1–8), 2007.

[49] I. L. Braly, R. J. Stoddard, A. Rajagopal, A. K. Jen, and H. W. Hillhouse, “Photoluminescence and Photoconductivity to Assess Maximum Open-Circuit Voltage and Carrier Transport in Hybrid Perovskites and Other Photovoltaic Materials,” *Journal of Physical Chemistry Letters*, vol. 9, no. 13, pp. 3779–3792, 2018.

[50] A. Delamarre, L. Lombez, and J. F. Guillemoles, “Contactless mapping of saturation currents of solar cells by photoluminescence,” *Applied Physics Letters*, vol. 100, no. 13, pp. 2012–2015, 2012.

[51] ESMAP, “Global Solar Atlas,” *Data obtained from the Global Solar Atlas 2.0, a free, web-based application is developed and operated by the company Solargis s.r.o. on behalf of the World Bank Group, utilizing Solargis data, with funding provided by the Energy Sector Management Assist.*, 2019.

[52] T. Kraus, O. Höhn, H. Hauser, and B. Bläsi, “Optoelectronic simulation of GaAs solar cells with angularly selective filters,” *Journal of Applied Physics*, vol. 115, no. 5, 2014.

[53] E. D. Kosten, B. M. Kayes, and H. A. Atwater, “Experimental demonstration of enhanced photon recycling in angle-restricted GaAs solar cells,” *Energy and Environmental Science*, vol. 7, no. 6, pp. 1907–1912, 2014.

[54] M. Peters, J. C. Goldschmidt, and B. Bläsi, “Angular confinement and concentration in photovoltaic converters,” *Solar Energy Materials and Solar Cells*, vol. 94, no. 8, pp. 1393–1398, 2010.

[55] C. Ulbrich, S. Fahr, J. Üpping, M. Peters, T. Kirchartz, C. Rockstuhl, R. Wehrspohn, A. Gombert, F. Lederer, and U. Rau, “Directional selectivity and ultra-light-trapping in solar cells,” *Physica Status Solidi (A) Applications and Materials Science*, vol. 205, no. 12, pp. 2831–2843, 2008.

[56] R. Quidant, N. F. V. Hulst, A. G. Curto, G. Volpe, T. H. Taminiau, and M. P. Kreuzer, “Unidirectional Emission of a Quantum Dot Coupled to a Nanoantenna,” *Science*, vol. 329, pp. 930–933kho, 2010.

[57] H. Aouani, O. Mahboub, E. Devaux, H. Rigneault, T. W. Ebbesen, and J. Wenger, “Plasmonic antennas for directional sorting of fluorescence emission,” *Nano Letters*, vol. 11, no. 6, pp. 2400–2406, 2011.

[58] G. Lozano, D. J. Louwers, S. R. K. Rodríguez, S. Murai, O. T. A. Jansen, M. A. Verschuuren, and J. Gómez Rivas, “Plasmonics for solid-state lighting: Enhanced excitation and directional emission of highly efficient light sources,” *Light: Science and Applications*, vol. 2, pp. e66(2013)(1–7), 2013.

[59] N. Yu and F. Capasso, “Flat optics with designer metasurfaces,” *Nature Materials*, vol. 13, no. 2, pp. 139–150, 2014.

[60] A. E. Krasnok, A. E. Miroshnichenko, P. A. Belov, and Y. S. Kivshar, “All-dielectric optical nanoantennas.,” *Optics Express*, vol. 20, no. 18, pp. 20599–20604, 2012.

[61] S. K. Andersen, S. Bogdanov, O. Makarova, Y. Xuan, M. Y. Shalaginov, A. Boltasseva, S. I. Bozhevolnyi, and V. M. Shalaev, “Hybrid Plasmonic Bullseye Antennas for Efficient Photon Collection,” *ACS Photonics*, vol. 5, no. 3, pp. 692–698, 2018.

[62] D. S. Filonov, A. E. Krasnok, A. P. Slobozhanyuk, P. V. Kapitanova, E. A. Nenasheva, Y. S. Kivshar, and P. A. Belov, “Experimental verification of the concept of all-dielectric nanoantennas,” *Applied Physics Letters*, vol. 100, no. 20, pp. 1–5, 2012.

[63] M. Khorasaninejad and F. Capasso, “Metalenses: Versatile multifunctional photonic components,” *Science*, vol. 358, no. 6367, pp. eaam8100 (1–8), 2017.

[64] H. A. Atwater and A. Polman, "Plasmonics for improved photovoltaic devices," *Nature Materials*, vol. 9, no. 3, pp. 205–213, 2010.

[65] E. Johlin, S. A. Mann, S. Kasture, A. F. Koenderink, and E. C. Garnett, "Broadband highly directive 3D nanophotonic lenses," *Nature Communications*, vol. 9, pp. 4742 (1–8), 2018.

[66] T. Holtus, L. Helmbrecht, H. C. Hendrikse, I. Baglai, S. Meuret, G. W. Adhyaksa, E. C. Garnett, and W. L. Noorduin, "Shape-preserving transformation of carbonate minerals into lead halide perovskite semiconductors based on ion exchange/insertion reactions," *Nature Chemistry*, vol. 10, no. 7, pp. 740–745, 2018.

[67] R. Scott, J. Heckmann, A. V. Prudnikau, A. Antanovich, A. Mikhailov, N. Owschimikow, M. Artemyev, J. I. Climente, U. Woggon, N. B. Grosse, and A. W. Achtstein, "Directed emission of CdSe nanoplatelets originating from strongly anisotropic 2D electronic structure," *Nature Nanotechnology*, vol. 12, pp. 1155–1161, 2017.

[68] A. Fieramosca, L. De Marco, M. Passoni, L. Polimeno, A. Rizzo, B. L. Rosa, G. Cruciani, L. Dominici, M. De Giorgi, G. Gigli, L. C. Andreani, D. Gerace, D. Ballarini, and D. Sanvitto, "Tunable Out-of-Plane Excitons in 2D Single-Crystal Perovskites," *ACS Photonics*, vol. 5, no. 10, pp. 4179–4185, 2018.

[69] D. R. Needell, O. Ilic, C. R. Bukowsky, Z. Nett, L. Xu, J. He, H. Bauser, B. G. Lee, J. F. Geisz, R. G. Nuzzo, A. P. Alivisatos, and H. A. Atwater, "Design criteria for micro-optical tandem luminescent solar concentrators," *IEEE Journal of Photovoltaics*, vol. 8, no. 6, pp. 1560–1567, 2018.

[70] K. Wu, H. Li, and V. I. Klimov, "Tandem luminescent solar concentrators based on engineered quantum dots," *Nature Photonics*, vol. 12, no. 2, pp. 105–110, 2018.

[71] J. C. Goldschmidt, M. Peters, J. Gutmann, L. Steidl, R. Zentel, B. Bläsi, and M. Hermle, "Increasing fluorescent concentrator light collection efficiency by restricting the angular emission characteristic of the incorporated luminescent material: the 'Nano-Fluko' concept," *Photonics for Solar Energy Systems III*, p. 77250S, 2010.

[72] B. Ehrler, K. P. Musselman, M. L. Böhm, R. H. Friend, and N. C. Greenham, "Hybrid pentacene/a-silicon solar cells utilizing multiple carrier generation via singlet exciton fission," *Applied Physics Letters*, vol. 101, no. 15, 2012.

[73] T. Kirchartz and U. Rau, "Modeling charge carrier collection in multiple exciton generating PbSe quantum dots," *Thin Solid Films*, vol. 517, no. 7, pp. 2438–2442, 2009.

[74] M. Li, R. Begum, J. Fu, Q. Xu, T. M. Koh, S. A. Veldhuis, M. Grätzel, N. Mathews, S. Mhaisalkar, and T. C. Sum, "Low threshold and efficient multiple exciton generation in halide perovskite nanocrystals," *Nature Communications*, vol. 9, pp. 4197 (1–9), 2018.

[75] C. de Weerd, L. Gomez, A. Capretti, D. M. Lebrun, E. Matsubara, J. Lin, M. Ashida, F. C. Spoor, L. D. Siebbeles, A. J. Houtepen, K. Suenaga, Y. Fujiwara, and T. Gregorkiewicz, "Efficient carrier multiplication in $CsPbI_3$ perovskite nanocrystals," *Nature Communications*, vol. 9, pp. 4199 (1–9), 2018.

[76] A. Dorodnyy, E. Alarcon-Lladó, V. Shklover, C. Hafner, A. Fontcuberta I Morral, and J. Leuthold, “Efficient Multiterminal Spectrum Splitting via a Nanowire Array Solar Cell,” *ACS Photonics*, vol. 2, no. 9, pp. 1284–1288, 2015.

[77] S. A. Mann and E. C. Garnett, “Resonant nanophotonic spectrum splitting for ultrathin multijunction solar cells,” *ACS Photonics*, vol. 2, no. 7, pp. 816–821, 2015.

[78] A. Andreas and T. Stoffel, “NREL Solar Radiation Research Laboratory (SRRL): Baseline Measurement System (BMS); Golden, Colorado (Data),” *NREL Report No. DA-5500-56488.*, 1981.

[79] T. S. Liang, M. Pravettoni, C. Deline, J. S. Stein, R. Kopecek, J. P. Singh, W. Luo, Y. Wang, A. G. Aberle, and Y. S. Khoo, “A review of crystalline silicon bifacial photovoltaic performance characterisation and simulation,” *Energy and Environmental Science*, vol. 12, pp. 116–148, 2019.

[80] L. Novotny and B. Hecht, *Principles of nano-optics.* Cambridge: Cambridge University Press, 2009.

[81] S. Gorsky, R. Zhang, A. Gok, R. Wang, K. Kebede, A. Lenef, M. Raukas, and L. Dal Negro, “Directional light emission enhancement from LED-phosphor converters using dielectric Vogel spiral arrays,” *APL Photonics*, vol. 3, no. 12, pp. 126103 (1–12), 2018.

[82] S. Gorsky, W. A. Britton, Y. Chen, J. Montaner, A. Lenef, M. Raukas, and L. Dal Negro, “Engineered hyperuniformity for directional light extraction,” *APL Photonics*, vol. 4, no. 11, pp. 110801 (1–13), 2019.

[83] E. Khaidarov, Z. Liu, R. Paniagua-Domínguez, S. T. Ha, V. Valuckas, X. Liang, Y. Akimov, P. Bai, C. E. Png, H. V. Demir, and A. I. Kuznetsov, “Control of LED Emission with Functional Dielectric Metasurfaces,” *Laser and Photonics Reviews*, vol. 14, pp. 1900235 (1–8), 2020.

[84] Y. Sun, V. Yaroshenko, A. Chebykin, E. Ageev, S. Makarov, and D. Zuev, “Metal-dielectric nanoantenna for radiation control of a single-photon emitter,” *Optical Materials Express*, vol. 10, no. 1, pp. 29–35, 2020.

[85] H. Y. D. Yang, N. G. Alexopoulos, and E. Yablonovitch, “Photonic band-gap materials for high-gain printed circuit antennas,” *IEEE Transactions on Antennas and Propagation*, vol. 45, no. 1, pp. 185–187, 1997.

[86] Z. Li, K. Aydin, and E. Ozbay, “Highly directional emission from photonic crystals with a wide bandwidth,” *Applied Physics Letters*, vol. 91, no. 12, pp. 89–92, 2007.

[87] J. S. Van Der Burgt and E. C. Garnett, “Nanophotonic Emission Control for Improved Photovoltaic Efficiency,” *ACS Photonics*, vol. 7, no. 7, pp. 1589–1602, 2020.

[88] L. Novotny and N. Van Hulst, “Antennas for light,” *Nature Photonics*, vol. 5, no. 2, pp. 83–90, 2011.

[89] M. Decker and I. Staude, “Resonant dielectric nanostructures: A low-loss platform for functional nanophotonics,” *Journal of Optics (United Kingdom)*, vol. 18, no. 10, pp. 1–31, 2016.

[90] H. C. Kim, H. Ko, and M. Cheng, “High efficient optical focusing of a zone plate composed of metal/dielectric multilayer,” *Optics Express*, vol. 17, no. 5, pp. 3078–3083, 2009.

[91] B. R. Lu, J. X. Li, H. B. Guo, C. Gao, E. Huq, X. P. Qu, Y. Chen, and R. Liu, “Dielectric Fresnel zone plates on optical fibers for micro-focusing applications,” *Microelectronic Engineering*, vol. 88, no. 8, pp. 2650–2652, 2011.

[92] A. Vaskin, R. Kolkowski, A. F. Koenderink, and I. Staude, “Light-emitting metasurfaces,” *Nanophotonics*, vol. 8, no. 7, pp. 1151–1198, 2019.

[93] P. P. Iyer, R. A. DeCrescent, Y. Mohtashami, G. Lheureux, N. A. Butakov, A. Alhassan, C. Weisbuch, S. Nakamura, S. P. DenBaars, and J. A. Schuller, “Unidirectional luminescence from InGaN/GaN quantum-well metasurfaces,” *Nature Photonics*, vol. 14, no. 9, pp. 543–548, 2020.

[94] T. Y. Huang, R. R. Grote, S. A. Mann, D. A. Hopper, A. L. Exarhos, G. G. Lopez, E. C. Garnett, and L. C. Bassett, “A monolithic immersion metalens for imaging solid-state quantum emitters,” *Nature Communications*, vol. 10, pp. 2392(1–8), 2019.

[95] M. Kamp, B. de Nijs, N. Kongsuwan, M. Saba, R. Chikkaraddy, C. A. Readman, W. M. Deacon, J. Griffiths, S. J. Barrow, O. S. Ojambati, D. Wright, J. Huang, O. Hess, O. A. Scherman, and J. J. Baumberg, “Cascaded nanooptics to probe microsecond atomic-scale phenomena,” *Proceedings of the National Academy of Sciences of the United States of America*, vol. 117, no. 26, pp. 14819–14826, 2020.

[96] A. E. Krasnok, A. Maloshtan, D. N. Chigrin, Y. S. Kivshar, and P. A. Belov, “Enhanced emission extraction and selective excitation of NV centers with all-dielectric nanoantennas,” *Laser and Photonics Reviews*, vol. 9, no. 4, pp. 385–391, 2015.

[97] E. Rusak, I. Staude, M. Decker, J. Sautter, A. E. Miroshnichenko, D. A. Powell, D. N. Neshev, and Y. S. Kivshar, “Hybrid nanoantennas for directional emission enhancement,” *Applied Physics Letters*, vol. 105, no. 22, pp. 221109 (1–5), 2014.

[98] A. Bonakdar and H. Mohseni, “Hybrid optical antenna with high directivity gain,” *Optics Letters*, vol. 38, no. 15, pp. 2726 – 2728, 2013.

[99] M. Peter, A. Hildebrandt, C. Schlickriede, K. Gharib, T. Zentgraf, J. Förstner, and S. Linden, “Directional Emission from Dielectric Leaky-Wave Nanoantennas,” *Nano Letters*, vol. 17, no. 7, pp. 4178–4183, 2017.

[100] J. Ho, Y. H. Fu, Z. Dong, R. Paniagua-Dominguez, E. H. Koay, Y. F. Yu, V. Valuckas, A. I. Kuznetsov, and J. K. Yang, “Highly directive hybrid metal-dielectric yagi-uda nanoantennas,” *ACS Nano*, vol. 12, no. 8, pp. 8616–8624, 2018.

[101] J. H. Atwater, P. Spinelli, E. Kosten, J. Parsons, C. Van Lare, J. Van De Groep, J. Garcia De Abajo, A. Polman, and H. A. Atwater, “Microphotonic parabolic light directors fabricated by two-photon lithography,” *Applied Physics Letters*, vol. 99, pp. 151113 (1–3), oct 2011.

[102] A. Bogucki, Ł. Zinkiewicz, M. Grzeszczyk, W. Pacuski, K. Nogajewski, T. Kazimierczuk, A. Rodek, J. Suffczyński, K. Watanabe, T. Taniguchi, P. Wasylczyk, M. Potemski, and P. Kossacki, “Ultra-long-working-distance spectroscopy of single nanostructures with aspherical solid immersion microlenses,” *Light: Science and Applications*, vol. 9, no. 1, pp. 48 (1–11), 2020.

[103] S. Molesky, Z. Lin, A. Y. Piggott, W. Jin, J. Vucković, and A. W. Rodriguez, “Inverse design in nanophotonics,” *Nature Photonics*, vol. 12, no. 11, pp. 659–670, 2018.

[104] J. S. Jensen and O. Sigmund, “Topology optimization for nano-photonics,” *Laser and Photonics Reviews*, vol. 5, no. 2, pp. 308–321, 2011.

[105] J. Lu and J. Vučković, “Nanophotonic computational design,” *Optics Express*, vol. 21, no. 11, pp. 13351–13367, 2013.

[106] S. Yu, C. Wang, C. Sun, and W. Chen, “Topology optimization for light-trapping structure in solar cells,” *Structural and Multidisciplinary Optimization*, vol. 50, no. 3, pp. 367–382, 2014.

[107] C. D. Dieleman, W. Ding, L. Wu, N. Thakur, I. Bespalov, B. Daiber, Y. Ekinci, S. Castellanos, and B. Ehrler, “Universal direct patterning of colloidal quantum dots by (extreme) ultraviolet and electron beam lithography,” *Nanoscale*, vol. 12, no. 20, pp. 11306–11316, 2020.

[108] T. Gissibl, S. Thiele, A. Herkommer, and H. Giessen, “Two-photon direct laser writing of ultracompact multi-lens objectives,” *Nature Photonics*, vol. 10, no. 8, pp. 554–560, 2016.

[109] V. Neder, Y. Ra’Di, A. Alù, and A. Polman, “Combined Metagratings for Efficient Broad-Angle Scattering Metasurface,” *ACS Photonics*, vol. 6, no. 4, pp. 1010–1017, 2019.

[110] J. B. Mueller, J. Fischer, Y. J. Mange, T. Nann, and M. Wegener, “In-situ local temperature measurement during three-dimensional direct laser writing,” *Applied Physics Letters*, vol. 103, no. 12, pp. 123107(1–4), 2013.

[111] J. Fischer, J. B. Mueller, J. Kaschke, T. J. A. Wolf, A.-N. Unterreiner, and M. Wegener, “Three-dimensional multi-photon direct laser writing with variable repetition rate,” *Optics Express*, vol. 21, no. 22, pp. 26244–26260, 2013.

[112] Z. Andaji-Garmaroudi, M. Anaya, A. J. Pearson, and S. D. Stranks, “Photobrightening in Lead Halide Perovskites: Observations, Mechanisms, and Future Potential,” *Advanced Energy Materials*, vol. 10, no. 13, pp. 1–12, 2020.

[113] D. A. Hanifi, N. D. Bronstein, B. A. Koscher, Z. Nett, J. K. Swabeck, K. Takano, A. M. Schwartzberg, L. Maserati, K. Vandewal, Y. van de Burgt, A. Salleo, and A. P. Alivisatos, “Redefining near-unity luminescence in quantum dots with photothermal threshold quantum yield,” *Science*, vol. 363, no. 6432, pp. 1199–1202, 2019.

[114] O. Chen, J. Zhao, V. P. Chauhan, J. Cui, C. Wong, D. K. Harris, H. Wei, H. S. Han, D. Fukumura, R. K. Jain, and M. G. Bawendi, "Compact high-quality CdSe-CdS core-shell nanocrystals with narrow emission linewidths and suppressed blinking," *Nature Materials*, vol. 12, pp. 445–451, may 2013.

[115] K. Boldt, N. Kirkwood, G. A. Beane, and P. Mulvaney, "Synthesis of highly luminescent and photo-stable, graded shell CdSe/$Cd_xZn_{1-x}S$ nanoparticles by in situ alloying," *Chemistry of Materials*, vol. 25, no. 23, pp. 4731–4738, 2013.

[116] T. Sikanen, S. Aura, L. Heikkilä, T. Kotiaho, S. Franssila, and R. Kostiainen, "Hybrid ceramic polymers: New, nonbiofouling, and optically transparent materials for microfluidics," *Analytical Chemistry*, vol. 82, no. 9, pp. 3874–3882, 2010.

[117] J. Purtov, A. Verch, P. Rogin, and R. Hensel, "Improved development procedure to enhance the stability of microstructures created by two-photon polymerization," *Microelectronic Engineering*, vol. 194, pp. 45–50, 2018.

[118] S. A. Mann, B. Sciacca, Y. Zhang, J. Wang, E. Kontoleta, H. Liu, and E. C. Garnett, "Integrating Sphere Microscopy for Direct Absorption Measurements of Single Nanostructures," *ACS Nano*, vol. 11, no. 2, pp. 1412–1418, 2017.

[119] Q. A. Akkerman and L. Manna, "What Defines a Halide Perovskite?," *ACS Energy Letters*, vol. 5, no. 2, pp. 604–610, 2020.

[120] Z. Li, T. R. Klein, D. H. Kim, M. Yang, J. J. Berry, M. F. Van Hest, and K. Zhu, "Scalable fabrication of perovskite solar cells," *Nature Reviews Materials*, vol. 3, p. 18017, mar 2018.

[121] W. Nie, H. Tsai, R. Asadpour, J. C. Blancon, A. J. Neukirch, G. Gupta, J. J. Crochet, M. Chhowalla, S. Tretiak, M. A. Alam, H. L. Wang, and A. D. Mohite, "High-efficiency solution-processed perovskite solar cells with millimeter-scale grains," *Science*, vol. 347, pp. 522–525, jan 2015.

[122] W. Nie, J. C. Blancon, A. J. Neukirch, K. Appavoo, H. Tsai, M. Chhowalla, M. A. Alam, M. Y. Sfeir, C. Katan, J. Even, S. Tretiak, J. J. Crochet, G. Gupta, and A. D. Mohite, "Light-activated photocurrent degradation and self-healing in perovskite solar cells," *Nature Communications*, vol. 7, p. 11574, 2016.

[123] E. Bi, Z. Song, C. Li, Z. Wu, and Y. Yan, "Mitigating ion migration in perovskite solar cells," *Trends in Chemistry*, vol. 3, no. 7, pp. 575–588, 2021.

[124] S. S. Mali, J. V. Patil, H. Arandiyan, R. Luque, and C. K. Hong, "Editors' Choice—Stability of Unstable Perovskites: Recent Strategies for Making Stable Perovskite Solar Cells," *ECS Journal of Solid State Science and Technology*, vol. 8, pp. Q111–Q117, 2019.

[125] J. A. Christians, S. N. Habisreutinger, J. J. Berry, and J. M. Luther, "Stability in Perovskite Photovoltaics: A Paradigm for Newfangled Technologies," *ACS Energy Letters*, vol. 3, no. 9, pp. 2136–2143, 2018.

[126] A. J. Knight, A. D. Wright, J. B. Patel, D. P. McMeekin, H. J. Snaith, M. B. Johnston, and L. M. Herz, “Electronic Traps and Phase Segregation in Lead Mixed-Halide Perovskite,” *ACS Energy Letters*, vol. 4, pp. 75–84, 2019.

[127] Y. Zhong, C. A. M. Luna, R. Hildner, C. Li, and S. Huettner, “In situ investigation of light soaking in organolead halide perovskite films,” *APL Materials*, vol. 7, p. 041114, apr 2019.

[128] A. J. Barker, A. Sadhanala, F. Deschler, M. Gandini, S. P. Senanayak, P. M. Pearce, E. Mosconi, A. J. Pearson, Y. Wu, A. R. Srimath Kandada, T. Leijtens, F. De Angelis, S. E. Dutton, A. Petrozza, and R. H. Friend, “Defect-Assisted Photoinduced Halide Segregation in Mixed-Halide Perovskite Thin Films,” *ACS Energy Letters*, vol. 2, pp. 1416–1424, jun 2017.

[129] E. T. Hoke, D. J. Slotcavage, E. R. Dohner, A. R. Bowring, H. I. Karunadasa, and M. D. McGehee, “Reversible photo-induced trap formation in mixed-halide hybrid perovskites for photovoltaics,” *Chemical Science*, vol. 6, no. 1, pp. 613–617, 2015.

[130] S. Mahesh, J. M. Ball, R. D. Oliver, D. P. McMeekin, P. K. Nayak, M. B. Johnston, and H. J. Snaith, “Revealing the origin of voltage loss in mixed-halide perovskite solar cells,” *Energy and Environmental Science*, vol. 13, no. 1, pp. 258–267, 2020.

[131] A. J. Knight and L. M. Herz, “Preventing phase segregation in mixed-halide perovskites: A perspective,” *Energy and Environmental Science*, vol. 13, pp. 2024–2046, jul 2020.

[132] J. S. Van Der Burgt, C. D. Dieleman, E. Johlin, J. J. Geuchies, A. J. Houtepen, B. Ehrler, and E. C. Garnett, “Integrating Sphere Fourier Microscopy of Highly Directional Emission,” *ACS Photonics*, vol. 8, no. 4, pp. 1143–1151, 2021.

[133] S. J. Lachman, “Learning is a process: Toward an improved definition of learning,” *Journal of Psychology: Interdisciplinary and Applied*, vol. 131, pp. 477–480, sep 1997.

[134] J. de Houwer, D. Barnes-Holmes, and A. Moors, “What is learning? On the nature and merits of a functional definition of learning,” *Psychonomic Bulletin and Review*, vol. 20, no. 4, pp. 631–642, 2013.

[135] C. Kaspar, B. J. Ravoo, W. G. van der Wiel, S. V. Wegner, and W. H. Pernice, “The rise of intelligent matter,” *Nature*, vol. 594, no. 7863, pp. 345–355, 2021.

[136] A. Walther, “Viewpoint: From Responsive to Adaptive and Interactive Materials and Materials Systems: A Roadmap,” *Advanced Materials*, vol. 32, no. 20, 2020.

[137] R. Merindol and A. Walther, “Materials learning from life: Concepts for active, adaptive and autonomous molecular systems,” *Chemical Society Reviews*, vol. 46, no. 18, pp. 5588–5619, 2017.

[138] Z. Wang, J. Wang, J. Ayarza, T. Steeves, Z. Hu, S. Manna, and A. P. Esser-Kahn, “Bio-inspired mechanically adaptive materials through vibration-induced crosslinking,” *Nature Materials*, vol. 20, no. 6, pp. 869–874, 2021.

[139] M. L. De Giorgi, S. Milanese, A. Klini, and M. Anni, "Environment-induced reversible modulation of optical and electronic properties of lead halide perovskites and possible applications to sensor development: A review," *Molecules*, vol. 26, no. 3, 2021.

[140] M. Yuan, L. N. Quan, R. Comin, G. Walters, R. Sabatini, O. Voznyy, S. Hoogland, Y. Zhao, E. M. Beauregard, P. Kanjanaboos, Z. Lu, D. H. Kim, and E. H. Sargent, "Perovskite energy funnels for efficient light-emitting diodes," *Nature Nanotechnology*, vol. 11, no. 10, pp. 872–877, 2016.

[141] J. S. Yun, J. Seidel, J. Kim, A. M. Soufiani, S. Huang, J. Lau, N. J. Jeon, S. I. Seok, M. A. Green, and A. Ho-Baillie, "Critical Role of Grain Boundaries for Ion Migration in Formamidinium and Methylammonium Lead Halide Perovskite Solar Cells," *Advanced Energy Materials*, vol. 6, no. 13, pp. 1–8, 2016.

[142] D. J. Slotcavage, H. I. Karunadasa, and M. D. McGehee, "Light-Induced Phase Segregation in Halide-Perovskite Absorbers," 2016.

[143] W. Mao, C. R. Hall, A. S. Chesman, C. Forsyth, Y. B. Cheng, N. W. Duffy, T. A. Smith, and U. Bach, "Visualizing Phase Segregation in Mixed-Halide Perovskite Single Crystals," *Angewandte Chemie - International Edition*, vol. 58, no. 9, pp. 2893–2898, 2019.

[144] H. H. Fang, S. Adjokatse, H. Wei, J. Yang, G. R. Blake, J. Huang, J. Even, and M. A. Loi, "Ultrahigh sensitivity of methylammonium lead tribromide perovskite single crystals to environmental gases," *Science Advances*, vol. 2, no. 7, pp. 1–10, 2016.

[145] T. Hirvikorpi, M. Vähä-Nissi, T. Mustonen, E. Iiskola, and M. Karppinen, "Atomic layer deposited aluminum oxide barrier coatings for packaging materials," *Thin Solid Films*, vol. 518, pp. 2654–2658, mar 2010.

[146] "Best Research-Cell Efficiency Chart | Photovoltaic Research | NREL."

[147] A. K. Jena, A. Kulkarni, and T. Miyasaka, "Halide Perovskite Photovoltaics: Background, Status, and Future Prospects," *Chemical Reviews*, vol. 119, no. 5, pp. 3036–3103, 2019.

[148] W. J. Yin, T. Shi, and Y. Yan, "Unique properties of halide perovskites as possible origins of the superior solar cell performance," *Advanced Materials*, vol. 26, no. 27, pp. 4653–4658, 2014.

[149] S. Sun, T. Salim, N. Mathews, M. Duchamp, C. Boothroyd, G. Xing, T. C. Sum, and Y. M. Lam, "The origin of high efficiency in low-temperature solution-processable bilayer organometal halide hybrid solar cells," *Energy and Environmental Science*, vol. 7, no. 1, pp. 399–407, 2014.

[150] J. H. Noh, S. H. Im, J. H. Heo, T. N. Mandal, and S. I. Seok, "Chemical management for colorful, efficient, and stable inorganic-organic hybrid nanostructured solar cells," *Nano Letters*, vol. 13, no. 4, pp. 1764–1769, 2013.

[151] A. F. Gualdrón-Reyes, S. J. Yoon, and I. Mora-Seró, "Recent insights for achieving mixed halide perovskites without halide segregation," *Current Opinion in Electrochemistry*, vol. 11, pp. 84–90, oct 2018.

[152] K. W. Allen, A. Darafsheh, and V. N. Astratov, “Photonic nanojet-induced modes: From physics to applications,” in *International Conference on Transparent Optical Networks*, 2011.

[153] B. S. Luk’yanchuk, R. Paniagua-Domínguez, I. Minin, O. Minin, and Z. Wang, “Refractive index less than two: photonic nanojets yesterday, today and tomorrow [Invited],” *Optical Materials Express*, vol. 7, no. 6, p. 1820, 2017.

[154] W. Stöber, A. Fink, and E. Bohn, “Controlled growth of monodisperse silica spheres in the micron size range,” *Journal of Colloid And Interface Science*, vol. 26, pp. 62–69, jan 1968.

[155] C. Park, T. Lee, Y. Xia, T. J. Shin, J. Myoung, and U. Jeong, “Quick, large-area assembly of a single-crystal monolayer of spherical particles by unidirectional rubbing,” *Advanced Materials*, vol. 26, no. 27, pp. 4633–4638, 2014.

[156] J. Wong, S. T. Omelchenko, and H. A. Atwater, “Impact of Semiconductor Band Tails and Band Filling on Photovoltaic Efficiency Limits,” *ACS Energy Letters*, vol. 6, pp. 52–57, jan 2021.

[157] P. Löper, M. Stuckelberger, B. Niesen, J. Werner, M. Filipič, S. J. Moon, J. H. Yum, M. Topič, S. De Wolf, and C. Ballif, “Complex refractive index spectra of CH3NH3PbI3 perovskite thin films determined by spectroscopic ellipsometry and spectrophotometry,” *Journal of Physical Chemistry Letters*, vol. 6, no. 1, pp. 66–71, 2015.

[158] M. T. Hörantner and H. J. Snaith, “Predicting and optimising the energy yield of perovskite-on-silicon tandem solar cells under real world conditions,” *Energy and Environmental Science*, vol. 10, pp. 1983–1993, sep 2017.

[159] D. P. McMeekin, G. Sadoughi, W. Rehman, G. E. Eperon, M. Saliba, M. T. Hörantner, A. Haghighirad, N. Sakai, L. Korte, B. Rech, M. B. Johnston, L. M. Herz, and H. J. Snaith, “A mixed-cation lead mixed-halide perovskite absorber for tandem solar cells,” *Science*, vol. 351, pp. 151–155, jan 2016.

[160] T. A. König, P. A. Ledin, J. Kerszulis, M. A. Mahmoud, M. A. El-Sayed, J. R. Reynolds, and V. V. Tsukruk, “Electrically tunable plasmonic behavior of nanocube-polymer nanomaterials induced by a redox-active electrochromic polymer,” *ACS Nano*, vol. 8, no. 6, pp. 6182–6192, 2014.

[161] M. S. Rahman, S. Miah, M. S. W. Marma, and T. Sabrina, “Simulation based Investigation of Inverted Planar Perovskite Solar Cell with All Metal Oxide Inorganic Transport Layers,” in *2nd International Conference on Electrical, Computer and Communication Engineering, ECCE 2019*, Institute of Electrical and Electronics Engineers Inc., apr 2019.

[162] BP, “Stratistical Review of World Energy,” *Statistical Review of World Energy 2020*, vol. 69, pp. 1–56, 2020.

[163] Enerdata, *Global Energy Statistical Yearbook 2021.* Enerdata, 2021.

[164] P. Bonato, R. Fedrizzi, M. D'Antoni, and M. Meir, "State-of-the-art and SWOT analysis of building integrated solar envelope systems," tech. rep., IEA, nov 2019.

[165] R. J. Yang and P. X. Zou, "Building integrated photovoltaics (BIPV): Costs, benefits, risks, barriers and improvement strategy," *International Journal of Construction Management*, vol. 16, pp. 39–53, jan 2016.

[166] T. E. Kuhn, C. Erban, M. Heinrich, J. Eisenlohr, F. Ensslen, and D. H. Neuhaus, "Review of technological design options for building integrated photovoltaics (BIPV)," *Energy and Buildings*, vol. 231, p. 110381, sep 2021.

[167] M. Kryszak and L. W. Wang, "The value of aesthetics in the BIPV roof products segment: a multiperspective study under European market conditions," *Energy Sources, Part A: Recovery, Utilization and Environmental Effects*, pp. 1–22, aug 2020.

[168] R. R. Lunt and V. Bulovic, "Transparent, near-infrared organic photovoltaic solar cells for window and energy-scavenging applications," *Applied Physics Letters*, vol. 98, p. 113305, mar 2011.

[169] C. J. Traverse, R. Pandey, M. C. Barr, and R. R. Lunt, "Emergence of highly transparent photovoltaics for distributed applications," *Nature Energy*, vol. 2, no. 11, pp. 849–860, 2017.

[170] A. A. Husain, W. Z. W. Hasan, S. Shafie, M. N. Hamidon, and S. S. Pandey, "A review of transparent solar photovoltaic technologies," *Renewable and Sustainable Energy Reviews*, vol. 94, no. January 2017, pp. 779–791, 2018.

[171] C. Lamnatou and D. Chemisana, "Solar radiation manipulations and their role in greenhouse claddings: Fluorescent solar concentrators, photoselective and other materials," *Renewable and Sustainable Energy Reviews*, vol. 27, pp. 175–190, 2013.

[172] W. H. Weber and J. Lambe, "Luminescent greenhouse collector for solar radiation," *Applied Optics*, vol. 15, no. 10, p. 2299, 1976.

[173] C. Corrado, S. W. Leow, M. Osborn, I. Carbone, K. Hellier, M. Short, G. Alers, and S. A. Carter, "Power generation study of luminescent solar concentrator greenhouse," *Journal of Renewable and Sustainable Energy*, vol. 8, p. 043502, jul 2016.

[174] M. E. Loik, S. A. Carter, G. Alers, C. E. Wade, D. Shugar, C. Corrado, D. Jokerst, and C. Kitayama, "Wavelength-Selective Solar Photovoltaic Systems: Powering Greenhouses for Plant Growth at the Food-Energy-Water Nexus," *Earth's Future*, vol. 5, no. 10, pp. 1044–1053, 2017.

[175] E. Cuce, D. Harjunowibowo, and P. M. Cuce, "Renewable and sustainable energy saving strategies for greenhouse systems: A comprehensive review," *Renewable and Sustainable Energy Reviews*, vol. 64, pp. 34–59, 2016.

[176] R. Fu, D. Feldman, and R. Margolis, "U.S. Solar Photovoltaic System Cost Benchmark: Q1 2018," tech. rep., CO: National Renewable Energy Laboratory. NREL/TP-6A20-72399, 2018.

[177] W. A. Shurcliff and R. C. Jones, “The Trapping of Fluorescent Light Produced within Objects of High Geometrical Symmetry,” *Journal of the Optical Society of America*, vol. 39, no. 11, p. 912, 1949.

[178] E. Yablonovitch, “Thermodyamics of the Fluorescent Planar Concentrator.,” *Journal of the Optical Society of America*, vol. 70, no. 11, pp. 1362–1363, 1980.

[179] A. Rabl, “Comparison of solar concentrators,” *Solar Energy*, vol. 18, no. 2, pp. 93–111, 1976.

[180] M. G. Debije and V. A. Rajkumar, “Direct versus indirect illumination of a prototype luminescent solar concentrator,” *Solar Energy*, vol. 122, pp. 334–340, 2015.

[181] Y. Li, Y. Sun, and Y. Zhang, “Luminescent solar concentrators performing under different light conditions,” *Solar Energy*, vol. 188, pp. 1248–1255, 2019.

[182] V. A. Rajkumar, C. Weijers, and M. G. Debije, “Distribution of absorbed heat in luminescent solar concentrator lightguides and effect on temperatures of mounted photovoltaic cells,” *Renewable Energy*, vol. 80, pp. 308–315, 2015.

[183] A. Reinders, R. Kishore, L. Slooff, and W. Eggink, “Luminescent solar concentrator photovoltaic designs,” in *Japanese Journal of Applied Physics*, vol. 57, p. 08RD10, aug 2018.

[184] P. Moraitis, G. van Leeuwen, and W. van Sark, “Visual appearance of nanocrystal-based luminescent solar concentrators,” *Materials*, vol. 16, no. 6, 2019.

[185] F. Meinardi, F. Bruni, and S. Brovelli, “Luminescent solar concentrators for building-integrated photovoltaics,” *Nature Reviews Materials*, vol. 2, pp. 1–9, 2017.

[186] A. Reinders, M. G. Debije, and A. Rosemann, “Measured Efficiency of a Luminescent Solar Concentrator PV Module Called Leaf Roof,” *IEEE Journal of Photovoltaics*, vol. 7, no. 6, pp. 1663–1666, 2017.

[187] J. A. Sol, G. H. Timmermans, A. J. van Breugel, A. P. Schenning, and M. G. Debije, “Multistate Luminescent Solar Concentrator “Smart” Windows,” *Advanced Energy Materials*, vol. 8, no. 12, pp. 1–8, 2018.

[188] S. M. Mopurisetty, M. Bajaj, and S. Ganguly, “TCAD calibration for Cu2ZnSnS4 solar cell simulation,” in *2017 IEEE 44th Photovoltaic Specialist Conference, PVSC 2017*, pp. 1737–1740, IEEE, jun 2017.

[189] D. R. Needell, C. R. Bukowsky, S. Darbe, H. Bauser, O. Ilic, and H. A. Atwater, “Spectrally Matched Quantum Dot Photoluminescence in GaAs-Si Tandem Luminescent Solar Concentrators,” *IEEE Journal of Photovoltaics*, vol. 9, pp. 397–401, mar 2019.

[190] M. M. Lunardi, D. R. Needell, H. Bauser, M. Phelan, H. A. Atwater, and R. Corkish, “Life Cycle Assessment of tandem LSC-Si devices,” *Energy*, vol. 181, pp. 1–10, aug 2019.

[191] M. G. Debije and P. P. Verbunt, “Thirty years of luminescent solar concentrator research: Solar energy for the built environment,” *Advanced Energy Materials*, vol. 2, no. 1, pp. 12–35, 2012.

[192] a. Goetzberger and W. Greube, “Solar energy conversion with fluorescent collectors,” *Applied Physics*, vol. 14, no. 2, pp. 123–139, 1977.

[193] C. Tummeltshammer, A. Taylor, A. J. Kenyon, and I. Papakonstantinou, “Losses in luminescent solar concentrators unveiled,” *Solar Energy Materials and Solar Cells*, vol. 144, pp. 40–47, 2016.

[194] a. R. Burgers, L. H. Slooff, R. Kinderman, and J. M. van Roosmalen, “Modelling of Luminescent Concentrators By Ray-Tracing,” *Presented at the 20th European Photovoltaic Solar Energy Conference and Exhibition*, pp. 394–397, 2005.

[195] B. C. Rowan, L. R. Wilson, and B. S. Richards, “Advanced material concepts for luminescent solar concentrators,” *IEEE Journal on Selected Topics in Quantum Electronics*, vol. 14, no. 5, pp. 1312–1322, 2008.

[196] A. L. Martínez and D. Gómez, “Design, fabrication, and characterization of a luminescent solar concentrator with optimized optical concentration through minimization of optical losses,” *Journal of Photonics for Energy*, vol. 6, no. 4, p. 045504, 2016.

[197] Z. Krumer, W. G. van Sark, R. E. Schropp, and C. de Mello Donegá, “Compensation of self-absorption losses in luminescent solar concentrators by increasing luminophore concentration,” *Solar Energy Materials and Solar Cells*, vol. 167, pp. 133–139, 2017.

[198] A. Kerrouche, D. A. Hardy, D. Ross, and B. S. Richards, “Luminescent solar concentrators: From experimental validation of 3D ray-tracing simulations to coloured stained-glass windows for BIPV,” *Solar Energy Materials and Solar Cells*, vol. 122, pp. 99–106, mar 2014.

[199] R. Connell, C. Pinnell, and V. E. Ferry, “Designing spectrally-selective mirrors for use in luminescent solar concentrators,” *Journal of Optics (United Kingdom)*, vol. 20, no. 2, 2018.

[200] L. H. Slooff, E. E. Bende, A. R. Burgers, T. Budel, M. Pravettoni, R. P. Kenny, E. D. Dunlop, and A. Büchtemann, “A Luminescent Solar Concentrator with 7.1% power conversion efficiency,” *Physica Status Solidi - Rapid Research Letters*, vol. 2, no. 6, pp. 257–259, 2008.

[201] M. G. Debije, R. C. Evans, and G. Griffini, “Laboratory protocols for measuring and reporting the performance of luminescent solar concentrators,” *Energy and Environmental Science*, vol. 14, no. 1, pp. 293–301, 2021.

[202] L. Xu, Y. Yao, N. D. Bronstein, L. Li, A. P. Alivisatos, and R. G. Nuzzo, “Enhanced Photon Collection in Luminescent Solar Concentrators with Distributed Bragg Reflectors,” *ACS Photonics*, vol. 3, no. 2, pp. 278–285, 2016.

[203] D. K. G. de Boer, D. J. Broer, M. G. Debije, W. Keur, A. Meijerink, C. R. Ronda, and P. P. C. Verbunt, “Progress in phosphors and filters for luminescent solar concentrators,” *Optics Express*, vol. 20, no. S3, p. A395, 2012.

[204] D. K. De Boer, L. Chi-Wen, M. P. Giesbers, H. J. Cornelissen, M. G. Debije, P. P. Verbunt, and D. J. Broer, “Polarization-independent filters for luminescent solar concentrators,” *Applied Physics Letters*, vol. 98, p. 021111, jan 2011.

[205] C. Tummeltshammer, A. Taylor, A. J. Kenyon, and I. Papakonstantinou, “Homeotropic alignment and Förster resonance energy transfer: The way to a brighter luminescent solar concentrator,” *Journal of Applied Physics*, vol. 116, no. 17, 2014.

[206] M. G. Debije, “Solar energy collectors with tunable transmission,” *Advanced Functional Materials*, vol. 20, no. 9, pp. 1498–1502, 2010.

[207] C. L. Mulder, P. D. Reusswig, A. P. Beyler, H. Kim, C. Rotschild, and M. A. Baldo, “Dye alignment in luminescent solar concentrators: II Horizontal alignment for energy harvesting in linear polarizers,” *Optics Express*, vol. 18, pp. A91–A99, apr 2010.

[208] H. C. Bauser, C. R. Bukowsky, M. Phelan, W. Weigand, D. R. Needell, Z. C. Holman, and H. A. Atwater, “Photonic Crystal Waveguides for >90Trapping Efficiency in Luminescent Solar Concentrators,” *ACS Photonics*, vol. 7, pp. 2122–2131, aug 2020.

[209] P. P. C. Verbunt, C. Sánchez-Somolinos, D. J. Broer, and M. G. Debije, “Anisotropic light emissions in luminescent solar concentrators–isotropic systems,” *Optics Express*, vol. 21, no. S3, pp. A485–A493, 2013.

[210] P. P. Verbunt, T. M. De Jong, D. K. De Boer, D. J. Broer, and M. G. Debije, “Anisotropic light emission from aligned luminophores,” *EPJ Applied Physics*, vol. 67, no. 1, pp. 1–7, 2014.

[211] P. P. Verbunt, A. Kaiser, K. Hermans, C. W. Bastiaansen, D. J. Broer, and M. G. Debije, “Controlling light emission in luminescent solar concentrators through use of dye molecules aligned in a planar manner by liquid crystals,” *Advanced Functional Materials*, vol. 19, no. 17, pp. 2714–2719, 2009.

[212] P. Moraitis, D. K. de Boer, P. T. Prins, C. de Mello Donegá, K. Neyts, and W. G. van Sark, “Should Anisotropic Emission or Reabsorption of Nanoparticle Luminophores Be Optimized for Increasing Luminescent Solar Concentrator Efficiency?,” *Solar RRL*, vol. 4, p. 2000279, oct 2020.

[213] H. Fang, C. Battaglia, C. Carraro, S. Nemsak, B. Ozdol, J. S. Kang, H. A. Bechtel, S. B. Desai, F. Kronast, A. A. Unal, G. Conti, C. Conlon, G. K. Palsson, M. C. Martin, A. M. Minor, C. S. Fadley, E. Yablonovitch, R. Maboudian, and A. Javey, “Strong interlayer coupling in van der Waals heterostructures built from single-layer chalcogenides,” *Proceedings of the National Academy of Sciences of the United States of America*, vol. 111, no. 17, pp. 6198–6202, 2014.

[214] A. Capretti, A. Lesage, and T. Gregorkiewicz, “Integrating quantum dots and dielectric mie resonators: A hierarchical metamaterial inheriting the best of both,” *ACS Photonics*, vol. 4, no. 9, pp. 2187–2196, 2017.

[215] A. Vaskin, S. Liu, S. Addamane, P. P. Vabishchevich, Y. Yang, G. Balarishnan, M. B. Sinclair, T. Pertsch, I. Brener, and I. Staude, “Manipulation of quantum dot emission with semiconductor metasurfaces exhibiting magnetic quadrupole resonances,” *Optics Express*, vol. 29, p. 5567, feb 2021.

[216] M. A. Steiner, J. F. Geisz, I. García, D. J. Friedman, A. Duda, and S. R. Kurtz, “Optical enhancement of the open-circuit voltage in high quality GaAs solar cells,” *Journal of Applied Physics*, vol. 113, no. 12, 2013.

[217] M. A. Green, “Radiative efficiency of state-of-the-art photovoltaic cells,” *Progress in Photovoltaics: Research and Applications*, vol. 20, no. 4, pp. 472–476, 2012.

[218] S. Sandhu, Z. Yu, and S. Fan, “Detailed balance analysis of nanophotonic solar cells,” *Optics Express*, vol. 21, no. 1, p. 1209, 2013.

[219] L. H. Slooff, R. Kinderman, A. R. Burgers, A. Büchtemann, R. Danz, T. B. Meyer, A. J. Chatten, D. Farell, K. W. J. Barnham, and J. A. M. van Roosmalen, “The luminescent concentrator illuminated,” in *Photonics for Solar Energy Systems*, vol. 6197, p. 61970K, 2006.

[220] U. Rau, F. Einsele, and G. C. Glaeser, “Efficiency limits of photovoltaic fluorescent collectors,” *Applied Physics Letters*, vol. 87, no. 17, pp. 1–3, 2005.

[221] G. C. Glaeser and U. Rau, “Collection and conversion properties of photovoltaic fluorescent collectors with photonic band stop filters,” in *Photonics for Solar Energy Systems*, vol. 6197, p. 61970L, 2006.

[222] N. D. Bronstein, Y. Yao, L. Xu, E. O’Brien, A. S. Powers, V. E. Ferry, A. P. Alivisatos, and R. G. Nuzzo, “Quantum Dot Luminescent Concentrator Cavity Exhibiting 30-fold Concentration,” *ACS Photonics*, vol. 2, no. 11, pp. 1576–1583, 2015.

[223] D. Şahin, B. Ilan, and D. F. Kelley, “Monte-Carlo simulations of light propagation in luminescent solar concentrators based on semiconductor nanoparticles,” *Journal of Applied Physics*, vol. 110, p. 033108, aug 2011.

[224] S. Sadeghi, R. Melikov, H. Bahmani Jalali, O. Karatum, S. B. Srivastava, D. Conkar, E. N. Firat-Karalar, and S. Nizamoglu, “Ecofriendly and Efficient Luminescent Solar Concentrators Based on Fluorescent Proteins,” *ACS applied materials & interfaces*, vol. 11, pp. 8710–8716, mar 2019.

[225] I. Papakonstantinou, M. Portnoi, and M. G. Debije, “The Hidden Potential of Luminescent Solar Concentrators,” *Advanced Energy Materials*, vol. 11, no. 3, pp. 2002883 (1–13), 2021.

[226] R. Mazzaro and A. Vomiero, “The Renaissance of Luminescent Solar Concentrators: The Role of Inorganic Nanomaterials,” *Advanced Energy Materials*, vol. 8, pp. 1801903 (1–19), nov 2018.

ABOUT THE AUTHOR

Julia Sofieke van der Burgt was born in Wageningen, the Netherlands on January 29, 1993, where she grew up and obtained her high school diploma in the direction Nature & Technology. In 2010 she moved to Delft, to start her bachelor's in Aerospace Engineering at the Technical University of Delft. During a minor in Nanomaterials at Georgia Institute of Technology in Atlanta, US, she got inspired by the fascinating phenomena occurring at the nanoscale. She spent a year taking additional physics courses to transition to a master's in this field, in combination with a follow-up project of her bachelor's thesis. Together with four fellow students, she built a prototype of the 'Birdplane', a bird-inspired drone. After this year, she started the master 'Nanomaterials: Physics and Chemistry at Utrecht University in 2015. During her master's, she worked a year at the Debye Institute for Nanomaterials Science under the supervision of Prof. Dr. Daniel Vanmeakelbergh and dr. Ingmar Swart on perovskite nanocrystals and did a six months internship at Philips working on optical shape sensing. She received her MSc degree cum laude (with honors) in 2017. At the end of that year, Julia joined the group of Prof. Dr. Erik Garnett at AMOLF as a Ph.D. student. Here, she worked on directional light emission for improving photovoltaic efficiency. The results of these scientific investigations are presented in this thesis. In early 2021 Julia went on a four-month maternity leave after giving birth to a daughter. In her free time, Julia enjoys outdoor activities and playing music on her double bass or piano.